

Jorge Jovicich: An Investigation of the Use of Gradient- and Spin-Echo (GRASE) Imaging for Functional MRI of the Human Brain. Leipzig: Max Planck Institute of Cognitive Neuroscience, 1999 (MPI Series in Cognitive Neuroscience; 4)

An investigation of the use of Gradient- and Spin-Echo (GRASE) imaging for functional MRI of the human brain

Von der Fakultät für Physik und Geowissenschaften

der Universität Leipzig

genehmigte

DISSERTATION

zur Erlangung des akademischen Grades

doktor rerum naturalium

Dr. rer. nat.

vorgelegt

von **M.Sc. Jorge Jovicich**

geboren am 13. März 1968 in Córdoba, Argentinien

Gutachter: PD David G. Norris
Prof. Jürgen Hennig
Dr. Glyn Johnson

Tag der Verleihung: 22. Februar 1999

Bibliographische Beschreibung:

Jorge Jovicich

**An investigation of the use of Gradient- and Spin-Echo (GRASE)
imaging for functional MRI of the human brain**

Universität Leipzig, Diss., in englischer Sprache,
S. 91, Lit. 110, Abb. 32, Tab. 1

Referat:

The most widely used imaging technique for performing functional magnetic resonance imaging (fMRI) of the human brain is gradient-echo imaging using blood oxygenation level dependent (BOLD) contrast. Due to its high speed, high signal-to-noise ratio and high intrinsic BOLD contrast, Echo Planar Imaging (EPI) has become the most commonly used gradient-echo imaging technique for fMRI. EPI has, however, limitations when imaging brain areas with strong magnetic field inhomogeneities, i.e., areas with short T_2^* . In such areas, which are often important for cognitive studies, EPI gives strong image distortions, signal loss and poor spatial resolution. These problems become more severe at high magnetic field strengths, which are preferred for fMRI because they offer a higher BOLD contrast.

This work examines the use of Gradient- and Spin-Echo (GRASE) as an alternative imaging method to EPI for fMRI in brain regions with short T_2^* using a 3 Tesla system. The choice of GRASE is motivated by its lower sensitivity to field inhomogeneities compared to EPI and its lower radio-frequency power deposition in comparison with a pure spin-echo imaging method.

The work starts by investigating the quality of GRASE images obtained with short effective echo time phase-encoding schemes. A new template interactive phase-encoding (TIPE) scheme is proposed and demonstrated. In areas where a good phase correction can be achieved, TIPE offers better SNR and less image artifacts than previously proposed schemes.

The BOLD contrast capabilities of GRASE are examined. Two strategies are considered: use of the intrinsic BOLD contrast and incorporation of an additional BOLD contrast with a T_2^* preparation experiment. After a computer simulation study the first option is discarded as it leads to similar limitations as those of EPI. The second option is further investigated and a method for achieving T_2^* -weighted GRASE is demonstrated using the displaced-echo technique. This method results in a signal loss of approximately 50 % compared to EPI but better image quality in brain regions with short T_2^* .

The use of T_2^* -weighted GRASE for fMRI is demonstrated in the visual cortex. A computer simulation is used to estimate the functional sensitivity of displaced GRASE as compared to EPI. The simulation and experimental results indicate that displaced GRASE may offer better functional sensitivity than EPI for brain areas having cortical tissues with T_2^* up to approximately 15ms for the experimental conditions investigated.

Contents

Abstract	i
Symbols and Abbreviations	v
1 Introduction	1
1.1 Magnetic resonance	1
1.1.1 NMR in medicine	1
1.1.2 The magnetic resonance phenomenon	2
1.1.3 Classical description	3
1.1.4 Relaxation	6
1.1.5 Frequency offsets	8
1.1.6 Single and multipulse NMR experiments: coherence pathways	9
1.1.7 Magnetic field gradients	14
1.2 Basic principles of MRI	18
1.2.1 k -space	18
1.2.2 Selective excitation	19
1.2.3 Frequency and phase encoding	21
1.2.4 Artifacts: the PSF formalism	24
1.3 Fast imaging sequences	25
1.3.1 Echo Planar Imaging (EPI)	26
1.3.2 Rapid Acquisition with Relaxation Enhancement (RARE)	28
1.3.3 Gradient and Spin Echo Imaging (GRASE)	30
1.4 Functional MRI of the human brain	32
1.5 Aims of this work	34
2 GRASE imaging	35
2.1 Importance of the phase-encoding method	35
2.2 Reduction of phase errors	36
2.3 Review of short TE_{eff} phase encoding methods	37
2.3.1 Centric GRASE	37
2.3.2 k -space banded centric GRASE	38
2.3.3 Conventional centric scheme for GRASE	39
2.4 A novel Template Interactive Phase Encoding method	39
2.5 Evaluation of phase-encoding methods: comparison of PSFs	41

3	Implementation of GRASE imaging at 3 Tesla	45
3.1	Imaging sequence	45
3.2	Image reconstruction algorithm	47
3.3	Imaging experiments	50
3.3.1	Phantom images	50
3.3.2	In-vivo images	50
4	Application of GRASE for BOLD fMRI	56
4.1	Intrinsic sensitivity of GRASE for BOLD fMRI	56
4.2	Additional T_2^* contrast for GRASE	60
4.2.1	T_2^* preparation experiment	60
4.2.2	T_2^* -weighted GRASE: displaced-echo method	60
4.3	Use of displaced GRASE based BOLD in the visual cortex	63
4.4	Displaced GRASE in brain regions with short T_2^*	68
4.5	Functional sensitivity of displaced GRASE	71
5	Summary and conclusions	74
A	Materials	78
A.1	MRI system	78
A.2	MRI samples	78
A.2.1	Phantom	78
A.2.2	Volunteers	78
	Bibliography	81
	Acknowledgements	89
	Curriculum Vitae	91
	Publications	93

Symbols and Abbreviations

Symbols

$A(k)$	amplitude modulation in a one-dimensional k -space
bw_p	R.F. pulse bandwidth
$bw_s = 1/\delta t$	sampling bandwidth
\mathbf{B}	magnetic flux density vector
\mathbf{B}_0	magnetic flux density vector of the static field
\mathbf{B}_1	magnetic flux density vector of the radio-frequency (R.F.) field
$B_1(t)$	amplitude modulation of the R.F. field
\mathbf{B}'_1	field \mathbf{B}_1 expressed in the rotating frame
\mathbf{B}_{eff}	effective magnetic field vector in the rotating frame
ΔB_0	half-bandwidth of a Lorentzian field inhomogeneities distribution
d_1, d_2	delays
ΔE	energy transition in a spin system with $I = 1/2$
$(FOV)_x, (FOV)_y$	field of view along x and y -axes
\mathbf{G}	magnetic field gradient vector with components $G_x = G_{\text{read}}, G_y = G_{\text{phase}}$ and $G_z = G_{\text{slice}}$
ΔG_r	displacing gradient in the read direction
$\hbar = h/(2\pi)$	Planck constant
H	Hamilton operator
$i^2 = -1$	complex unit
$\mathbf{i}, \mathbf{j}, \mathbf{k}$	orthogonal unitary vectors in the laboratory frame corresponding to the x, y , and z -axes respectively
$\mathbf{i}', \mathbf{j}', \mathbf{k}' = \mathbf{k}$	orthogonal unitary vectors in the rotating frame
i_g	integer index for the gradient echoes: $i_g = 1, \dots, N_g$
i_p	integer index for the RF pulses: $i_p = 1, \dots, N_p$
\mathbf{I}	nuclear spin angular momentum operator
I	nuclear spin angular momentum
I_x, I_y, I_z	Cartesian components of angular momentum spin operators
k	Boltzmann constant
\mathbf{k}	k -space coordinate vector with components $k_x = k_{\text{read}}, k_y = k_{\text{phase}}, k_z = k_{\text{slice}}$
$\delta k_x, \delta k_y$	intersample separation in k -space
m_z	eigenvalues of I_z operator
\mathbf{M}	magnetization vector with components M_x, M_y and M_z
$\mathbf{M}_0 = M_0 \mathbf{k}$	equilibrium magnetization vector
\mathbf{M}_{xy}	transverse component of the magnetization vector in the laboratory frame
$\mathbf{M}_{\mathbf{x}'\mathbf{y}'}$	transverse component in the rotating frame
N_+, N_-	spin population numbers of a spin system with $I = 1/2$
$N_x = N_{\text{read}}, N_y = N_{\text{phase}}$	number of sampling points along the x and y -axes, which are also the read and the phase-encoding directions

N_g	number of gradient echoes per RF interval in a GRASE sequence
N_p	number of RF refocusing pulses in RARE or GRASE sequences
$P(k)$	phase modulation in a one-dimensional k -space
\mathbf{r}	position vector
R_2	irreversible relaxation rate of transverse magnetization
R_2'	reversible relaxation rate of transverse magnetization
R_2^*	total relaxation rate of transverse magnetization
$s(t)$	time domain NMR signal
$S(\omega)$	frequency domain signal (Fourier transform of $s(t)$)
$S_{\text{GRASE}}, S_{\text{GE}}, S_{\text{SE}}$	image intensity given by GRASE, GE, and SE sequences respectively
S_a, S_c	signals during stimulation (activation) and control conditions respectively
ΔS	functional signal change
t_{acq}	acquisition window
δt	sampling interval in the time domain
T	absolute temperature, eq. (1.6)
T	sampling duration interval, section 1.2.4
T_1	longitudinal relaxation time
T_2	transverse relaxation time
T_2^*	effective transverse relaxation time
TE	echo time
TE_{eff}	effective echo time
TR	repetition time
$\delta x, \delta y$	pixel dimensions
Δz	slice thickness
α	rotation angle of R.F. pulse (flip angle)
$\alpha_{x'}$	R.F. pulse with \mathbf{B}_1' field along x' axis in the rotating frame
ϕ	magnetization phase in the rotating frame
γ	gyromagnetic ratio
μ	nuclear magnetic moment
$\Delta\nu = 1/(\pi T_2^*)$	Lorentzian linewidth broadening
$\boldsymbol{\omega} = -\gamma\mathbf{B}$	resonance frequency vector
$\omega_0 = \gamma B_0$	Larmor frequency
$\omega_1 = \gamma B_1$	resonance frequency of the B_1 field
$\Delta\omega$	frequency offset
Ω	rotation frequency of the rotating frame
$\rho(\mathbf{r})$	spin density spatial distribution
σ	chemical shield factor
τ	duration of a R.F. pulse, eq. (1.15)
τ	R.F. pulse separation intervals, section 1.1.6
τ	T_2^* weighting delay
θ	phase of a R.F. pulse

Abbreviations

AM	amplitude modulation in k -space
BOLD	blood oxygenation level dependent
CPMG	Carr-Purcell Meiboom-Gill
EPI	echo planar imaging
eq.	equation
fMRI	functional magnetic resonance imaging
Fig.	figure
FID	free induction decay
FOV	field of view
GRASE	gradient- and spin-echo
GRE	gradient-echo
GE-EPI	gradient-echo EPI
kb	k -space banded
ppm	parts per million
PM	phase modulation in k -space
PSF	point spread function
RARE	rapid acquisition with relaxation enhancement
RF	radio-frequency
TIPE	template interactive phase encoding
SE	spin-echo
SE-EPI	spin-echo EPI
STE	stimulated-echo
SNR	signal-to-noise ratio

Chapter 1

Introduction

This work is concerned with the investigation of the GRASE (GRAdient And Spin-Echoes) method for functional imaging of the human brain using the blood level dependent oxygenation (BOLD) contrast and a high main field MRI system.

This first chapter introduces the physics of magnetic resonance imaging (MRI) and describes how this method can be used to obtain fast images where the contrast is a function of proton spin density and relaxation times. The introduction is written with an emphasis on the aspects that will be of relevance in the following chapters. The basic principles of the GRASE imaging method are introduced and the last part of the chapter describes the aims of this work.

The second chapter discusses in more detail the origin of artifacts in GRASE images due to the modulation of both the phase and the amplitude of the signal along the echo train. The importance of the phase-encoding method for reducing these artifacts is examined using the point spread function (PSF) formalism. This chapter considers previously proposed phase-encoding schemes and presents a novel phase-encoding method.

The third chapter describes the implementation of GRASE on a 3 Tesla MRI system and discusses the image quality obtained with the different phase encoding methods examined in chapter 2. The experimental results are compared with the predictions made by the PSF analysis.

The fourth chapter investigates methods for obtaining BOLD contrast in a GRASE sequence. The intrinsic BOLD contrast of GRASE is considered. A method for increasing the intrinsic BOLD contrast is investigated by using a T_2^* preparation experiment. The use of GRASE based BOLD is demonstrated in the visual cortex using the phase-encoding method which was found to give the lowest artifacts and highest signal-to-noise-ratio in the studies of chapter 3.

Finally, the last chapter gives a summary of the results.

1.1 Magnetic resonance

1.1.1 NMR in medicine

Nuclear magnetic resonance (NMR) is a phenomenon based on the absorption of radio-frequency (RF) energy by the magnetic moments of atomic nuclei within samples placed in a strong

magnetic field. NMR has been used to study organic and inorganic probes and has also found applications in medicine.

The measurement of nuclear magnetic resonance on bulk materials was made possible by Felix Bloch *et al* [1] and Edward Purcell *et al* [2] in 1946. This was soon followed by the discovery of chemical shift, allowing nuclei in different chemical environments to be identified as a result of the small change in resonance frequency caused by the electron cloud of the molecule [3]. The NMR method was further developed with the spin-echo experiment proposed by Hahn [4], Carr and Purcell [5] and by Meiboom and Gill [6]. A major step in the development of NMR was the incorporation of the Fourier transform of the NMR signal, first proposed by Ernst and Anderson in 1966 [7].

Although high-resolution NMR has developed as a versatile tool for studying the chemistry and structure of solids and liquids, the major bio-medical interest has arisen from the possibilities of making measurements in living tissue. In parallel with the development of spectroscopic techniques, methods for imaging the distribution of protons in tissue evolved. In 1973 the principle of utilising the shift in resonance frequency resulting from the imposition of a magnetic field gradient was proposed by Lauterbur [8] and later by Mansfield and Grannel [9]. It was realised that this method could be used for obtaining the two-dimensional spatial distribution of protons in a sample: nuclear magnetic resonance imaging (MRI) was born. Since these early days a vast number of technical and commercial developments have been made and MRI has become a routine imaging method used in medicine and biology for a wide variety of applications.

In recent years, an increasing number of MRI strategies have been described which allow the possibility of acquiring clinically useful images in a time scale of a few hundred milliseconds or even less. The evolution of these methods has been possible due to both an increasing understanding of the complexities inherent to pulse sequence design and the increasing availability of stronger and rapidly switchable magnetic field gradients. These two factors have permitted drastic reductions of MRI data acquisition times, hence enormously increasing the scope of applications by MRI.

1.1.2 The magnetic resonance phenomenon

Magnetic resonance (MR) is a phenomenon found in systems that possess a non-zero spin quantum number. Such systems could consist, for example, of electron spins or of atomic nuclei. We are here concerned with nuclear MR. A system such as a nucleus may be composed of many particles coupled together so that in any given state, the nucleus possesses a total magnetic moment $\boldsymbol{\mu}$ and a spin angular momentum \mathbf{I} so that

$$\boldsymbol{\mu} = \gamma \mathbf{I} \quad (1.1)$$

where γ is a scalar known as the gyromagnetic ratio and is a property of the nucleus. The application of a static external magnetic field with flux density \mathbf{B}_0 will produce an interaction energy given by the Hamiltonian

$$H = -\boldsymbol{\mu} \cdot \mathbf{B}_0 \quad (1.2)$$

Replacing eq. (1.1) in eq. (1.2) and taking the field to be of magnitude B_0 along the z -direction gives

$$H = -\gamma \hbar B_0 I_z \quad (1.3)$$

with eigenvalues

$$E_{m_z} = -\gamma \hbar B_0 m_z \quad (1.4)$$

where m_z are the eigenvalues of I_z ($m_z = -I, -I + 1, \dots, I - 1, I$) and \hbar is Planck's constant divided by 2π . Equation (1.4) describes the energy splitting which results from the quantisation in the z -component of the magnetic moment.

For systems having $I = \frac{1}{2}$ (such as protons, which are of main interest in this work) there will be two different energy levels: $m_z = +\frac{1}{2}$, the low energy state and $m_z = -\frac{1}{2}$, the high energy state. A transition between these two states can be produced by applying a magnetic field \mathbf{B}_1 of angular frequency ω_0 in the transverse plane such that

$$\hbar\omega_0 = \Delta E = \gamma \hbar B_0 \quad (1.5)$$

where ΔE is the energy difference between the two states. The frequency of the \mathbf{B}_1 -field is called the Larmor frequency (ω_0), and its magnitude is given by $\omega_0 = \gamma B_0$.

Until now the states of a single spin in a magnetic field have been described. Consider now a macroscopic sample of uncoupled spins ($I = \frac{1}{2}$). Since there are many nuclei, we shall specify the number in the two m_z states $+\frac{1}{2}$ and $-\frac{1}{2}$ by N_+ and N_- , respectively. In thermal equilibrium the statistical distribution of the spin states will be given by the Boltzmann distribution,

$$\frac{N_-}{N_+} = \exp\left(-\frac{\Delta E}{kT}\right) \quad (1.6)$$

where k is the Boltzmann constant and T is the absolute temperature of the spin system (which is equal to the lattice temperature when the sample is in thermal equilibrium). Thus, at thermal equilibrium there is a population difference between the two energy states and this gives rise to a macroscopic bulk magnetization \mathbf{M}_0 oriented along the direction of the external static field \mathbf{B}_0 . An interaction with the magnetic field \mathbf{B}_1 will induce transitions between the eigenstates and the bulk magnetization \mathbf{M} will no longer be in equilibrium. By using the Heisenberg representation for the equation of motion of the angular momentum I and the commutation relationships of I , it can be shown [10] that the observable behaviour of a sample containing a large number of noninteracting identical spins can be described classically.

1.1.3 Classical description

Many aspects of NMR can be understood by considering systems of isolated spins hence allowing a description on classical grounds. An adequate treatment of systems with coupled spins should be made using a quantum mechanical description [11].

The classical formalism will be used to describe the dynamics of the bulk magnetization and how this can be manipulated by the use of radiofrequency (RF) pulses.

Derivation of the classical equation of motion

A magnet with magnetic moment $\boldsymbol{\mu}$ in an arbitrary magnetic field with flux density \mathbf{B} will experience a torque of amount $\boldsymbol{\mu} \times \mathbf{B}$. An ordinary magnet, mounted with bearings so that it could turn at will, would attempt to line up along the direction of \mathbf{B} . If the magnet also possesses (spin) angular momentum \mathbf{I} then the equation of motion of the magnet can be obtained by equating the torque with the rate of change of angular momentum (from second Newton's law)

$$\frac{d\langle \mathbf{I} \rangle}{dt} = \boldsymbol{\mu} \times \mathbf{B} \quad (1.7)$$

Using eq. (1.1) and considering a system consisting of several magnets $\boldsymbol{\mu}_i$ then the total magnetization will be given by $\mathbf{M} = \sum \boldsymbol{\mu}_i$ and its equation of motion by

$$\frac{d\mathbf{M}}{dt} = \mathbf{M} \times \gamma \mathbf{B} \quad (1.8)$$

This equation states that, as with the expectation values given by the quantum mechanical description, at any instant of time the magnetization \mathbf{M} is precessing about the field \mathbf{B} at the frequency

$$\boldsymbol{\omega} = -\gamma \mathbf{B} \quad (1.9)$$

This equation is known as the Larmor equation. The minus sign indicates that the vectors $\boldsymbol{\omega}$ and \mathbf{B} are antiparallel. In what follows, the minus sign will be neglected when considering the magnitude of the frequency. The spins which precess at the Larmor frequency $\omega_0 = \gamma B_0$ are said to be on resonance.

The rotating coordinate system

Equation (1.8) can be solved by standard methods of differential equations for various assumed time varying fields \mathbf{B} . However, the description of the dynamics of \mathbf{M} can be significantly simplified by introducing the use of a rotating coordinate system.

It can be proved [10] that in a frame of reference rotating about the direction of the external static field \mathbf{B}_0 with frequency Ω , the equation of motion of \mathbf{M} is identical to equation (1.8) except that the field \mathbf{B} has to be replaced by an effective field \mathbf{B}_{eff} ,

$$\frac{d\mathbf{M}}{dt} = \mathbf{M} \times \gamma \mathbf{B}_{\text{eff}} \quad \text{with} \quad \mathbf{B}_{\text{eff}} = \mathbf{B} + \frac{\Omega}{\gamma} \quad (1.10)$$

Assuming that in the laboratory frame the total field \mathbf{B} is composed of a constant field term \mathbf{B}_0 and an arbitrary time varying field \mathbf{B}_1 , the effective field will be

$$\mathbf{B}_{\text{eff}} = \mathbf{B}_0 + \mathbf{B}'_1 + \frac{\Omega}{\gamma} \quad (1.11)$$

where \mathbf{B}'_1 is the field \mathbf{B}_1 expressed in the rotating frame.

By choosing Ω such that $\Omega = -\gamma B_0$, the equation of motion of the magnetization takes a particularly easy form in the rotating frame

$$\frac{d\mathbf{M}}{dt} = \mathbf{M} \times \gamma \mathbf{B}'_1 \quad (1.12)$$

which expresses that in the rotating frame the magnetization of the spins on resonance will precess about the field \mathbf{B}'_1 .

Manipulating the magnetization with RF pulses

Equation (1.12) tells us that if only the external static field is present (i.e., $\mathbf{B}'_1 = 0$), then in the rotating frame the magnetization \mathbf{M} remains static and aligned with \mathbf{B}_0 as this was the initial condition.

In order to measure \mathbf{M} , it must be tilted away from the \mathbf{B}_0 or z -direction, to produce a measurable component \mathbf{M}_{xy} in the xy plane. Any component of the magnetization that is in the transverse plane precesses about \mathbf{B}_0 with frequency ω_0 , and can induce a measurable voltage at this frequency in an appropriately placed receiver coil. This is the basis of the MR experiment.

The most effective way of rotating magnetization into the transverse plane is by using a magnetic field \mathbf{B}_1 perpendicular to \mathbf{B}_0 and rotating about the z -axis at the resonance frequency $\omega_0 = -\gamma\mathbf{B}_0$ [11]. Such a field may be expressed mathematically as

$$\mathbf{B}_1(t) = B_1(t) \cos(\omega_0 t + \theta) \mathbf{i} + B_1(t) \sin(\omega_0 t + \theta) \mathbf{j} \quad (1.13)$$

where $B_1(t)$ is the amplitude and θ is the initial phase of the applied field with respect to the (arbitrarily chosen) x - or y -axes, whose directions are defined by the unitary vectors \mathbf{i} and \mathbf{j} respectively.

In the rotating frame the effective magnetic field for on resonance spins is

$$\mathbf{B}_{\text{eff}}(t) = \mathbf{B}'_1(t) = B_1(t) \cos(\theta) \mathbf{i}' + B_1(t) \sin(\theta) \mathbf{j}' \quad (1.14)$$

Therefore, in the rotating frame the effective field has a constant direction (defined by θ) on the xy plane and the magnetization vector precesses under the influence of this effective field at a frequency $\omega_1 = \gamma B_1(t)$. The effect of $\mathbf{B}_{\text{eff}}(t)$ is then to rotate the magnetization about the direction defined by the phase θ giving a component $\mathbf{M}_{x'y'}$ in the $x'y'$ plane of the rotating frame.

A RF field of duration τ , known as a RF pulse, will rotate the magnetization vector of on resonance spins through an angle

$$\alpha = \gamma \int_0^\tau B_1(t) dt \quad (1.15)$$

This angle is known as the flip angle of the RF pulse. Pulses producing flip angles $\alpha = 90^\circ$ and $\alpha = 180^\circ$ play important roles in MRI.

A note on RF power deposition: Power deposition from RF radiation is well known to produce local heating if sufficient power is absorbed in tissue with a risk of metabolic rate increase if the deposited heat is not dissipated rapidly enough. It has been demonstrated that the absorbed power is proportional to $\omega_0^2 \cdot B_1^2$ [12], which means that MRI experiments on a high field system deposit considerably more power, particularly when using RF pulses with large flip angles. RF exposure limits have been drawn up on the basis that any significant rise in temperature of the sensitive tissues of the body should be avoided. Acceptable exposures should not result in a rise of body temperature of more than 1°C or more than 1°C in any mass of tissue under 1 g in the body. In a human head this may be ensured by limiting the mean specific absorption rate to 4 W kg^{-1} [13].

Magnetization response of an RF pulse

For any given system, the spins precess over a range of frequencies because the main magnetic field \mathbf{B}_0 in real conditions is never perfectly homogeneous. RF pulses, on the other hand, can be applied during a finite duration τ and will therefore have an effect on spins precessing over a bandwidth of frequencies. Consequently, the response of the magnetization to an RF pulse is a function of the local resonance frequency.

The magnetization response of an RF pulse is the distribution $\mathbf{M}(\omega)$ arising from its application to fully relaxed magnetization uniformly distributed over all precessional frequencies. The RF pulse can be then viewed as mapping the frequency distribution of the magnetization from its initial state into a new state. As will be discussed in a later section, the fact that RF pulses operate on frequency distributions is an important property used for spatial encoding in MR imaging.

The bandwidth of a RF pulse defines the degree to which the pulse is frequency selective. The bandwidth depends on both the pulse modulation $B_1(t)$ (also referred to as the shape of the pulse) and the pulse duration. In general the longer the duration of an RF pulse the narrower the bandwidth. Pulse shapes can be designed to obtain a desired frequency characteristic thereby optimizing the magnetization response for a particular experiment.

RF probe: signal transmission and acquisition

The $B_1(t)$ or radiofrequency field is generated using the so-called probe or coil driven by an RF amplifier source. For many applications coils are designed to generate a circularly polarized magnetic field (quadrature coils). Compared to linear polarization, circular polarization has the advantage of a reduction in excitation power (up to 50 % reduction) and improved signal-to-noise ratio, or SNR (by a factor of $\sqrt{2}$) [14].

The RF coil is often used both to generate the B_1 field (transmission) and to acquire the NMR signal (reception) by inductively coupling to the sample magnetization. The detector system effectively transforms the input signal from the lab frame to the rotating frame of reference by independently mixing it with two orthogonal RF sources of the pure Larmor frequency with a 90° phase difference. This method for signal acquisition is called quadrature detection. The two demodulated channels are the in-phase and quadrature components of the signal. The channels are frequently regarded as the real and imaginary components of the complex signal. This is equivalent to considering the measured signal as being effectively generated by the transverse magnetization $M_{x',y'}$ in the rotating frame.

1.1.4 Relaxation

The equation of motion (1.8) describes the macroscopic behaviour of a spin system with a magnetization vector \mathbf{M} of constant magnitude. In reality, however, a spin system shows relaxation effects and for a correct description of the system the terms modelling these effects have to be incorporated. Relaxation is of great importance in the design of pulse sequences because of its consequences on the image SNR, spatial resolution and contrast. The following is a brief description of the mechanisms of NMR relaxation. A full description can be found in the literature [10, 11, 15].

Spin-lattice relaxation (T_1)

Consider, for example, a sample of spins with $I = \frac{1}{2}$ initially free from the influence of external magnetic fields and at equilibrium. Equation (1.4) states that there is no splitting of the spin population into distinct energy levels. If this sample is now rapidly brought into a strong magnetic field \mathbf{B}_0 , the spins will be equally distributed between the two energy levels: $N_+ = N_-$. Thus, the populations will not be in the equilibrium state given by equation (1.6). We know, however, that after some time equilibrium is established giving a net magnetization. This equilibrium state corresponds to the low energy state having a larger spin population than the high energy level. Therefore, in order to reach equilibrium, there has to be a mechanism by which transitions between the spin states occur. In this process, there is a net number of transitions from the upper to the lower energy state. The spins give up a certain amount of energy, hence there must be a coupling with some other system (called the lattice) in an energy state that permits these transitions.

The process by which thermal equilibrium is established is called spin-lattice relaxation, longitudinal relaxation or T_1 relaxation. This process is described by the equation

$$\frac{d}{dt}M_z = -\frac{(M_z - M_0)}{T_1} \quad (1.16)$$

and it can be seen that the longitudinal magnetization M_z of the spin system approaches equilibrium with a time constant T_1 .

T_1 relaxation is a process in which energy is transferred between the spin system and the lattice. The interaction is mediated by fluctuating magnetic fields (e.g., the dipole moments of molecules like water) and the nuclear dipole moment. These fluctuating fields will have components in the xy plane, some of which will vibrate at the resonance frequency $\omega_0 = -\gamma\mathbf{B}_0$ therefore stimulating emission or absorption of energy. This means that the T_1 relaxation process depends on the external field strength. The T_1 relaxation time provides information about vibrational motion in the lattice. Tissue can be considered as a fluid for which the lattice is generally water, therefore T_1 relaxation is a measure of the ability that water molecules have to tumble and rotate in the neighbourhood of the spins whose signal is being measured.

Spin-spin relaxation (T_2)

Transverse, T_2 or spin-spin relaxation is the loss of coherent magnetization \mathbf{M}_{xy} from the xy plane. As this is the magnetization that is measured, T_2 relaxation gives the observed decay in the NMR signal. This relaxation process results both from a loss of phase coherence in the xy plane and also as a result of the longitudinal relaxation causing a net loss in signal from the xy plane. In tissue, T_2 relaxation is usually considerably faster than T_1 relaxation. In the liquid state, the process of spin-spin relaxation can be approximately modelled by a first order process with time constant T_2

$$\frac{d}{dt}\mathbf{M}_{xy} = -\frac{\mathbf{M}_{xy}}{T_2} \quad (1.17)$$

The molecular magnetic fields referred to above also usually give rise to a z component in addition to the xy component, which has the effect of slightly altering the effective field B_0 experienced by the nucleus. This causes the frequency of precession to vary slightly, causing an irreversible loss of phase coherence and therefore a reduction in the net magnetization \mathbf{M}_{xy} .

Another effect that gives rise to loss of phase is an exchange of the spin state between two nuclei, with no net loss of energy from the spin system, but a loss of phase information.

The Bloch equations

The terms modelling T_1 and T_2 relaxation processes can be introduced into the equations describing the evolution of the magnetization (1.8). The resulting formulae model the magnetization behaviour, and are the phenomenological Bloch equations [1]

$$\frac{d}{dt}\mathbf{M} = \gamma\mathbf{M} \times \mathbf{B} - \frac{(M_z - M_0)}{T_1}\mathbf{k} - \frac{1}{T_2}(M_x\mathbf{i} + M_y\mathbf{j}) \quad (1.18)$$

in the laboratory frame. The unitary vector \mathbf{k} is in the direction of the z -axis for both the laboratory frame and the rotating frame. The Bloch equations in the rotating frame can be obtained by replacing the field \mathbf{B} by the effective field \mathbf{B}_{eff} . The Bloch equations assume that the spins are static but they can be generalized to include the effects of diffusion and flow [16].

Relaxation through inhomogeneous dephasing (T_2^*)

In practice, factors other than T_2 relaxation also cause loss of transverse magnetization. The components of the magnetization M_{xy} rotate with a precession frequency defined by the local magnetic field $\omega(\mathbf{r}) = -\gamma\mathbf{B}(\mathbf{r})$. If the magnetic field varies spatially then there will be an additional dephasing of the spins due to the spread in frequencies for a given nucleus. The effective T_2 relaxation time will then be shorter, and is generally modelled by an exponential decay defined by the time constant T_2^*

$$1/T_2^* = 1/T_2 + \gamma\Delta B_0/2 \quad (1.19)$$

where the term $\gamma\Delta B_0/2$ represents signal loss due to magnetic field inhomogeneities. Therefore, to take into account these effects T_2 should be replaced by T_2^* in the Bloch equations.

1.1.5 Frequency offsets

The spins in a sample will have the same resonance frequency and therefore precess in phase only in the ideal case that they all experience the same magnetic field. In a real case there are magnetic field inhomogeneities ΔB_0 present, thus generally there will be a distribution of resonance frequencies centred at a frequency which is offset by $\Delta\omega$ from the Larmor frequency ω_0 . Thus, in the rotating frame only the on resonance ($\omega = \omega_0$) spins will remain static whereas the off resonance spins will precess with a frequency given by $\Delta\omega = \gamma\Delta B_0$. Frequency offsets will cause spins to lose phase coherence. The phase difference between on resonance spins and off resonance spins is frequently termed the phase-error.

Frequency offsets may arise for several reasons. One principal cause can be inhomogeneities of the main static field B_0 . Such effects are reduced by optimizing the field uniformity in the region of interest with the use of additional external fields generated from the so-called shim coils. Another source of field inhomogeneities is the presence of objects with different intrinsic magnetic susceptibilities. When such objects are in a magnetic field, the difference in their magnetic polarization will lead to local field gradients near their boundaries. These effects cannot be entirely corrected by shimming and they become worse as the main field

strength B_0 gets stronger. In the human brain there are regions with strong field susceptibility induced inhomogeneities at the interfaces between air and brain tissue. These inhomogeneities are particularly severe in regions where the brain is in close proximity to air such as the frontal sinuses. In other regions of the skull these problems are less severe because through thicker bone there is a larger separation between brain tissue and air hence weaker susceptibility gradients.

Frequency offsets can also develop due to chemical shift. The main field experienced by a proton in an external field B_0 is $B = B_0(1 - \sigma)$, where σ is the magnetic shielding factor and depends on the electronic cloud surrounding the proton hence on the chemical environment of the proton. This results in water protons having a slightly different resonance frequency as protons in lipid molecules. The chemical shift is a measure of the relative frequency difference relative to the ω_0 . Chemical shift is measured in parts per million (ppm) and for fat is approximately 3.3 ppm ($\simeq 440$ Hz at 3 Tesla).

1.1.6 Single and multipulse NMR experiments: coherence pathways

In most MRI methods the magnetization is manipulated by using several RF pulses. In this section the effects that a series of RF pulses can have on the magnetization are discussed. The concepts of free induction decay, spin echoes, stimulated echoes and coherence pathways will be introduced. These concepts are of vital importance in the design of fast imaging MR methods.

Single RF pulse (free induction decay)

The simplest NMR experiment consists of using a single RF pulse. The resulting signal is called free induction decay or FID. Let us assume that the $B_1(t)$ field is applied along the y' axis of the rotating frame such that it rotates the equilibrium magnetization M_0 by an angle α about the z axis of the rotating frame. Such a pulse is denoted by $\alpha_{y'}$. Thus, immediately after the pulse the magnetization in the rotating frame is

$$\mathbf{M}(\mathbf{0}_+) = M_0 \sin \alpha \mathbf{i}' + M_0 \cos \alpha \mathbf{k} \quad (1.20)$$

At a time t after the RF pulse has been turned off, the tranverse magnetization will be given by the solution of the Bloch equations, which in the laboratory frame gives

$$M_{xy}(t) = M_x(t) + i M_y(t) = M_0 \sin \alpha \exp(i\omega_0 t - t/T_2^*) \quad (1.21)$$

The complex signal $s(t)$, obtained by simultaneous observation of both x and y -components by quadrature detection, is directly proportional to the complex magnetization $M_{xy}(t)$. In NMR it is usually the frequency spectrum $S(\omega)$ (i.e., the Fourier transform of $s(t)$) which is of most interest

$$S(\omega) = \int_0^\infty s(t) \exp(-i\omega t) dt \quad (1.22)$$

giving the complex spectrum

$$S(\Delta\omega) = M_0 \sin \alpha \frac{1/T_2^* - i\Delta\omega}{(1/T_2^*)^2 + (\Delta\omega)^2} \quad (1.23)$$

where the frequency offset $\Delta\omega = \omega - \omega_0$ is measured with respect to the centre of the resonance.

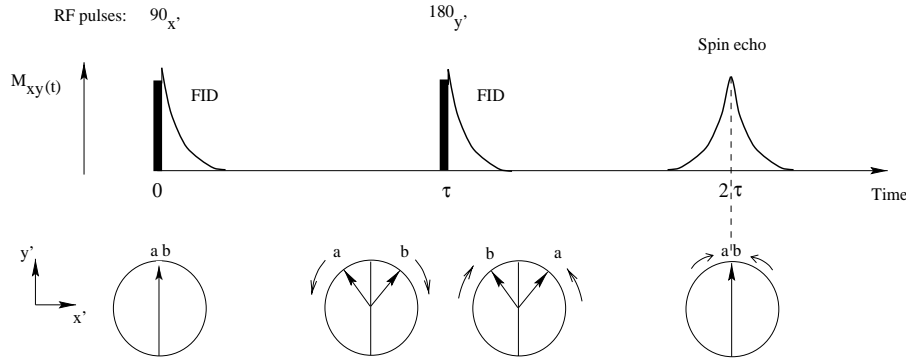


Figure 1.1: Formation of a spin echo. The dephasing of two spin isochromats with opposite off resonance frequencies is described. Static spins precess with constant frequency vector. The 180° refocusing pulse reverse their phases so that an echo is formed at 2τ .

It is clear that the maximum signal will be obtained when $\alpha = \pi/2$. The real or absorptive component of complex spectrum gives a Lorentzian lineshape, the imaginary or dispersive component is broader. The interpretation of the NMR signal is thus facilitated by applying a phase-correction after the Fourier transform and examining only the absorptive component. If there were no T_2 relaxation and no field inhomogeneities, then there would be only one resonance frequency and the absorption component would be a delta function centred at this frequency. This is in practice not the case and the full width at half maximum ($\Delta\nu$) of the Lorentzian lineshape gives a measure of the frequency bandwidth that absorbs energy $\Delta\nu = 1/(\pi T_2^*)$.

Two RF pulses (spin-echo)

An NMR experiment using two RF pulses can produce three signals: two FIDs, one immediately following each RF pulse, and a third signal called spin-echo or Hahn echo [4]. If the spacing between the RF pulses is τ then the spin-echo will appear at a time 2τ from the first RF pulse. The pulse sequence and the possible signals are shown in Figure 1.1.

The formation of the spin-echo can be easily understood by using the vector model for the macroscopic magnetization. To simplify the description using this model, it will be assumed that there is no T_2 relaxation but there is signal dephasing due to static field inhomogeneities (i.e., the field inhomogeneities do not change with time). It will be further assumed that the first RF pulse is along the x' axis of the rotating frame and that the second RF pulse is a perfect 180° pulse along the y' axis. With these definitions, the pulse sequence shown in Fig. 1.1 can be abbreviated by the notation: $\alpha_{x'} - \tau - 180_{y'}^\circ - \tau$. These assumptions are not necessary for the formation of a spin echo and they will be later removed for a more general description not involving the magnetization vector model.

The lower part of Fig. 1.1 schematically shows how the magnetization in the rotating frame evolves for two groups of spins (also called spin isochromats) having different resonance frequencies. It will be assumed that these spins do not move, i.e., they always feel the same net magnetic field and therefore retain their resonance frequency. One spin isochromat has

a resonance frequency $\omega_o - \Delta\omega$ and the other has a frequency $\omega_o + \Delta\omega$, where ω_o is the Larmor frequency. Thus, immediately after the first RF pulse there will be some transverse magnetization along the y' axis and the magnetizations from both spin isochromats will have the same phase. After the first pulse the isochromats will precess freely in opposite directions with frequency $\Delta\omega$ in the rotating frame, resulting in a loss of phase coherence. The second RF pulse, being a perfect 180° for both spin isochromats, rotates both magnetization vectors about the y' axis by an angle of 180° . Following the second RF pulse the spin isochromats are left to precess freely again, in the same direction as previously so that after a time τ the isochromats will be again in phase and a signal will be formed. After this echo the spin isochromats lose phase coherence again and, as there is no mechanism for reestablishing this, there will be no further signals. It can be easily proved that for a symmetric spin-echo the dispersion contribution is zero, which means that taking the magnitude of the signal gives the absorption component.

A spin-echo has a very useful property: the signal that is dephased due to static field inhomogeneities ΔB_0 can be fully recovered. For this reason the 180° RF pulse is usually called a refocusing pulse as it rephases the phase dispersion developing from ΔB_0 , thereby making this relaxation process reversible.

In a real case the spins dephase due to both T_2 relaxation and field inhomogeneities. The T_2 relaxation process is irreversible, so that that signal amplitude at the time 2τ will be

$$S(2\tau) = S(0) \exp\left(-\frac{2\tau}{T_2}\right) \quad (1.24)$$

where the term $S(0)$ denotes the signal immediately after the first excitation RF pulse. The maximal signal is obtained when $\alpha = 90^\circ$ and $\beta = 180^\circ$.

There is an additional irreversible process due to the fact that spins in a liquid diffuse and they do this in a field that is not homogeneous [5, 17]. This results in an additional loss of phase which is irreversible due to the random nature of diffusion. The complete quantitative description of the spin-echo intensity is given by

$$S(2\tau) = S(0) \exp\left(-\frac{2\tau}{T_2}\right) \exp\left(-\kappa\tau^3\right) \quad (1.25)$$

where the constant κ contains further terms with information about the field inhomogeneity and the diffusion coefficient of the spins [5, 17].

Three RF pulses (stimulated-echoes)

An NMR experiment using three RF pulses can produce eight signals: three FIDs, one immediately following each RF pulse, several spin-echoes and a signal called stimulated-echo [4]. These signals are shown in Figure 1.2 together with the times at which they appear relative to the first RF pulse.

The evolution of the magnetization between the RF pulses and the origin of the different signals could be described by using the magnetization vector model. Instead, the extended-phase-graph method [18] will be introduced. This is an alternative method for describing the origin (and also the amplitude) of the signals in pulse sequences consisting of several RF pulses. It is preferred to the vector model because of its simplicity for visualizing the possibilities that

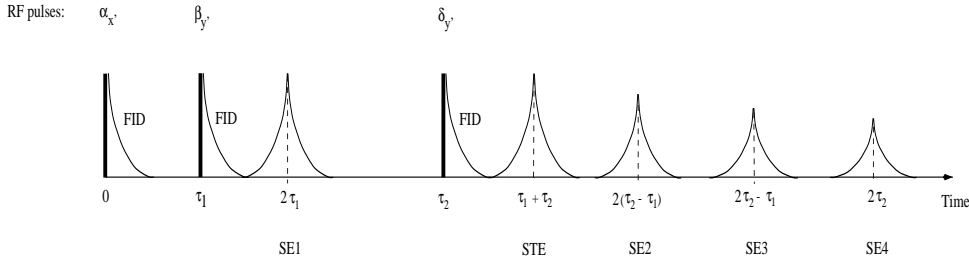


Figure 1.2: NMR signals obtained from three RF pulses: three FIDs, four spin-echoes (SE) and a stimulated echo (STE).

the magnetization has for evolving and forming signals in multipulse sequences. The extended-phase graph method will be described for the case of three RF pulses and applied in the next section for more pulses. A full description of the extended-phase-graph can be found in the literature [18, 19]

Every time an RF pulse is applied, its operation on the transverse magnetization can be described as follows:

- A part of the magnetization continues dephasing as though nothing had happened.
- A part is phase conjugated about the axis of the RF pulse as if a perfect 180° refocusing pulse had been applied.
- A part is rotated to the z -axis where it stops precessing while still keeping information about the phase it had immediately before the pulse.

The distribution of magnetization into the different components is determined by the flip angle of the RF pulses. Thus every time an RF pulse is applied the magnetization is split into different evolving fractions, each describing a different evolution pathway of the spins. These evolving fractions are called coherence pathways.

Figure 1.3 shows the extended-phase graph for a pulse sequence consisting of three RF pulses: $\alpha_{x'} - \tau_1 - \beta_{y'} - \tau_2 - \delta_{y'}$. The RF pulses are represented by vertical lines. No relaxation or diffusion effects are considered. The phase of the transverse magnetization relative to the y' axis is plotted versus time for a spin isochromat having a given (constant) off resonance frequency. The evolution of the phase is shown by solid lines between the pulses and the dotted horizontal lines represent z magnetization. These lines represent the coherence pathways. At every RF pulse the coherence pathways are further split. Refocusing or conjugating the magnetization is equivalent to negating the spin phase. Observable signal comes from pathways crossing the zero phase axis. Longitudinal magnetization does not dephase and the difference between horizontal dotted lines in Fig. 1.3 represent the different phase information that is stored in the longitudinal axis.

The origin of the different signals can be explained as follows. After the first RF pulse some magnetization will be aligned along the y' axis, thus having initial zero phase. Due to field inhomogeneities there will be a phase evolution of the magnetization until the second RF pulse is applied. It is assumed that time-varying effects (flow, motion, field inhomogeneities) are negligible and therefore the dephasing over an arbitrary time interval remains constant along the pulse sequence. The second RF pulse splits the coherence pathway into three new pathways a , b and c (*c.f.* Fig. 1.3) as defined above. In addition, the second RF pulses starts a new pathway.

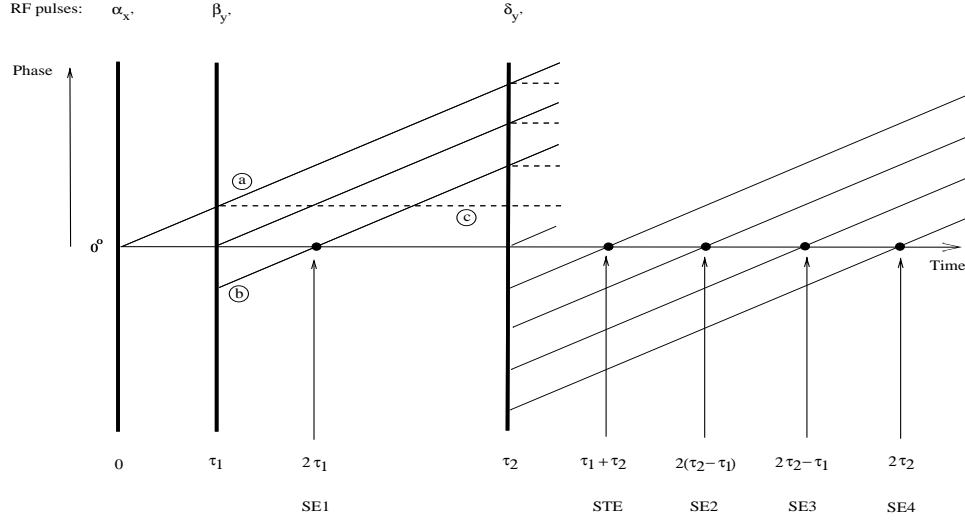


Figure 1.3: Phase graph for possible coherence pathways generated by three RF pulses. The first RF pulse generates a coherence pathway which is split into three components by the second RF pulse: component (a) represents the part of the magnetization that is unaffected by β_y , component (b) represents the part that is perfectly rotated and component (c) (horizontal dotted line) represents the part that is stored along the z -axis. The RF pulse β_y generates itself a new coherence pathway. The process is repeated for each pathway after the third RF pulse. See text for more details.

The first spin-echo (SE1) is formed by the magnetization which is effectively refocused by the second RF pulse. In a similar manner, the signals SE3 and SE4 are also spin-echoes arising from the RF pulse pairs $\beta_{y'} - \tau_2 - \delta_{y'}$ and $\alpha_{x'} - (\tau_1 + \tau_2) - \delta_{y'}$ respectively. The signal SE2 is a spin-echo that results from the refocusing of SE1. Finally, the stimulated echo STE comes from longitudinal magnetization created by the second RF pulse, which is stored in the z axis during the time interval $\tau_2 - \tau_1$ and then brought back to the xy plane by the last RF pulse.

Since the pathway of the stimulated echo goes through both the transverse plane and the z axis, the amplitude of this echo will depend on T_1 , T_2 relaxation and the RF pulse flip angles. All the other pathways remained in the transverse plane so their amplitudes will have information about T_2 relaxation and the pulse flip angles.

It can easily be seen from Fig. 1.3 that the number of coherence pathways rapidly increases with the number of RF pulses. Luckily, as will be shown in the next section, under certain timing conditions several pathways can be made to interfere coherently giving one single signal, thus reducing the number of different signals generated by a multipulse sequence.

Multipulse sequence

A typical example of a multipulse sequence often used in MRI is one that starts with a 90° excitation pulse and is followed by equally spaced 180° pulses such that an echo occurs in the center of the time interval between two refocusing pulses [5]. The sequence of signals is normally called an echo train. If perfect refocusing pulses could be used then the signal decay along the echo train would be determined by T_2 relaxation alone (neglecting the diffusion term). In a real situation, however, the RF refocusing pulses are imperfect. A method that compensates for these imperfections is given by the well known CPMG (Carr-Purcell Meiboom-Gill) sequence where the following condition is imposed: the phase of all the refocusing pulses should be the same and orthogonal to the phase of the first excitation pulse [6]. This is known as the CPMG condition.

Figure 1.4 shows an idealized representation (no time-varying effects) of the extended phase diagram for the CPMG sequence: $\alpha_{x'} - TE/2 - \beta_{y'} - TE - \beta_{y'} - TE - \dots$ where TE is the echo time. It can be seen that because of the periodicity in the spacing of the RF pulses, all the coherence pathways from spin- and stimulated-echoes are brought together to form echo signals at times $TE, 2TE, 3TE, \dots$ from the first excitation pulse. The first signal in the echo train originates from a 'pure' spin-echo (i.e., no stimulated-echo adds to this signal), whereas the following signals are composed by the interference of both spin- and stimulated-echoes. Only the pathways arising from the excitation pulse α are shown. The pathways originating from the refocusing pulses β are not shown because the signals from these pathways become refocused at the same times when the RF refocusing pulses are applied, thus giving no measurable signals.

1.1.7 Magnetic field gradients

Magnetic field gradients are the most important feature in the development of MRI from NMR spectroscopy. They will be introduced at this point because, in addition to allowing spatial information to be encoded in the NMR signal, they can also be used for selecting coherence pathways.

A magnetic field gradient \mathbf{G} in the main field $\mathbf{B} = B_z \mathbf{k}$ is defined by

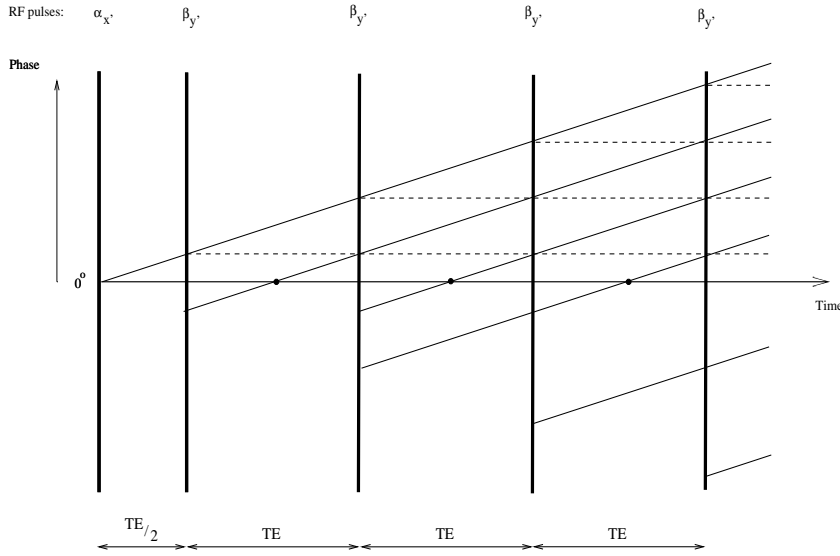


Figure 1.4: Phase graph of possible coherence pathways for a CPMG pulse sequence.

$$\mathbf{G} = \nabla B_z = \left(\frac{\partial B_z}{\partial x}, \frac{\partial B_z}{\partial y}, \frac{\partial B_z}{\partial z} \right) \quad (1.26)$$

Generally, three gradient coil windings are employed, with linear field variation in each of the three primary (x, y, z) directions, producing G_x , G_y and G_z gradients, respectively. In the presence of a gradient, a spin ensemble precessing according to the Larmor equation has a frequency offset from ω_o given by

$$B(\mathbf{r}) = B_0 + \mathbf{G} \cdot \mathbf{r} \Rightarrow \omega(\mathbf{r}) = \gamma(B_0 + \mathbf{G} \cdot \mathbf{r}) \quad (1.27)$$

Thus, in presence of a gradient the resonance frequency is proportional to the position of the spins along the gradient direction. If a gradient \mathbf{G} is applied, then at a time t the phase $\phi(t)$ of the transverse magnetization describing a spin isochromat will be

$$\phi(t) = \gamma \int_0^t \mathbf{G}(t') \cdot \mathbf{r}(t') dt' \quad (1.28)$$

where it has been assumed that the isochromat has zero phase at $t = 0$. A gradient field has no effect on longitudinal magnetization because this, by definition, has no phase. If motion of the spins is neglected, the dephasing effect of a gradient can be refocused by using exactly the same gradient with the same duration but with opposite polarity (i.e., $-\mathbf{G}(t)$). When two such pulses are applied between two consecutive RF pulses the total dephasing will be zero and no coherence pathway will be affected. However, a coherence pathway can be dephased (and therefore any signal coming from it eliminated) by properly choosing the position and strength of a gradient pulse in a multipulse sequence. If the spins move in the presence of a bipolar

gradient it can be seen from eq. (1.28) that there will be a phase accumulation which may be used to detect motion [20].

To illustrate how magnetic field gradients can have an effect on coherence pathways, Fig. 1.4 will be reconsidered. It will now be assumed that between the RF pulses there is a pulsed magnetic gradient as shown in Fig. 1.5A for the first three refocusing pulses. During the periods in which the gradient is zero the magnetization retains its phase without further dephasing. The pulsed gradient corresponds to the read or frequency encoding gradient used during signal acquisition in a MR-imaging experiment (*c.f.* section 1.2.3). Thus, it will be assumed that the signals are measured during the refocusing periods when the pulse gradient is on. The time interval during which the signal measurement is performed is called the acquisition window.

It can be seen that the essential features of Fig. 1.4 and Fig. 1.5A are identical if the time integral over the pulsed gradient in all refocusing pulses remains constant and equal to twice the integral over the gradient between the excitation pulse and the first refocusing pulse. This condition ensures that the dephasing effects of the gradient are refocused. The polarity of the gradient needs not to be changed due to the fact that the refocusing pulses already invert the phase of the magnetization. In this situation the CPMG condition holds and, except for the first 'pure' spin-echo, spin- and stimulated echoes interfere coherently at the center of the acquisition windows along the echo train.

If the latter integral condition is not fulfilled, as illustrated in Fig. 1.5B, then spin- and stimulated echoes will no longer interfere coherently [19, 21, 22, 23]. In Fig. 1.5B only the pathways which contribute to echo formation during the first three refocusing intervals are shown. The effect of having an imbalanced gradient is to split the pathways so that in each acquisition window (except the first one) two signals will form. These signals can be classified as being odd or even echoes according to the number of intervals that the magnetization has spent in the transverse plane before being refocused to form the echo [22]. If time-varying effects like flow or motion can be neglected, then odd and even echoes will be formed at the same time points within each acquisition window along the echo train. The definition of the two echo groups may be further developed by considering them as belonging to two separate families [22]: family SE , that occurring simultaneously with the repeated direct refocusing of the first spin-echo SE_1 ; and family STE , that occurring simultaneously with the direct refocusing of the first stimulated-echo STE_1 . The relative intensity of the two families is determined by the refocusing angle β . If $\beta = 180^\circ$, then only pure spin-echoes will be generated and family STE will not exist. By following the pathways in Fig. 1.5B, it can be seen that odd and even echoes come alternatively from the SE and STE families. It should be noted that the echo families SE and STE can contain both spin- and stimulated echoes (e.g., SE_3 in Fig. 1.5B).

The example illustrated in Fig. 1.5B shows a case in which the dephasing action of an imbalanced gradient modifies the coherence pathways so that stimulated- and spin-echoes do not add coherently and therefore the CPMG condition is no longer fulfilled. These considerations will become important when considering methods for making a similar multi-echo sequence independent from the CPMG condition (*c.f.* section 4.2).

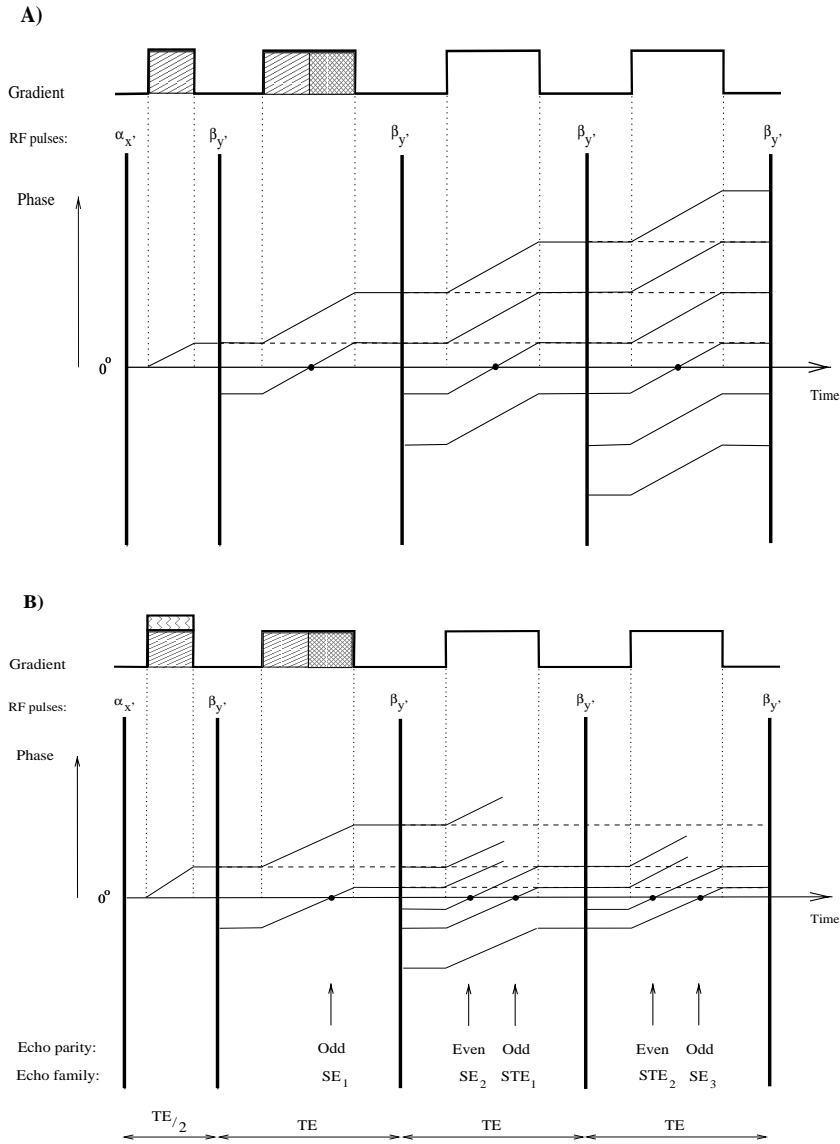


Figure 1.5: Phase graph of multi-echo CPMG sequences where the dephasing between RF pulses is produced by a pulsed magnetic field gradient. In **A)** the gradient rephases the signals midway between the RF refocusing pulses by having the shaded areas equal. All essential features are identical to those shown in Fig. 1.4. In **B)** the gradient is imbalanced by increasing the net dephasing during the excitation pulse and the first refocusing pulse (vertical shaded area). The other shaded areas remain equal. The effect of the gradient imbalance is to separate the coherence pathways of odd and even echoes. The points along the time axis indicate the times when the different coherences refocus to form an echo. See text for more details.

1.2 Basic principles of MRI

In this section the basic methods for encoding spatial information in a NMR signal will be discussed. The k -space formalism, which will be introduced first, is a very useful tool that permits the interpretation of the MR signal from a perspective of the acquisition of spatial frequency data [9, 24]. The most common methods for encoding spatial information in the NMR signal will be then discussed.

1.2.1 k -space

The application of a single RF pulse generates magnetization M_{xy} on the transverse plane, where M_{xy} satisfies the Bloch equations 1.18. The signal induced in the receiver coil is proportional to M_{xy} . Thus, in the absence of relaxation, flow and diffusion effects the measured signal may be expressed as

$$S(t) = M_{xy} \exp(i\omega_0 t) \quad (1.29)$$

If we now consider an extended sample with spin density $\rho(\mathbf{r})$, then an elemental volume dr^3 at the position \mathbf{r} will have a magnetization $\delta M(\mathbf{r}) = \rho(\mathbf{r}) dr^3$ and the total measured signal will be given by a volume integral of the signal over the whole sample

$$S(t) = \int \rho(\mathbf{r}) \exp(i\omega_0 t) dr^3 \quad (1.30)$$

An arbitrary time-varying gradient $\mathbf{G}(t)$ causes the spins to dephase in the transverse plane of the rotating frame. The phase accumulated by a stationary spin after a time t is

$$\phi(\mathbf{r}, t) = \gamma \int_0^t \mathbf{G}(t') dt' \cdot \mathbf{r} \quad (1.31)$$

We may neglect the ω_0 term in equation (1.29) by considering that the measured signal is electronically mixed with a reference signal of the same frequency so that the deviations from the resonance frequency are sampled. By integrating the effects of the gradients over time, and assuming no relaxation

$$S(t) = \int_V \rho(\mathbf{r}) \exp(i\phi(\mathbf{r}, t)) dr^3 \quad (1.32)$$

Introducing the so-called k -space conjugate variable [9, 24] by defining

$$\mathbf{k}(t) = \frac{\gamma}{2\pi} \int_0^t \mathbf{G}(t') dt' \quad (1.33)$$

makes the Fourier imaging relationship clear

$$S(\mathbf{k}) = \int_V \rho(\mathbf{r}) \exp(i2\pi \mathbf{k} \cdot \mathbf{r}) dr^3 \quad (1.34)$$

$$\text{so that } \rho(\mathbf{r}) = \int_K S(\mathbf{k}) \exp(-i2\pi \mathbf{k} \cdot \mathbf{r}) dk^3$$

Equations (1.34) express a fundamental relationship applicable to all MRI methods. These equations state that k -space is the spatial frequency domain in which the data are collected.

Thus, by measuring the signal $S(\mathbf{k})$ (a process known as 'sampling k -space') the spatial distribution of the spin density can be obtained from a Fourier transform of the measured data. This is, however, an approximation since it was assumed that the phase of the magnetization is only determined by the variable $\mathbf{k}(t)$ defined in eq. (1.33). In many applications these simplifications are no longer valid and the Fourier transform of the measured data will not give the spin distribution $\rho(\mathbf{r})$. The effects of relaxation will be considered in a later section where the point spread function formalism is introduced.

Digital computers, controllers and sampling systems require the collection of discrete data. Therefore, equations (1.34) have to be substituted by discrete Fourier transforms to reconstruct the data. A two-dimensional image of an object can be obtained by selecting a slice (*c.f.* section 1.2.2) through the object and then restricting ourselves to spatially encoding two spatial dimensions. For a two-dimensional spin distribution on the plane xy being sampled by N discrete points along the x - and y -axis

$$\rho(x, y) = \frac{1}{N} \sum_{y=-\frac{N}{2}}^{\frac{N}{2}-1} \sum_{x=-\frac{N}{2}}^{\frac{N}{2}-1} S(k_x, k_y) \exp(-i 2\pi (k_x x + k_y y) / N) \quad (1.35)$$

As the time integral of $\mathbf{G}(t)$ defines the k -space position, it is in principle possible to sample k -space using a variety of methods. However, the advantages given by the fast Fourier transform to rapidly reconstruct the acquired data into images favours the use of sampling strategies with a regular pattern in k -space [24]. One of the most popular sampling arrangements consists in collecting the data from a Cartesian or rectangular grid. The path through the k -space and the succession of the acquired k -space data $S(k_x, k_y)$ is called the k -space trajectory.

The rectangular grid in the image space is defined by the pixel size δr and the number of pixels N_r , where r denotes any of the x - or y -axes. The image dimensions are defined by the product $\delta r \cdot N_r$ which give the so-called field of view or FOV. The dimensions of the grid in k -space can be calculated from these parameters. Using the Larmor equation, the definition of k -space and the Nyquist sampling criterion [25] to ensure that the intersample separation is small enough to avoid aliasing, it follows that

$$(\text{FOV})_r = \frac{1}{|\delta k_r|} \quad \text{and} \quad \frac{(\text{FOV})_r}{N_r} = \delta r = \frac{1}{|k_r|} \quad (1.36)$$

where δk_r is the distance between consecutive samples in k -space and $|k_r|$ is the extension of k -space from the center along any of the directions (x or y) defined by r .

1.2.2 Selective excitation

The frequency selectivity of a soft RF pulse applied in the presence of a field gradient, will be manifested as a spatial selectivity [26]. This method is schematically described in Figure 1.6. Suppose that the main field B_0 is along the z direction and that a linear magnetic gradient G_{slice} is applied in this direction such that

$$\omega(z) = \gamma (B_0 + G_{\text{slice}} z) \quad (1.37)$$

Thus, in presence of the gradient G_{slice} we can regard the z -axis as being also a frequency axis. Assume that we want to selectively excite only those spins which are in the slice defined by

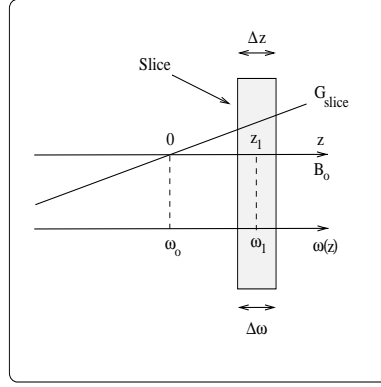


Figure 1.6: Principles of slice selective excitation. When the linear gradient G_{slice} is applied, the z -axis is also a frequency axis. Thus, a RF pulse with frequency $\omega_1 = \omega(z_1)$ and excitation bandwidth bw_p will selectively excite the spins in a slice centred at z_1 with thickness Δz .

the position z_1 and the thickness Δz . By considering the frequency axis, we can see that the desired slice would be excited by a RF pulse oscillating at the frequency $\omega_1 = \omega(z_1)$ and having a pulse bandwidth bw_p given by

$$bw_p = \gamma G_{\text{slice}} \Delta z \quad (1.38)$$

The pulse bandwidth bw_p is defined by the chosen pulse shape and pulse duration, which are usually user-defined in addition to the slice position and slice thickness. Therefore, the usual method is to calculate the strength of G_{slice} , also called the slice selection gradient, from equation (1.38) and then the frequency of the RF pulse from equation (1.37).

Ideally, the frequency response of the RF pulse should be a rectangular function that excites only the desired bandwidth bw_p . In practice, it is not possible to obtain a slice profile of rectangular cross section due to the fact that the slice excitation RF pulse has to be applied during a finite (and preferably short) time. The temporal modulation of the RF-pulse determines the slice-profile, and for small excitation angles ($< 60^\circ$) the slice profile can be approximated by the Fourier transform of the time domain representation of the RF-pulse [27]. The effective slice thickness is usually defined as the full width at half maximum of the slice profile. For larger excitation angles the slice profile is further affected by the non-linearity of the Bloch equations [27]. Optimized RF pulses can be obtained by analytical [28, 29] and numerical methods [30, 31]. These RF pulses can give a more uniform slice profile but they are not normally used in fast imaging sequences because they require higher RF power deposition and they usually have a high bandwidth, thus requiring much stronger slice gradients to excite the same slice thickness (eq. (1.38)).

From eq. (1.37) it can be seen that when the slice gradient is turned off after the RF pulse, the spins along the z -direction will be dephased because they had different resonance frequencies whilst the RF pulse was applied. If the shape of the RF pulse is symmetric, it is necessary to rephase the spins otherwise there will be no net signal coming from the selected

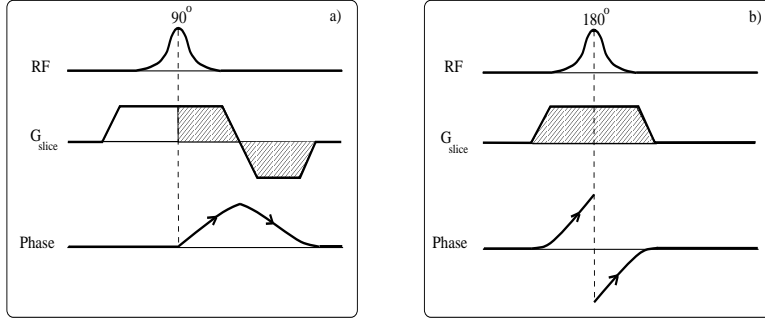


Figure 1.7: a) An 90° RF pulse is effectively applied at the center of the pulse duration interval. From this time onwards spins at different positions through the slice will dephase from each other due to the gradient G_{slice} . A slice rephasing gradient with opposite polarity can be applied to rephase the excited magnetization in the slice. The shaded areas under the gradient waveform (i.e., the net dephasing) must be equal. b) For a 180° RF pulse phase differences are cancelled out if the slice gradient is symmetric around the center of the 180° RF.

slice. To bring the spins back in phase a rephasing slice gradient is applied. The strength and duration of this gradient are normally calculated so that the area under the rephasing gradient (i.e., the net rephasing) equals half the area of the slice excitation gradient under the RF pulse [32]. This is schematically shown in Figure 1.7a, which shows the pulse sequence diagram for a slice selective excitation pulse. Figure 1.7b shows the situation for a 180° pulse. For such a pulse a slice rephasing gradient is not necessary due to the refocusing action of the RF pulse. The transverse magnetization exists for the entire time that the slice selection gradient for 180° is on. At the center of the pulse the 180° will be effectively applied and the phase conjugated. Thus, if the slice gradient is symmetric around the RF pulse, phase changes will cancel out. Self-refocusing RF pulses have also been developed [33], and by definition these do not require a rephasing gradient.

1.2.3 Frequency and phase encoding

Let us assume that a slice has been selected transverse to the z -axis. To form a two-dimensional image of this slice the NMR signal from the $(x-y)$ plane has to be spatially encoded to discriminate between spins in different parts of the slice. One method for doing this is frequency encoding, in which the signal is measured with a magnetic gradient present, say G_x along the x -axis. As mentioned previously (*c.f.* section 1.1.7), the effect of a magnetic gradient is to make the resonance frequency a linear function of position along the gradient direction

$$\omega(x) = \gamma x G_x \quad (1.39)$$

Thus, the amplitude of the signal at a particular frequency is proportional to the number of spins (amount of material) at the corresponding x -position. If a FID is obtained with a gradient

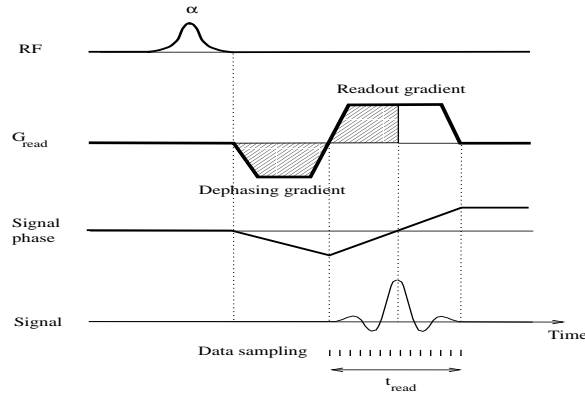


Figure 1.8: Gradient sequence showing a gradient echo.

present, a Fourier transform of the signal gives a one-dimensional projection of the object along the direction of the gradient. Such a gradient is called a *readout gradient*.

Problems arise if one attempts to measure the FID immediately after excitation, with the readout gradient present. It is important not to miss the start of the FID because it contains the low spatial frequency information. Thus, it is preferable to record the signal as an echo, generated either by a 180° RF pulse or by a reversal of the readout gradient. The latter is called a *gradient echo*. Figure 1.8 illustrates how a gradient echo is formed. The spins are first dephased with a negative gradient pulse immediately following the RF pulse, and they are then rephased by the readout gradient. The NMR signal is sampled for example 128 times for a 128 pixel wide image.

Another method for spatial discrimination is phase encoding, which can be understood by examining the behaviour of spins during the readout period, and considering the net phase changes occurring between consecutive data samples. It can be seen that the 128 numbers representing the signal strength variation during the readout period could have been obtained not by observing the signal in the presence of a gradient but by performing 128 RF excitations followed each time by a different sized dephasing or *phase-encoding* gradient pulse before sampling the signal once. This technique is known as phase-encoding because it is the phase of the precessing magnetization which depends on position along the gradient direction.

A two-dimensional image can be therefore obtained by combining frequency and phase-encoding using two orthogonal magnetic gradients along orthogonal directions in the imaging plane. This MRI method is called spin-warp imaging [34]. Figure 1.9 schematically shows a conventional gradient-recalled echo (GRE) sequence (Fig. 1.9, left) with its k -space trajectory for data acquisition (Fig. 1.9, right). We assume a slice selective excitation oriented along the slice selection gradient G_{slice} perpendicular to the phase-encoding G_{phase} and read G_{read} gradient directions. If an image consists of N_{read} and N_{phase} points (pixels) along the read- and phase-encoding directions, then k -space will consist of a rectangular grid with the same number of points along the corresponding directions. The G_{phase} gradient has a constant duration and varies its amplitude, starting with a negative amplitude, in constant steps to sample the

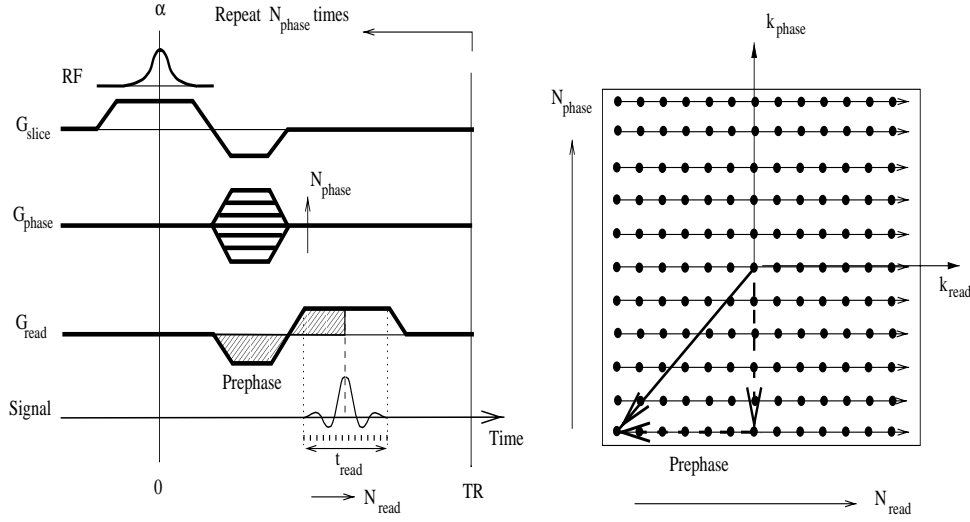


Figure 1.9: Conventional 2D-GRE sequence (left) and corresponding k -space trajectory (right). The k -space data lines are acquired from left to right.

coordinates along the phase-encode direction. To fully sample k -space, N_{phase} phase-encoding amplitudes will be needed, the spacing and the extensions of the k -space coordinates being defined by equation (1.36). The prephasing lobe of the G_{read} in combination with the first G_{phase} gradient amplitude define the starting point (lower left edge of k -space) for the first k -space data line, or first phase-encoding step. During the acquisition time t_{read} , the first line of k -space is acquired and N_{read} data points are measured. During this time, the coordinate $k_{\text{read}} = \gamma G_{\text{read}} t / (2\pi)$ varies linearly with time. After the repetition time, TR , during which the longitudinal magnetization is left to relax, the RF excitation pulse is repeated, and the G_{phase} gradient amplitude is increased defining the start position for the second k -space data line, or second phase-encoding step. This procedure is repeated until all k -space has been sampled.

From all the acquired echoes the one with strongest signal intensity is the one acquired when the phase gradient is zero. For this echo, the only dephasing occurs in the k_{read} direction through G_{read} during acquisition. Thus, the Fourier transform of this echo gives the one-dimension projection or profile of the imaged object along the x_{read} direction.

The strength of the G_{read} gradient is defined by the FOV in the read direction and the sampling bandwidth bw_s of the low-pass frequency filter that is used in the receiver. The sampling bandwidth also defines the sampling rate δt , which is set according to Nyquist theorem, and hence the acquisition time for each k_{read} line ($t_{\text{read}} = N_{\text{read}} \delta t$). The choice of the sampling bandwidth bw_s is important because it affects the amplitude of the random noise (proportional to $bw_s^{-1/2}$) allowed by the filter.

1.2.4 Artifacts: the PSF formalism

We saw that in an ideal situation the 2D spin spatial distribution $\rho_{(x,y)}$ of a sample can be obtained from the 2D Fourier transform of the MR signal $S(\mathbf{k}_{(t)})$ (eq. 1.34). This is only true if the amplitude and phase of the MR signals are purely defined by the spatial encoding gradients. In other words, the assumption of this ideal situation is that all non-phase-encoded echoes have constant signal amplitude and constant phase. This is not true in many situations, particularly in single shot imaging methods (*c.f.* next section), where the signal amplitude typically decays and off-resonance phase errors may evolve during the experiment.

To describe a more realistic situation the previous assumptions are dropped. In addition, the finite sampling window is considered. Without loss of generality the discussion is made in the following for the one-dimensional case. From eq. (1.34), in presence of a field gradient G such that $k(t) = \gamma G t / (2\pi)$ and including the relaxation effects during acquisition $A(k_{(t)})$ and off-resonance spin effects $P(k_{(t)})$, the normalized free induction decay can be described by

$$S(k_{(t)}) = \text{rect}(t/T) \int_{-\infty}^{\infty} \rho_{(r)} e^{i 2\pi k r} A(k_{(t)}) P(k_{(t)}) dr \quad (1.40)$$

where r represents the one-dimensional spatial position. The integration can be performed to infinity because the spin density $\rho_{(r)}$ is limited. The term $A(k_{(t)})$ depends on the relaxation times (T_1, T_2, T_2^*) and describes the signal decay that occurs while k -space is sampled. Thus, the general form of this term will be some sort of exponential decay where the relaxation times involved will depend on the particular imaging sequence considered. The term $P(k_{(t)})$ describes the off-resonance phase errors, which depend mainly on magnetic field inhomogeneities ΔB_o and chemical shift (e.g. fat) frequency offsets. As this term describes purely phases, it will generally have the form of a complex exponential. The functions $A(k_{(t)})$ and $P(k_{(t)})$ will be often referred to as the amplitude and phase modulations of the signal in k -space. When such effects are not present then these functions are defined as unity. The finite sampling duration (T) is accounted for by introducing the rectangle function $\text{rect}(t/T)$ defined by

$$\text{rect}(t/T) = \begin{cases} 1 & \text{for } \frac{-T}{2} < t < \frac{T}{2} \\ 0 & \text{otherwise} \end{cases} \quad (1.41)$$

To calculate the Fourier transform of eq. (1.40) the convolution theorem can be used [25]: this says that the Fourier transform (F) of the product of two functions g and h is the convolution (\otimes) of the single Fourier transformed functions

$$F(gh) = F(g) \otimes F(h)$$

Using the convolution theorem and assuming that the amplitude $A(k_{(t)})$ and phase $P(k_{(t)})$ functions are spatially constant, the Fourier transform of eq. (1.40) gives

$$F(S(k)) = \rho'(r) = \rho(r) \otimes \text{PSF}(r) \quad (1.42)$$

with

$$\text{PSF}(r) = \text{sinc}\left(\frac{\gamma G T r}{2\pi}\right) \otimes \int_{-\infty}^{\infty} A(k) P(k) e^{-i 2\pi k r} dk \quad (1.43)$$

where it was used that the Fourier transform of the rectangle function is a sinc function ($\text{sinc}(x) = \sin(\pi x)/(\pi x)$).

Equation (1.42) indicates that the measured spin density distribution $\rho'(r)$ as the Fourier transform of $S(k)$ is the true spin density $\rho(r)$ convoluted by a function $\text{PSF}(r)$. PSF stands for point spread function.

From a mathematical point of view, the PSF describes the way in which a point object is depicted by an imaging method. From eqs. (1.42) and (1.43) it can be seen that the measured spin density $\rho'(r)$ will be identical to the real $\rho(r)$ distribution only in the situation when the acquisition time T is infinite and when there are no amplitude and phase modulations. In this ideal situation the PSF will be a delta function. The fact that the measuring time is limited transforms the ideal PSF into a sinc function centred at the position of the point source ($x = 0$).

The width at half maximum of the PSF gives a measure of the achievable spatial resolution. The magnitude of the PSF at the position $x = 0$ gives a measure of the pixel intensity.

When amplitude and phase modulations are present the PSF deteriorates further. This can be reflected by a broadening of the central peak (related to a poorer spatial resolution), by the appearance of extra side lobes (related to image intensity away from the central point and thus to image artifacts), and by a decreased pixel intensity (which is a direct consequence of the signal broadening). Thus, different k -space trajectories or different pulse sequences can be compared by comparing their corresponding PSF and predictions can be made regarding spatial resolution, artifacts and signal intensity for the various methods.

It can be seen from equations (1.40) that when no relaxation and off resonance effects take place ($A(k) = P(k) = 1$), the signal $S(k = 0)$ measured at the center of k -space is proportional to the total magnetization available and hence to the image intensity. When relaxation effects occur, the magnitude of the signal measured at $k = 0$ will reflect these effects and the image is weighted by the relaxation parameters.

In this analysis, it was assumed that the amplitude and phase functions were spatially constant. Although this will generally not be true, eq. (1.42) and (1.43) still hold true over a small area where the functions $A(k_t)$ and $P(k_t)$ can be assumed to be constant. Thus, the effective PSF can in principle vary across the image as a function of each pixel's relaxation and inhomogeneity characteristics.

1.3 Fast imaging sequences

To investigate brain function with MRI (*c.f.* section 1.4) it is desirable to have imaging methods which can acquire the data for a whole image in a time-scale comparable to that in which blood flow changes may occur. Sub-second imaging times are therefore a requirement if dynamic processes are going to be followed in large areas of the brain by the acquisition of multiple slices.

Sub-second imaging sequences can be divided into two main categories: those relying on rapidly repeated RF excitation (usually at low flip angles), like the snapshot FLASH method [35, 36], and techniques that create an echo train from a single RF excitation (also called single-shot techniques).

Snapshot FLASH is a gradient-echo imaging technique similar to that illustrated in Fig. 1.9 where each phase-encoded acquisition follows the previous with minimal recovery delay for the

longitudinal magnetization. Ideally, the flip angle is adjusted so that the transverse component of the magnetization is the same for each phase-encoding step. For FLASH it follows that the shorter the experimental time is, the lower the optimum flip angle has to be in order to ensure a constant transverse magnetization during the experiment [37]. Therefore, although FLASH can give very good quality images for subsecond imaging times, due to the low flip angle pulse, the SNR from FLASH images is lower than the SNR obtainable from single shot techniques [37]. Furthermore, for functional brain imaging a strong T_2^* weighting (i.e., $\simeq 30$ ms) is required for optimal functional sensitivity (*c.f.* section 1.4). This T_2^* weighting can be incorporated in FLASH based sequences by using a long echo time ($TE \simeq 30$ ms). This has the disadvantage that the total experimental time is considerably increased (e.g., an image formed with 64 echoes would take $\simeq 2$ s). The data acquisition efficiency can be improved by exciting additional slices during the TE period [38]. This, however, increases the sensitivity of the sequence to motion (through the use of multiple bipolar slice gradients) thus limiting its application to a few slices [39].

For detecting small signal changes like those occurring in the brain due to haemodynamic changes, having the highest possible SNR together with high temporal resolution is a basic requirement, hence single-shot methods are normally preferred. In the following sections the essential features of three basic single-shot MR imaging sequences will be summarized.

1.3.1 Echo Planar Imaging (EPI)

In echo planar imaging (EPI) the information required to form an image is obtained under the FID of a single excitation [40] allowing images to be acquired within 30-100 ms with currently available hardware [41].

The gradient echo EPI sequence (GE-EPI) with the corresponding k -space trajectory is illustrated in Figure 1.10. In conventional GRE techniques a single echo is used to scan one line in k -space (Fig. 1.9). In EPI the addition of the bipolar oscillating gradient along the frequency-encoding direction permits the generation of an echo-train, and each of the echoes may then be independently phase-encoded. Due to the bipolar read gradient, consecutive lines along k_{read} will traverse k -space in opposite directions giving rise to odd and even echoes. The phase-encoding is performed by usually using first a negative gradient that defines the starting position in k -space followed by short duration gradients 'blips' occurring between consecutive read periods. Each phase-encoding blip gradient moves the k -space trajectory one step further along the k_{phase} direction after each acquisition. Thus, after one excitation it is possible to sample k -space acquiring all the necessary data to form an image.

The advantages of EPI are that high SNR images can be obtained in a very short time. The main disadvantage of EPI is that the signal is measured while undergoing T_2^* decay. Signal decay means the decay observed in the intensity of the NMR signals along the echo train when the phase-encoding gradient is switched off. Such an experiment is also called a template or reference scan, and it is useful for correcting time and phase errors during the process of image reconstruction (*c.f.* section 3.2).

The T_2^* decay limits the total time during which useful signals can be spatially encoded hence limiting the achievable spatial resolution, specially in areas of the image with short T_2^* . The number of echoes collected could in theory be increased by using faster switching gradients. The speed of gradient switching is, however, limited by the hardware and, most importantly, by

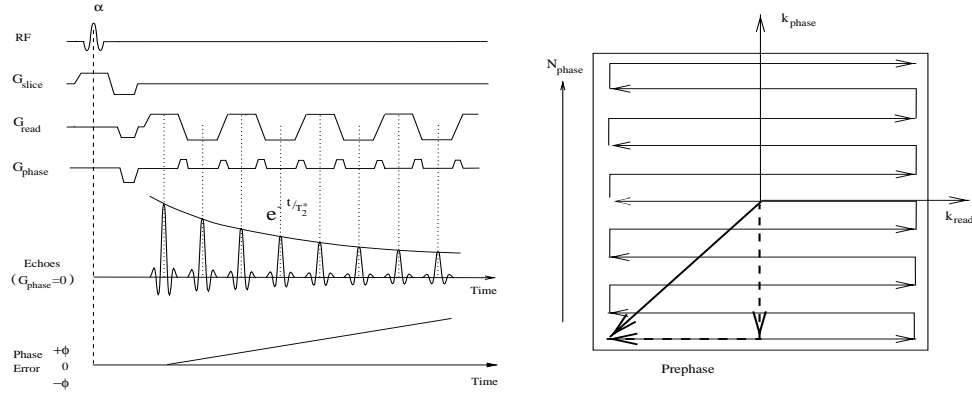


Figure 1.10: GE-EPI sequence (left) and corresponding k -space trajectory (right). The odd and even data lines traverse k -space in opposite directions.

the physiological effects on neuronal stimulation due to the time-varying magnetic fields [41]. Another consequence of the T_2^* decay during acquisition is that the dephasing from off-resonance spins increases linearly with the length of the echo train, as shown in Fig. 1.10. Using the PSF formalism it can be seen that these relaxation and dephasing effects result in image artifacts which are particularly strong in the phase-encoding direction because this is the direction in k -space where the PSF most deteriorates [42]. The artifacts can be reduced by having a shorter echo train. Shorter echo trains can be obtained by reducing the area of k -space that is sampled after the RF excitation. With single shot imaging this would result in a reduction of the spatial resolution. The spatial resolution can be maintained or increased by performing multishot imaging. In this case the data for an image is acquired after several RF excitations, each sampling a different fraction of k -space in an interlaced fashion. Multishot imaging can be done using long repetition times between segments to let the magnetization recover with the disadvantage of lower temporal resolution than single shot imaging. Alternatively, multishot imaging can be also done using a very short repetition times at the cost of SNR and a greater sensitivity to system stability [43].

An additional disadvantage of EPI is the fact that a read gradient of alternating polarity is used to acquire odd and even echoes. Hardware imperfections can give rise to differences between these echoes [41] and these mismatches are manifested in EPI as duplicate images of the object, called $N/2$ or Nyquist ghosts, and if severe, they can degrade image quality.

From Fig. 1.10 it can be seen that the center of k -space can be reached only after the signal has undergone some T_2^* decay. As the center of k -space defines the image intensity, GE-EPI images will show T_2^* contrast. If k -space is sampled symmetrically in the phase-encode direction, i.e., when the maximum and minimum values of k_{phase} have the same magnitude as shown in Fig. 1.10 (right), then the T_2^* -weight will be defined by half the length of the echo train. A shorter T_2^* -weighting can be achieved by sampling k -space asymmetrically so that the center of k -space is reached at an earlier point in the echo train. This method of reducing the intrinsic T_2^* contrast in GE-EPI is, however, limited due to the image artifacts that arise when

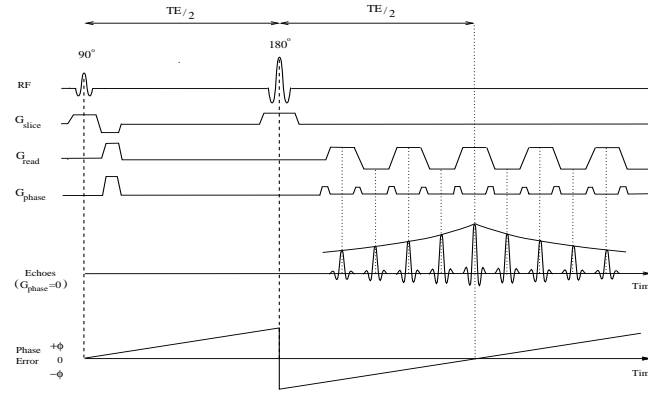


Figure 1.11: SE-EPI sequence.

an excessive asymmetry in k -space is used.

The sensitivity of EPI to phase errors can be reduced by using a RF refocusing pulse, as illustrated in Figure 1.11. With this method (spin echo EPI, or SE-EPI), static field inhomogeneity effects are rephased at the spin echo time. Thus, by keeping the same echo train length the maximum dephasing is halved at the cost of a lower SNR due to the T_2 decay. If the center of k -space is sampled at the spin echo time TE , then the image will show T_2 contrast. A pure T_2 contrast will not be possible due to the fact that during the whole acquisition the signal suffers from various degrees of T_2^* weighting. The minimum achievable T_2 contrast is defined by $TE \approx ETL$, where ETL is the echo train length.

It is possible to incorporate T_2^* weighting in a SE-EPI image by reducing the time interval between the excitation RF pulse and the RF refocusing pulse, for example by an amount τ . If the center of k -space is still measured at the center of the echo train, then the delay τ will define the amount of T_2^* weighting. This method is known as asymmetric SE-EPI. In this sequence the echo time TE can be reduced to be $TE = ETL - \tau$ thereby reducing the intrinsic T_2 contrast while incorporating T_2^* contrast.

To summarize, the well known result is that EPI allows fast image acquisition but EPI images can show ghosting, geometric distortions and signal loss due to signal dephasing [41]. Image distortion and signal loss problems become worse in regions with strong field inhomogeneities. To minimise these effects several factors must be taken into account, including special hardware design, special sampling techniques and special image reconstruction algorithms, making the implementation of EPI difficult, particularly at high main field strengths [41].

1.3.2 Rapid Acquisition with Relaxation Enhancement (RARE)

The rapid acquisition with relaxation enhancement (RARE) technique creates a train of spin-echoes by using a train of RF refocusing pulses [44]. Each spin-echo can be separately phase-encoded allowing the possibility of the image data to be acquired after a single excitation. Figure 1.12 illustrates the RARE pulse sequence with the corresponding k -space trajectory. As

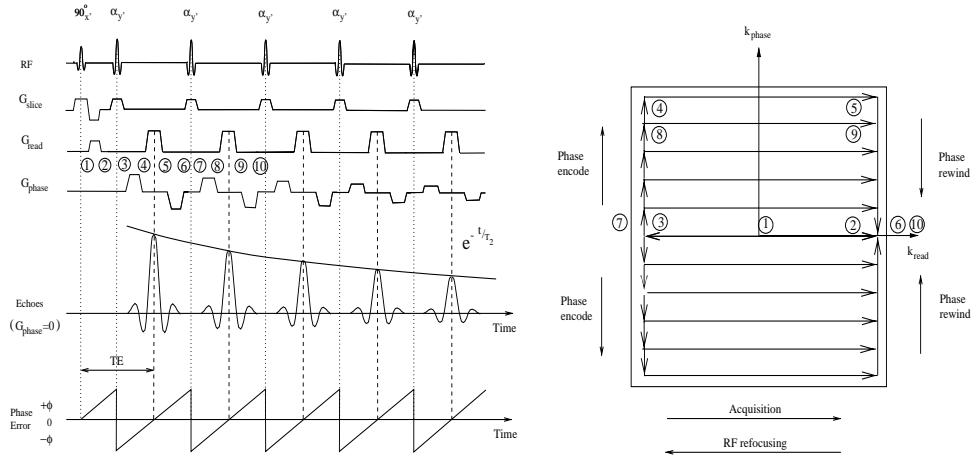


Figure 1.12: RARE sequence (left) with corresponding k -space trajectory (right). The numbers are used as reference to illustrate how the trajectory in k -space is formed.

shown in Fig. 1.5A, the prephase read gradient lobe has the same polarity as the read gradient during signal acquisition. This is necessary due to the rephasing action of the RF refocusing pulses on the presence of the slice gradient, the net effect in k -space being a 180° rotation of the vector \mathbf{k} about the k_{slice} . To show how the k -space trajectory is formed, ten time points have been marked in the RARE sequence (Fig. 1.12, left) with their corresponding k -space coordinates (Fig. 1.12, right).

The RF refocusing pulses are equally spaced and the CPMG condition is used to ensure that all possible magnetization pathways interfere coherently. To ensure that the coherences remain unchanged between the RF pulses a rewinder phase-encoding gradient is applied after each acquisition and before the following RF pulse (*c.f.* Fig. 1.12, left). This rewinder gradient is important because it cancels out the dephasing introduced by the preceding phase-encoding gradient preventing therefore that later phase-encoded echoes be affected. In addition, the coherent superposition of echoes offers the possibility of using refocusing pulses with reduced flip angles without serious loss of signal amplitude [18]. Furthermore, rewinding of the phase-encoding gradient gives total freedom regarding the sequence of phase-encoding steps, allowing the possibility achieving different image contrasts [44, 45]. The ways by which the sequence of phase-encoding steps can affect image contrast and image quality will be discussed in more detail in the following chapter.

An advantage of RARE versus EPI is the fact that in RARE off resonance effects are perfectly refocused. Therefore, RARE images are much less sensitive to field inhomogeneities than EPI. Other advantages of RARE are that no fast switching gradients are in principle required and that all echoes are acquired with the same gradient polarity hence imposing less demanding hardware and / or software requirements than EPI. In addition, RARE does not need special image reconstruction algorithms like EPI does to correct for phase errors and geometrical distortions. Thus, RARE is easier to implement than EPI.

Assumed the signal decays exponentially with a time constant given by T_2 , that there are no phase errors and that the signal is measured for an infinitely long acquisition time, then using eq. (1.43) it can be seen that in the frequency domain the PSF of a RARE sequence will be a Lorentzian function with a line-broadening given by $1/(\pi T_2)$. The PSF will not degrade the spatial resolution if its width is smaller than the frequency difference between adjacent points in the frequency domain of the phase-encode directions. Using the Nyquist sampling theorem it can be seen that this will be achieved if $N_p TE \leq \pi T_2$, where N_p is the number of echoes acquired per excitation.

In most cases, particularly when RARE is used for fast imaging, the refocusing pulses α will not generate perfect 180° pulses through an excited slice. Lower refocusing angles will generate longitudinal magnetization that is brought at some later stage into the transverse plane to form stimulated echoes, making the signal decay a complicated function of TE , α , T_2 and T_1 . For the case when T_2 is short compared to T_1 , this can lead to an appreciable lengthening in the life time of the transverse magnetization compared to that expected from T_2 alone. This may be an advantage because it gives more time during which more echoes can be acquired after a single excitation.

Disadvantages of RARE compared to EPI are that the RARE method is slower (it is faster to switch gradients and acquire gradient echoes than to apply RF refocusing pulses to acquire spin echoes) and that significantly more RF power is needed per RARE image. The RF power deposited by RARE images can be reduced by applying lower refocusing flip angles at the cost of losing SNR. RF power can become a real limitation when large areas of the brain are to be covered with multislice acquisition and short repetition times, particularly when imaging at high field.

1.3.3 Gradient and Spin Echo Imaging (GRASE)

The gradient and spin echo imaging (GRASE) method is a relatively new hybrid imaging method [46] that combines features of EPI and of RARE, thereby combining both the advantages and disadvantages of these methods.

GRASE creates an echo train by alternating between RF and gradient refocusing. Figure 1.13 shows a typical GRASE pulse sequence. Following an initial excitation, a train of spin echoes is obtained by RF refocusing pulses, like in RARE. In addition, between consecutive RF refocusing pulses a short echo train is obtained by an alternating read gradient, like in EPI. Similarly to RARE, a rewinder phase-encoding gradient is used at the end of each RF refocusing interval to ensure that the coherences remain unchanged between RF pulses. The signal decay along the GRASE echo train is determined by a combination of T_2 and T_2^* effects.

Compared to EPI, GRASE has similar advantages to RARE. GRASE is less sensitive to off-resonance effects due to the shorter gradient echo train used between consecutive RF refocusing pulses. This leads to a shorter evolution of phase errors and therefore better image quality than EPI, particularly in regions where EPI images will show strong artifacts and signal loss due to strong field inhomogeneities [47]. Another advantage is that in GRASE the signal decay along the echo train is dominated by T_2 , therefore longer echo trains are possible in single shot imaging, potentially leading to higher spatial resolution. The requirement of fast switching gradients is not as strict a requirement as for EPI. The disadvantages of GRASE compared to EPI are that GRASE is slower (due to the use of RF refocusing) and GRASE produces more

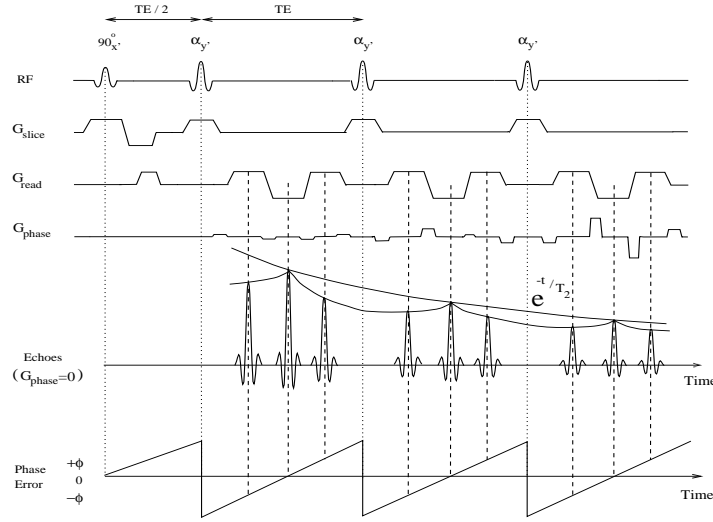


Figure 1.13: GRASE sequence with three gradient echoes per RF refocusing interval. See text for details.

RF power deposition per image, thus imposing a limit on the number of images that can be acquired per unit time.

Compared to RARE, GRASE has the advantage that for the same amount of RF power deposition it generates a greater number of echoes in single shot imaging, leading to an improved spatial resolution. Alternatively, for the same spatial resolution less RF power is required allowing a higher image acquisition rate or for higher SNR per image. In both RARE and GRASE sequences refocusing angles with less than 180° can be used to reduce the power deposition and increase imaging speed at the cost of reduced SNR. A disadvantage of GRASE relative to RARE is that GRASE is slightly more sensitive to phase errors because not only pure spin-echoes are used. GRASE also uses an alternating read gradient and is therefore more sensitive to hardware imperfections.

A special consideration with GRASE imaging arises from the quasi periodic modulation of both the phase errors and the signal amplitude along the echo train (Fig. 1.13). In EPI or RARE sequences the signal amplitude follows a monotonically decreasing decay whereas the phase errors increase linearly (EPI) or do not evolve at all (RARE). In GRASE the situation is different and if the phase and amplitude modulations are not taken into account, then severe image artifacts can appear in the phase encode direction [48, 49]. It follows that for GRASE the choice of the k -space trajectory followed during data acquisition is particularly important for defining the final image quality. The origin of image artifacts from the amplitude and phase modulations, as well as methods for reducing these artifacts will be discussed in more detail in Chapter 2 using the concept of the point spread function.

1.4 Functional MRI of the human brain

Understanding human brain function remains a challenge and a considerable amount of energy has been devoted in the development of new brain imaging techniques for this purpose. The latest of these imaging methods have been those that use MRI. These MRI-based techniques have been collectively termed *functional* MRI or fMRI. This section gives a very brief overview of fMRI. Comprehensive reviews on the basic concepts and applications of fMRI have been recently reported [50, 41]

Brain activation

When a population of neurons experiences membrane polarity changes during activation, measurable electrical, magnetic and metabolic changes are created [51, 52]. These changes are accompanied, through mechanisms that are not yet completely understood [53, 54], by changes in blood flow [51, 55], blood volume [56, 57] and blood oxygenation [58, 59, 60]. All techniques for assessing human brain function are based on the detection and measurement of these electrical, magnetic, metabolic and hemodynamic changes that are spatially and temporally associated with neuronal activation. Alternative modalities to fMRI for mapping these responses in the brain include positron emission tomography [61, 62], single photon emission computed tomography [63], electroencephalography [64, 65, 66], magnetoencephalography [67, 68] and optical imaging [69, 70, 71]. The advantages and disadvantages of each of these human brain mapping modalities have been discussed in the literature [66, 72].

MRI of cerebrovascular physiology

MRI can be used to map several types of cerebrovascular information by using paramagnetic exogenous contrast agents or blood as an endogenous marker. The information that can be obtained includes maps of cerebral blood volume and flow as well as maps of *changes* in cerebral blood volume, flow and oxygenation.

Initial fMRI experiments used low toxicity intravascular paramagnetic contrast agents to assess blood volume changes [73, 56]. A bolus of paramagnetic contrast agent is injected and T_2^* -weighted images are obtained. As the contrast agent passes through the vasculature, magnetic field gradients are transiently produced. These gradients cause intravoxel dephasing, resulting in a signal attenuation that is linearly proportional to the concentration of the contrast agent, which in turn is a function of blood volume [74]. This technique has proven to be very robust but it has important limitations. Although the toxicity of the tracers used is low, the dose of contrast agents is sufficiently high that repeat studies can not be made consecutively. In addition, the time resolution of the method is of the order of 30 s due to the time it takes for the bolus of contrast agent to build up and wash out.

These problems were circumvented by using endogenous blood as a freely diffusible marker for assessing blood flow [75] and/or blood oxygenation [58, 59, 76]. From these endogenous techniques, the one that has demonstrated the highest activation-induced signal change contrast has been the measurement of oxygenation changes.

Blood oxygenation level dependent (BOLD) contrast

Oxygenation changes in blood are associated with magnetic susceptibility changes. In 1932 Pauling et al. [77] discovered that the magnetic susceptibility of red blood cells decreases

linearly from full oxygenation to full deoxygenation. This susceptibility difference results from the fact that oxyhemoglobin contains diamagnetic oxygen-bound iron and deoxyhemoglobin contains paramagnetic iron [77].

In 1990 it was demonstrated that the MR signal in the vicinity of vessels and in perfused human brain tissue decreases with a decrease in blood oxygenation [58, 59, 76]. This type of physiological contrast was termed blood oxygenation level dependent (BOLD) contrast. The first papers demonstrating the use of BOLD contrast for the observation of human brain activation were reported in 1992 [78, 75, 79]. In these experiments a small but significant local signal increase in activated cortical regions was observed using susceptibility-weighted (i.e., T_2^* -weighted), gradient-echo pulse sequences.

The model to explain these observations is that the increase in blood flow originating from neuronal activity increase results in an excess of oxygenated hemoglobin beyond the metabolic need. Thus, there is a reduction of the proportion of paramagnetic deoxyhemoglobin in the vasculature. This causes a reduction in susceptibility differences in the vicinity of venules, veins, and red blood cells within veins, thereby causing less loss of spin coherence (increase in T_2 and T_2^*) and therefore an increase in the signal in T_2 and/or T_2^* -weighted MRI sequences.

Sequence requirements for fMRI

MRI sequences used for fMRI must fulfill certain basic requirements. These requirements will be briefly discussed.

The most fundamental of needs in fMRI is a high functional contrast-to-noise ratio (CNR) to detect small signal changes. Functional contrast relates to the detection of activation-induced signal changes in space and time. When using gradient-echo sequences, maximal susceptibility contrast is achieved by using a T_2^* -weighting approximately equal to the T_2^* of the activated tissue [80, 81]. In addition, both computer simulation [74, 82] and experimental studies [83, 84] indicate that the BOLD contrast increases with the strength of the main magnetic field.

In conventional multi-shot techniques pulsatile motion (which has a frequency of approximately 1 Hz) during data acquisition has been shown to cause variation in k -space registration which primarily causes nonrepeatable ghosting variations across each image, adding significantly to the noise [85]. Thus, single-shot imaging sequences which are able to sample all k -space in less than a second will "freeze" physiological motion and hence reduce this source of noise significantly. Such fast imaging techniques will also reduce the total study time thereby minimising artifactual signal changes that may occur due to involuntary head motion during the experiment.

It is important that the functional images are minimally distorted. If image distortions are severe, then misregistration between the functional map and the high spatial resolution anatomical image over which the map is normally overlaid may lead to incorrect determination of the activation site. In addition, image distortions, which are usually subject dependent, may reduce the effective functional sensitivity when results are averaged across subjects.

It is becoming increasingly desirable for most functional imaging studies to observe the entire brain. When imaging at high main fields this imposes restrictions regarding the maximum RF power deposited by the imaging sequence.

1.5 Aims of this work

In view of the requirements for imaging sequences employed in fMRI, EPI has become the predominant technique for the development and applications of fMRI, and if possible, in combination with high field MRI systems [50, 41]. The advantages of EPI for fMRI include high temporal resolution and low RF power deposition.

EPI is, however, of limited use in areas of the brain with short T_2^* (*c.f.* section 1.3.1) which are often important for cognitive studies. The use of RARE could avoid this sensitivity to field inhomogeneities but at the cost of a lower image acquisition rate (*c.f.* section 1.3.2). Therefore, a natural choice for investigating fMRI in these brain areas is to consider a method like GRASE (*c.f.* section 1.3.3), which is a hybrid of EPI and RARE.

At the time when the work of this thesis begun, several papers had been published [46, 47, 86, 87, 88] describing the implementation and use of GRASE at 1.5 Tesla. Most of these papers were focused in investigating phase-encoding methods for minimizing the artifacts in the phase-encode direction of GRASE images. One of these publications proposed the use of GRASE for fMRI [47] but there was no demonstration for this application.

In this context, the aims of this thesis were:

- i)* Implementation of the GRASE sequence on a whole-body 3 Tesla system with the phase-encoding methods proposed in the literature.
- ii)* Investigation of the attainable image quality and consideration of alternative phase-encoding methods.
- iii)* Investigation of the BOLD contrast capabilities of GRASE for fMRI. This investigation should consider both the intrinsic contrast of GRASE given by the use of spin- and gradient echoes as well as other methods for increasing the BOLD contrast.
- iv)* Comparison of the results of fMRI experiments given by GRASE and EPI. Determination of the indications for using GRASE.

Chapter 2

GRASE imaging

The basic principles of GRASE imaging have been introduced in the previous chapter, where the origins of the amplitude and phase modulations of the signal along the echo train were described. These amplitude and phase modulations (AM and PM respectively) can cause strong image artifacts in the phase-encode direction if not properly considered. This chapter describes how these artifacts originate and discusses methods for reducing them.

The first two sections describe the importance of the phase-encoding method and of phase correction in GRASE imaging. The third section reviews some of the phase-encoding schemes proposed for GRASE in the literature. The fourth section proposes a new method for ordering the phase-encoding gradient. The last section examines this new method with those of the literature by comparing their point spread functions.

2.1 Importance of the phase-encoding method

In a single shot experiment like EPI, RARE or GRASE a total of N_y separately phase-encoded echoes are acquired in an echo train to sample N_y k -space coordinates in the phase-encoding direction (k_y). A phase-encoding scheme defines which echo along the echo train is used to sample each k_y coordinate.

In principle, any mapping scheme could be used so that $N_y!$ phase-encoding methods are possible (e.g., of the order of 10^{89} possibilities for an image acquired with 64 phase-encoding steps). All these possibilities are equivalent only in the ideal case when all echoes in a template scan are identical (i.e., when they all have the same amplitude and the same phase in a scan performed without phase-encoding). In such a case, each echo can be equally used to map any k_y coordinate and therefore any mapping scheme gives the same information in k -space. However, if the echoes in a template scan have different amplitudes and phases, then each possible phase-encoding method will map differently these modulations to k -space along the k_y direction. Therefore, as different AM and PM in k -space reflect different image properties, it is important to choose the appropriate phase encoding method.

The signal modulations in k -space determine two important properties in an image: the contrast and the point spread function (PSF). The contrast is defined mostly by the relaxation undergone by the echoes which are mapped to the central part of k -space. In GRASE the AM depend mainly on T_2 , T_2^* so that different image contrasts can be achieved. For example, the lowest image contrast can be obtained if the first echoes of the echo train are used to encode

the center of k -space. Such a phase-encoding method has a short TE_{eff} and gives an image which has a low T_2 contrast. On the contrary, if the later echoes are used (long TE_{eff}) then a higher T_2 contrast can be achieved which will also result in a reduction of the image intensity.

The other important property defined by the AM and PM in k -space is the PSF. The concept of the PSF was introduced in Chapter 1 as a mathematical tool for calculating how the image of a point source deteriorates through the AM and the PM in k -space. The PSF in the phase-encode direction is calculated as the Fourier transform of the AM and PM along k_y . The ideal PSF with a finite sampling time is a sinc function and is obtained only when the phase error is constant and when there is no signal decay. Deviations from the ideal PSF correspond to image deterioration. The PSF in the read direction is normally neglected. This is due to the fact that the acquisition time of each single echo is normally short ($\simeq 1$ ms) compared to the average T_2^* tissue relaxation time ($\simeq 50$ ms), thus giving negligible image artifacts.

Summarising, the choice of the phase-encoding method is important because it has to provide both the PSF giving minimum artifacts and the desired image contrast. A useful strategy, which was followed in the work described in this thesis, is to make image contrast independent of the phase-encoding method, hence allowing their optimization separately. This can be achieved by combining the use of a preparation experiment followed by a short TE_{eff} imaging experiment. In this way, during the preparation experiment the magnetization undergoes the desired relaxation and this magnetization is then immediately used to form the echoes which will sample the center of k -space. The image contrast will be therefore mainly determined by the preparation experiment and the phase-encoding will define the PSF.

So far the discussion about the importance of the phase-encoding method has been general and valid for any single shot imaging method like EPI, RARE or GRASE. The phase-encoding method is particularly important for GRASE imaging because, due to the periodic nature of the phase errors, it is not possible to minimise at the same time both the AM and the PM in k -space. It should be noted that each echo has an amplitude and a phase error associated with it. This means that a phase-encoding method simultaneously defines both the AM and the PM, i.e., a phase-encoding method cannot treat the AM and the PM independently and hence cannot minimise their modulations separately. Therefore, a compromise has to be reached and for GRASE different phase-encoding methods can be investigated which achieve different degrees of improvement in the PSF by minimising either the AM or the PM in k -space. This will be further discussed in the following sections.

For EPI and RARE the situation is different. In these methods the signal decays monotonically and the phase errors evolve linearly along echo train (for EPI) or do not evolve at all (for RARE). This leads to a situation in which the conventional linear phase-encoding method will give an optimal (smooth) amplitude and phase modulations at once. For these imaging methods the resulting PSF will still be distorted due to the signal modulations in k -space, but the PSF cannot be further optimised by varying the phase-encoding scheme.

2.2 Reduction of phase errors

Given the phase errors, the phase-encoding scheme aims at minimizing their modulation in k -space. However, it is of interest to consider methods for reducing the magnitude of the phase errors in the first place. If these can be reduced then the PM would also be automatically

reduced and therefore the phase-encoding method could be more focused at improving the AM.

The normal procedures for reducing the magnitude of the phase errors include the following:

- a) Fat suppression: the signal from fat protons is off resonance with respect to that of water protons (*c.f.* Chapter 1). It is therefore important to suppress the fat signal in order to avoid its contribution to the phase errors. One method for performing fat suppression consists in starting the experiment with a frequency-selective pulse that excites only the fat protons [89]. This signal is then dephased by application of a spoiler gradient, which is followed by the conventional GRASE sequence.

- b) Phase correction: instrumental imperfections and field inhomogeneities introduce phase and time shifts between the odd and even echo signals during the GRASE readout between two consecutive RF refocusing pulses. These imperfections, which are created mainly because odd and even echoes are sampled in opposite directions in k -space, must be corrected prior to image reconstruction to eliminate ghosting artifacts. A perfect phase correction is not always possible and phase correction methods usually perform average corrections. The usual approach for correction is based on acquisition of reference data obtained without phase-encoding [46]. The phase and time shifts between odd and even echoes are calculated from the reference data and used to correct the image data. The phase correction method used in this work will be described in Chapter 3, where the image reconstruction algorithm is discussed.

These procedures for reducing phase errors are used for GRASE imaging independently of the phase-encoding method used.

2.3 Review of short TE_{eff} phase encoding methods

This section reviews two of the most basic short TE_{eff} phase-encoding methods proposed for 2D GRASE imaging: centric GRASE and centric k -space banded GRASE [48]. The term 'centric' is used to emphasize that high intensity signals are mapped to the central region of k -space therefore achieving a short TE_{eff} . The calculation and discussion of the PSFs resulting from these methods will be postponed to a later section where these and other phase-encoding methods will be evaluated. A comprehensive comparison of short TE_{eff} phase-encoding schemes has previously been reported [49].

The conventional centric (or center-out) phase-encoding method is also described at the end of this section. This short TE_{eff} phase-encoding scheme, although used in single shot sequences like RARE [90], has not been considered by others for GRASE.

2.3.1 Centric GRASE

This phase-encoding method achieves the minimum PM in k -space at the cost of introducing strong AM in the phase-encode direction [49]. The main idea is to group signals in k -space with identical phase errors. For example, if $N_g=3$ gradient echoes per refocusing pulse are used, then k -space will be divided in three regions. Each one of these regions will be given echoes associated with only one of the three phase errors. In addition, within each region the echoes are distributed so that they fill the region from its center outwards, in an alternating way. By doing this some of the high intensity echoes are placed in the center of k -space and therefore a

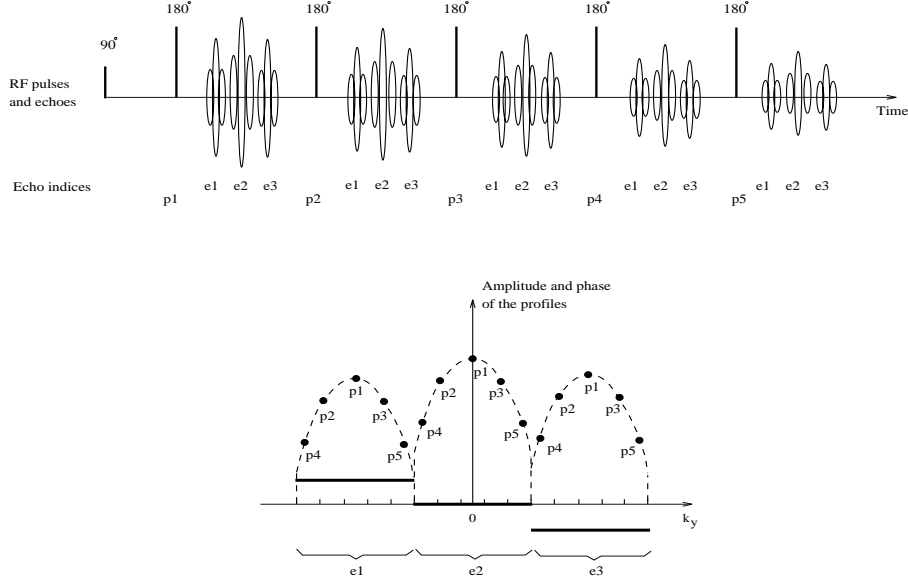


Figure 2.1: Centric GRASE phase-encoding scheme for $N_g=3$ and $N_p=5$.

short TE_{eff} is achieved. The TE_{eff} corresponds typically to the time when the first Hahn echo occurs.

Figure 2.1 shows schematically how the centric GRASE phase-encoding method maps the signal decay and the phase errors to the phase-encode direction of k -space. In this example the GRASE sequence consists of $N_p = 5$ RF refocusing pulses with $N_g = 3$ gradient echoes per RF interval. The position of each echo along the echo train can be uniquely defined by a pair of indices, one defining the gradient echo in a RF interval ($e_{(i_g)}$, with $i_g = 1, \dots, N_g$) and the other defining the RF interval ($p_{(i_p)}$, with $i_p = 1, \dots, N_p$). Figure 2.1 shows how these indices are mapped to the k_y direction generating the typical AM (dashed line) and PM (thick solid line) for the centric GRASE phase-encoding method.

2.3.2 k -space banded centric GRASE

In this method the GRASE echo train is divided in a number of parts, typically three or five, so that each time segment covers a region in k -space by using the centric GRASE ordering [88, 49].

Figure 2.2 shows schematically the AM and PM resulting from the k -banded (kb) centric GRASE method. An odd number of bands is generally used so that one can band symmetrically covers the central part of k -space while the other bands cover the sides. In this example three bands have been used, each corresponding to a different time segment of the echo train. The first segment of the echo train is used to map the center of k -space thus giving a short TE_{eff} . Note that the PM within each band has been chosen to be continuous with the PM of the

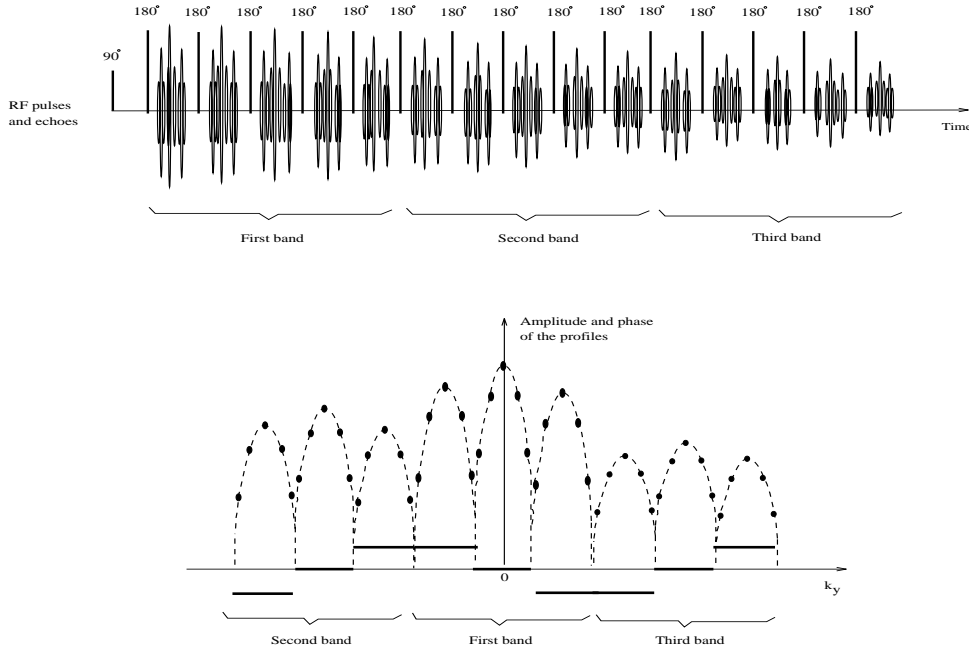


Figure 2.2: Kb centric GRASE phase-encoding scheme for $N_g=3$, $N_p=15$ and three bands.

adjacent band in order to minimize the overall PM. The kb centric GRASE method has the same TE_{eff} as the centric GRASE method. The difference is that in kb centric GRASE the size of the AM is reduced at the cost of increasing the frequency of both the AM and the PM.

2.3.3 Conventional centric scheme for GRASE

In the conventional centric method, if δk_y is the minimum distance between k_y coordinates, then the echoes in the echo train sequentially sample the coordinates $k_y = 0, \delta k_y, -\delta k_y, 2\delta k_y, -2\delta k_y, \dots$ and so forth.

The resulting AM and PM are schematically shown in Figure 2.3. The assumed GRASE sequence is the same as that shown in 2.1 and only the modulations of the amplitude (dashed line) and phase (solid line) in k -space are shown.

2.4 A novel Template Interactive Phase Encoding method

When GRASE was proposed as an imaging method it was quickly realized that the PM in k -space were responsible of image artifacts if conventional phase-encoding methods were used. Therefore, since then all the phase-encoding methods proposed for GRASE have been based on predefined k -space trajectories which focus mainly at minimising the PM along the phase-encode direction. As a result, these methods introduce strong AM which can still give artifacts.

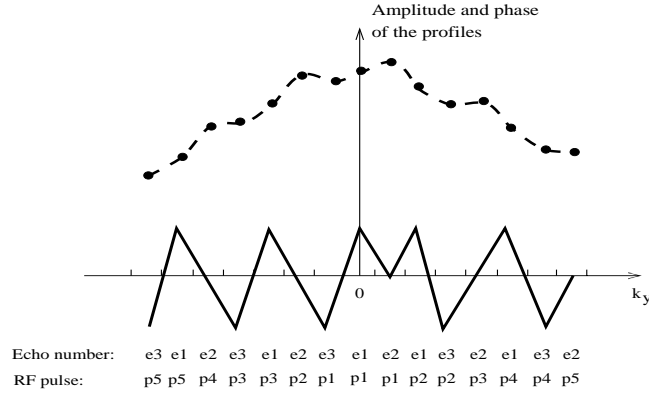


Figure 2.3: Conventional centric phase-encoding scheme. Amplitude (dashed line) and phase (solid line) modulations in k -space for a GRASE sequence having $N_g=3$, $N_p=5$ (Fig. 2.1).

Here a new phase-encoding method is presented which aims at minimizing the AM and leaves the PM to be corrected by the usual phase correction which is used during reconstruction of GRASE images. In principle, with the proposed method, any desired AM can be obtained by previously measuring the signal decay of a template scan. We call this method Template Interactive Phase-Encoding or TIPE [91]. Previous reports describe the use of a template scan to correct for time position errors, phase errors and T_2 and T_2^* decay [46]. We proposed that the template scan can also be used to generate the phase-encoding scheme. The new concept is therefore that the phase-encoding scheme, rather than being a predefined k -space trajectory, is interactively calculated from the signal from the object to be imaged. The TIPE method can be particularly useful in fast MRI methods which allow each echo to be phase-encoded in any arbitrary way, and where the intensity decay of the echoes along the echo train is not known a priori, as in the case of GRASE.

The TIPE method can be applied for short TE_{eff} GRASE imaging (centric TIPE). In this application the signal decay of a template scan is used to order the echoes in k -space so that the higher the intensity of an echo the lower the absolute value of spatial frequency encoded by the echo. This phase-encoding scheme gives an amplitude modulation in the phase-encode direction that is maximum at the center, is symmetric around the center and decreases monotonically from the center of k -space. Such a phase-encoding scheme significantly reduces the amplitude modulation artifacts in the phase encode direction and gives high signal-to-noise-ratio (SNR) images due to the short TE_{eff} .

The centric TIPE method minimizes the AM without considering the resulting PM. The centric GRASE method, on the other hand, minimizes the PM and results in strong AM. The kb centric method improves the AM at the cost of a worse PM. The advantages and disadvantages of these phase-encoding methods will be discussed in the following section.

2.5 Evaluation of phase-encoding methods: comparison of PSFs

In this section the centric TIPE method is evaluated by comparing its resulting PSF with those given by the centric GRASE, kb centric GRASE and conventional centric phase-encoding methods.

To calculate the PSF of the different methods we simulated the amplitude signal decay with the off-resonance phase errors. We then calculated the Fourier transform of the resulting AM and PM given by each phase-encoding method.

To model the signal we considered that the magnitude decay results from a combination of T_2 and T_2^* effects and that the phase of the signal is modulated by the resonance offset ($\Delta\nu = 1/(\pi T_2^*)$) of the frequency distribution center (due primarily to static field inhomogeneities). It was assumed that the fat signal was suppressed and no other preparation experiment was considered. For analytical convenience we made the assumption that the tissue transverse relaxation rate $R_2^* = 1/T_2^*$ can be separated into two components, one that describes the reversible dephasing of the magnetization (R_2') and another that accounts for the irreversible dephasing ($R_2 = 1/T_2$) so that $R_2^* = R_2' + R_2$. With these assumptions the GRASE signal between the i_p -th and the (i_p+1) -th RF refocusing pulse can be written as the product of two exponentials, one describing the amplitude modulation and the other describing the phase modulation:

$$S_{(t,i_p)} = \exp(-R_2 t - R_2' |t - i_p TE|) \exp(-i 2\pi \Delta\nu (t - i_p TE)) \quad (2.1)$$

where TE is the echo time and t is the time from the initial 90° pulse. The time t takes values in the interval $[(2i_p - 1)TE/2, (2i_p + 1)TE/2]$. We assumed unity gain and initial amplitude. We also assumed that the RF refocusing pulses were perfect, adding no T_1 contribution to the signal decay.

The AM and PM described by equation 2.1 can be compared with those schematically shown in Fig. 1.13. At the times where the spin-echoes (Hahn echoes) occur ($t = i_p TE$) the magnetization is fully refocused giving a pure exponential T_2 decay with, ideally, no phase errors. The gradient echoes, which are symmetrically placed around each spin-echo, have phase errors of opposite sign due to the net frequency offset $\Delta\nu$ from the resonance frequency. The gradient echoes have different intensities because, although they have undergone the same amount of R_2' relaxation, they occur at different times from the initial excitation and therefore have different R_2 weighting.

The main interest of our simulation was to compare the effects of different short TE_{eff} GRASE phase-encoding methods when imaging the head, particularly when considering cortical regions because in these regions the highest signal and the least artifacts are desired for fMRI experiments. Cortical regions can include areas with high (short T_2^*) and/or low (long T_2^*) susceptibility-induced field inhomogeneities, depending the area of the brain being considered. It is expected that these different relaxation conditions will reflect different behaviours in the PSF so that the two cases were considered separately.

The following relaxation parameters were used for the simulation: $T_2 = 80$ ms, $T_2^* = 8$ ms (high field inhomogeneity region, $\Delta\nu = 40$ Hz) and $T_2^* = 32$ ms (low field inhomogeneity region, $\Delta\nu = 10$ Hz) [92]. The timing parameters were chosen to approximate those pertaining

to our MRI system (see Appendix A). The echo time was 11 ms and the inter-echo time 2.5 ms, giving phase shifts of 0.2π and 0.05π radians for $T_2^* = 8$ ms and $T_2^* = 32$ ms respectively.

Only single shot images were considered in the simulations. For each phase-encoding scheme the case of $N_p = 33$ RF refocusing pulses and $N_g = 3$ gradient echoes per RF refocusing was simulated, giving a total of 99 phase-encoding steps. A relatively large N_p was chosen in order to study the effect of strong signal decay along the k_y direction. With this choice of N_p the time interval between the first and last echoes is approximately $4.5T_2$ which means that by the end of the echo train the simulated signal is only 1 % of the starting signal. To increase the details in the shapes of the PSFs, data sets were zero-filled to 512 points before Fourier transformation [93].

Figure 2.4 shows the computer simulation results for the case of short T_2^* . Each row corresponds to one of the phase-encoding scheme considered: centric kb GRASE, centric GRASE, conventional centric, and centric TIPE schemes. The left hand side column shows the magnitude (solid line) and phase (dashed line) of the simulated signal decays for each phase-encoding scheme. The decays are displayed versus the phase-encoding step numbers. The scale shown corresponds to the amplitude and it is unity for no attenuation. The phase, shown on an arbitrary scale for better visibility, corresponds to a frequency offset of 0.2π radians per gradient echo. The central column displays the magnitude of the PSFs resulting from the left column. The right hand column shows the magnitude of the PSFs resulting from the case when the frequency offset is zero. The magnitude of the PSFs are displayed in arbitrary units versus the fraction of the field of view (FOV), which takes values between -0.5 and 0.5.

In practice the raw data is usually phase corrected prior to reconstruction of GRASE images [46]. In the right hand column of Fig. 2.4 the offset of the resonance frequency was set to zero to simulate the PSF resulting from a perfect phase correction. This is, however, an idealization as phase correction methods normally perform only average corrections. The sidelobes in the PSFs in this column are thus only due to the amplitude modulation of the signal decay in k -space. The results for the centric kb GRASE and centric GRASE phase-encoding schemes have already been discussed in the literature [48, 49] and are showed here only for comparison purposes. In Fig. 2.4 it can be seen that in these methods the ideal phase-correction does not appreciably reduce the side lobes in the PSFs. This means that for these methods the sidelobes in the PSFs are mainly due to the signal amplitude modulation in k -space.

Figure 2.4 shows that for the short T_2^* used in the simulation the conventional centric phase-encoding scheme gives rise to a modulation of high frequencies on both the phase and the amplitude of the signal in k -space. The AM occurs at a single frequency and gives rise to rather sharp side lobes in the PSF. The PM occurs at a narrow frequency range that exclude the amplitude modulation frequency. As a result the PSF has broad side lobes which are far from the central peak. These side lobes correspond to a low intensity low frequency artifact in the phase-encode direction of the reconstructed image. Even a perfect phase correction (zero offset) will not eliminate these artifacts because the amplitude modulation will remain (right hand column in Fig.2.4) This will give a single frequency well structured artifact in the phase-encode direction.

By definition the centric TIPE method gives a smooth, centered amplitude variation of the signal in k -space at the cost of a strong PM. The PSF of the centric TIPE method shows side lobes originating from phase errors. However, after an ideal phase correction the resulting PSF will have no side lobes. For longer T_2^* values it can be seen (data not shown) that the results

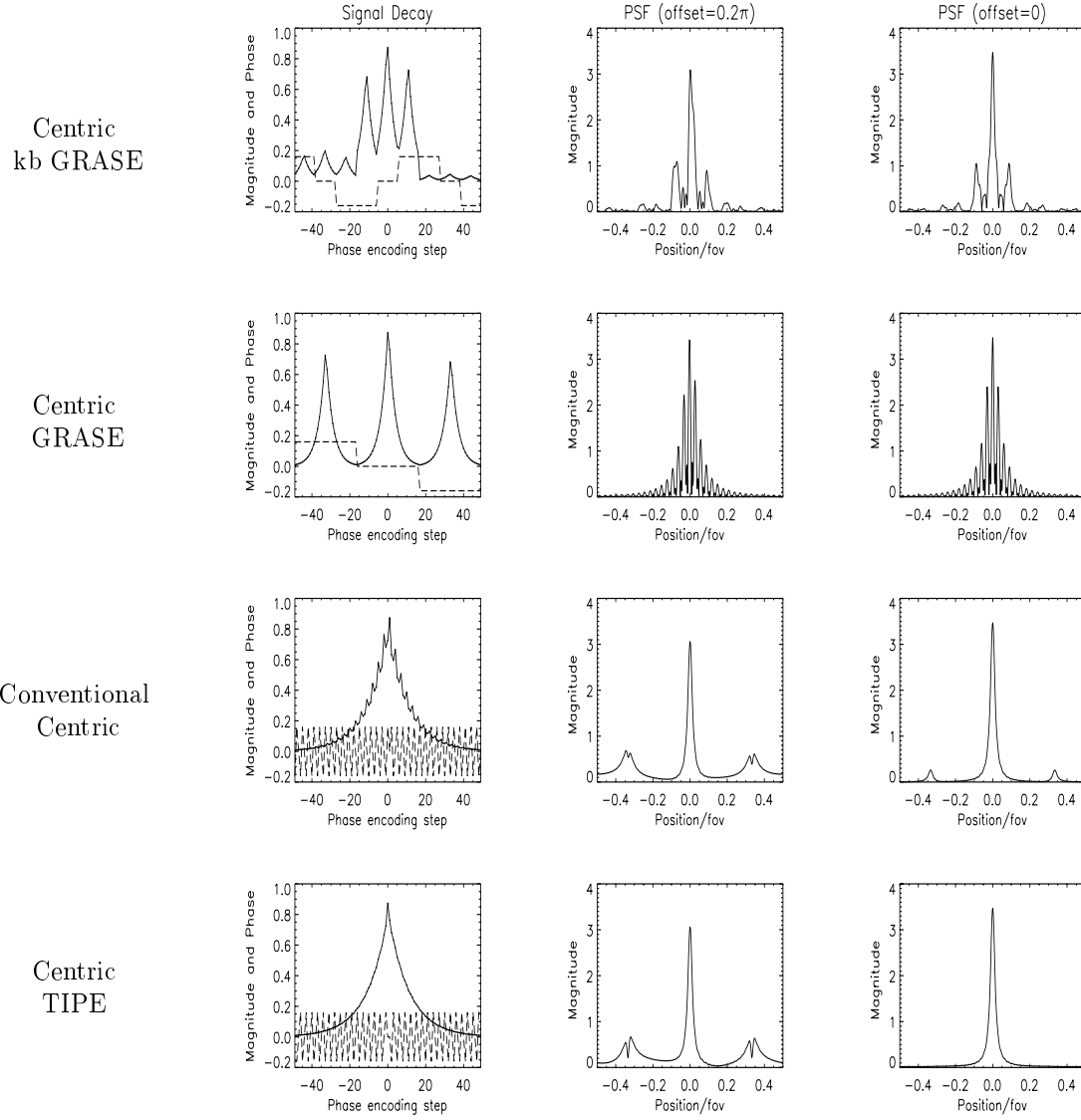


Figure 2.4: Simulated signals and the corresponding PSFs for the centric kb GRASE, centric GRASE, conventional centric and centric TIPE schemes for $N_p = 33$ and $N_g = 3$. See text for more details.

for centric kb GRASE, centric GRASE and centric TIPE do not qualitatively differ from those shown in Fig. 2.4). However, the results from the conventional centric method become the same as those given by centric TIPE in Fig. 2.4. In other words, as T_2^* tends to T_2 the conventional centric method gives, similarly to the centric TIPE method, a smooth amplitude modulation of the signal in phase encode direction.

The computer simulation results in Fig. 2.4 suggest that a reduction of artifacts in the phase corrected images may be obtained by optimising the modulation of the magnitude decay only (without restrictions on the phase modulation) which is what the centric TIPE GRASE method does. This is based on the assumption that a good phase correction can be achieved. When T_2^* is long (i.e., where susceptibility-induced field inhomogeneities are not so severe) then both centric TIPE and conventional centric methods give similar results. If T_2^* is short (larger phase errors have to be corrected) then centric TIPE gives less artifacts than the other methods considered.

There are several parameters that can be varied in the simulation. In Fig. 2.4 only the effects of changing the phase error are shown. The effects of increasing the number of gradient echoes N_g (i.e., increasing data collection efficiency) and varying T_2 have already been discussed in the literature for the kb centric GRASE and centric GRASE methods [48]. It was found that if N_g is increased the PSF of the centric TIPE GRASE method stays essentially as that shown in Fig. 2.4 (right hand column). However, for the other phase-encoding methods considered the artifacts in the PSFs become more severe as result of increased AM. As before, for larger N_g the results from the conventional centric method tend to those of the centric TIPE method as T_2^* tends to T_2 . This suggests that for larger N_g the centric TIPE GRASE method will produce significantly less amplitude related artifacts in the phase corrected images when imaging regions of high susceptibility-induced field inhomogeneities. The source of improvement is a smooth amplitude modulation. Once again, this is assuming that a good phase correction can be achieved, which for larger N_g will become more important as phase errors increase.

As T_2 decreases, the PSF of the centric TIPE GRASE method becomes broader and therefore the spatial resolution (i.e., the width of the PSF) will become lower. However, for the kb centric GRASE and centric GRASE methods discontinuities in the magnitude decay will become more abrupt for short T_2 s. The effect is that, for these methods, the height of the side lobes in the PSF increase relative to the central peak, suggesting that artifacts will also increase.

In summary, the results suggest that, of the short TE_{eff} phase-encoding methods considered here, the centric TIPE method should give the lowest artifact levels in the phase corrected images, particularly where T_2^* is short. The reason for the predicted improvement is that TIPE produces a smooth amplitude modulation. However, whether it is apparent in practice will depend on the effectiveness of the phase correction. When imaging regions having low magnetic field inhomogeneities the centric TIPE and the conventional centric phase-encoding schemes should give similar results.

Chapter 3

Implementation of GRASE imaging at 3 Tesla

In the previous chapter the template interactive phase-encoding scheme (TIPE) was presented and a computer simulation was described to compare TIPE with other short effective TE phase-encoding schemes previously proposed for GRASE imaging. The phase-encoding schemes considered in the simulation were centric GRASE, kb centric GRASE, conventional centric ordering and centric TIPE. This chapter shows the results of implementing and comparing these methods on a 3 Tesla MRI system.

The implementation required writing both the programs that control the MRI system for the data acquisition as well as the programs that reconstruct the images from the measured raw (i.e., unprocessed) data. Phantom and human head images were obtained to test the programs during the implementation stage and to test the predictions drawn from the computer simulation study. The materials used (MRI system and samples) are separately described in Appendix A.

3.1 Imaging sequence

A general GRASE sequence using $N_g=3$ gradient echoes per RF refocusing has been shown in Fig. 1.13. In Figure 3.1 the sequence is shown in some more detail and in the form as it was implemented in the MEDSPEC system when no preparation experiment was used. The instructions in the sequence between consecutive RF refocusing pulses are repetitive and are therefore programmed as a loop. This loop is repeated N_p times to give a total of $3 N_p$ echoes after a single excitation. In each loop the phase-encoding gradients take different values depending on the phase-encoding scheme used. Gradient switching points that are simultaneous for several gradients are indicated by vertical dotted lines.

To maximise the efficiency of data collection, the sequence was programmed so as to have an echo time TE as short as possibly allowed by our hardware (see Appendix A). The calculation of the read, slice and phase-encoding gradient strengths is standard in MRI and has been described in Chapter 1. In the design of the pulse sequence the following additional relations were considered:

a) Delays in the sequence were calculated so as to keep $TE/2$ as short as possible.

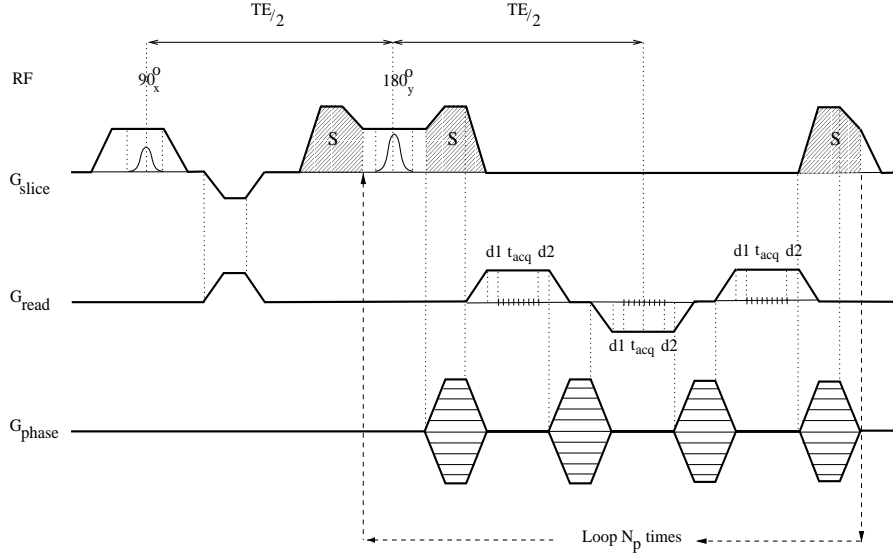


Figure 3.1: GRASE sequence. See text for more details.

b) The RF pulse durations were as short as possible while still giving a nominal 180° pulse and an average power deposition rate under 1 W/kg. The RF supervisor unit of the MRI system automatically interrupts an experiment if the mean transmitted power exceeds this threshold. Gauss-shaped RF pulses with a duration of 2 ms were used for excitation and RF refocusing. The phase of the RF pulses was set to satisfy the CPMG condition (i.e., 90_x° and 180_y°) in order to ensure constructive interference of all coherence pathways originated from the imperfect pulses.

c) The slice gradient spoilers around the RF refocusing pulses (shaded areas *S* in Fig. 3.1) were symmetric, as short as possible and strong enough to prevent any significant FID signal from the RF refocusing from being detected. The efficiency of the spoilers can be tested by running the sequence with the excitation pulse turned off and only the RF refocusing pulses turned on. In this way, any signal detected arises from imperfect RF pulses and can be reduced by increasing the strength of the spoiling.

d) The delays d_1 and d_2 ($\simeq 100 \mu\text{s}$) around each acquisition period t_{acq} (c.f. Fig. 3.1) were calculated so that the echoes are refocused at the centre of each acquisition window. This calculation is done by assuming that the dephasing is solely produced by the read gradient and assuming some gradient shape (trapezoidal in our case). Normally, however, due to hardware imperfections and field inhomogeneities the maximum echo signal will not occur exactly at the centre of the acquisition window, odd and even echoes will show opposite displacements relative to the centre. The delays d_1 and d_2 can be used to correct for this by slightly modifying their values while keeping $d_1 + d_2 = \text{constant}$ to ensure that the total dephasing is constant. The echoes will shift in the direction of the delay which is reduced. This calibration was performed only once, for a phantom, and it was found that during in-vivo imaging the echoes also appeared

centred or very close to the centre. Remaining small time errors were corrected during the image reconstruction process described in the next section.

e) Linear sampling of the NMR signal was performed when the read gradient was constant. A more efficient data acquisition strategy consists of sampling the NMR signal during the gradient ramp times [41]. Echoes were linearly sampled (uniform time-domain sampling) typically with 128 complex data points in 1.28 ms (100 kHz receiver bandwidth).

f) For the TIPE experiment a template scan was first acquired, which was then processed off-line using the IDL language (Research Systems, Inc., Colorado). The raw data echoes were Fourier transformed and for each echo the maximum of the magnitude of the profile was calculated. These maximum values were then ordered in k -space to obtain a centre-out phase-encoding scheme. In this way each echo was assigned a phase-encoding step number which allowed the calculation of a table with the phase-encoding gradient strengths used for the image scan.

It was found that in general, due to stimulated echoes, the first three echoes in the echo train had much lower intensities than the subsequent echoes. Excluding the TIPE order, for the other phase-encoding scheme this would result in an additional modulation of the signal in the phase-encode direction. To avoid this extra modulation these first three echoes were discarded. The effective echo time TE_{eff} was therefore $TE_{eff} = 2TE = 23$ ms for all phase-encoding schemes

A frequency-selective saturation Gauss pulse was used for fat suppression in the head images. The Gauss pulse was 10 ms long (resulting in an excitation bandwidth of approximately 160 Hz), and its resonance frequency was shifted 440 Hz (3.5 ppm at 3 T) with respect to the resonance frequency of water protons. At the start of each imaging experiment global shimming was performed with the linear gradients using the manufacturer's standard procedure.

3.2 Image reconstruction algorithm

To obtain the spatial distribution of the magnetization in the sample a two dimensional Fourier transform is required. In Chapter 1 it was shown that when the NMR signal is uniformly sampled in k -space then this operation takes on a particularly simple form (1.34). However, imperfections in the implementation of GRASE will almost inevitably lead to some distortion of the ideal k -space trajectory therefore leading to ghost images and geometrical distortions.

These effects should be reduced by estimating the true k -space sampling locations from the measured data and using these corrected values in the reconstruction process. Such problems are shared by EPI techniques and several correction methods have been proposed in the literature [41].

Correction methods used in MRI reconstruction typically include methods that measure a field inhomogeneity map and calculate from this the real k -space trajectory [94], methods that directly measure the real k -space trajectory [95] and methods that use a reference scan [46]. The measurement of k -space trajectories has proven to be useful for the reconstruction of spiral images, where the real behaviour of the gradients may considerably differ from the expected response [96]. Main field mapping techniques have been successfully used to reduce image distortions in EPI due to field inhomogeneities, particularly when imaging at high main field strengths. GRASE, however, should be less sensitive to field inhomogeneities than EPI because less gradient echoes are collected while the signal undergoes T_2^* relaxation. We adopted

the reference scan method, which is the phase correction method originally proposed for GRASE imaging and also the easiest to implement from those above mentioned. The reconstruction program was written in the IDL language.

Reference scan

A reference scan is measured by switching off the phase-encoding gradient while keeping the timing of the sequence identical. In the ideal case (i.e., perfect hardware conditions, ideal shim and no relaxation effects) a set of identical echoes would be expected. In reality, however, differences are present: the echoes have different amplitudes, different phases and they are refocused at different time points within the acquisition window. The decay of the signal amplitude originates from the tissue T_2 , T_2^* and T_1 relaxation times and has the effect of broadening the PSF. The difference in phases originates from the off resonance signals and means that the k -space trajectory along the phase-encode direction will no longer be purely defined by the phase-encoding scheme as there are other sources giving phase variations. The timing errors can originate from the time delay between the current in the gradient coil and the gradient field caused by eddy current effects [97]. The delayed gradient field causes the magnetization to refocus late, and due to the time reversal, the lines in k -space acquired with the read gradient having opposite polarity are shifted by the same time delay in the opposite direction.

All these errors reflect deviations from the expected k -space trajectory and if not corrected can lead to strong artifacts along the phase-encoding direction.

Corrections deduced from the reference scan

The timing and phase errors can be measured from a reference scan and used to correct the image data. The underlying assumption of this method is that the eddy-currents induced by the phase-encoding blips during the image scan will not significantly change the estimation of the phase and time errors calculated from the reference scan. Another assumption is that the phase and timing errors produced by the switching read gradient are reproducible.

In principle, the correction can be performed by acquiring a few reference echoes instead of a full reference scan. A full reference scan was used because this scan was also used for generating the phase-encoding scheme for the TIPE scheme. For this reason, although it is not important for the other phase-encoding schemes, we always acquired first the reference scan and then the image scan. In addition, for each imaging slice a reference scan is used because different slices will generally be affected by different field inhomogeneities hence having different phase errors.

The correction from a reference scan consists on performing the following steps:

- 1) Calculate the 1D Fourier transform of the reference and image echoes along the read direction.
- 2) Calculate the phases, point by point, of the reference profile.
- 3) Subtract, point by point, the residual phase error in the profiles from the corresponding image profiles.

The reconstruction in total

The complete GRASE reconstruction process is divided into several steps schematically shown in Figure 3.2. The procedure consists of acquiring first a reference scan without phase-encoding and then an image scan using the desired phase-encoding scheme.

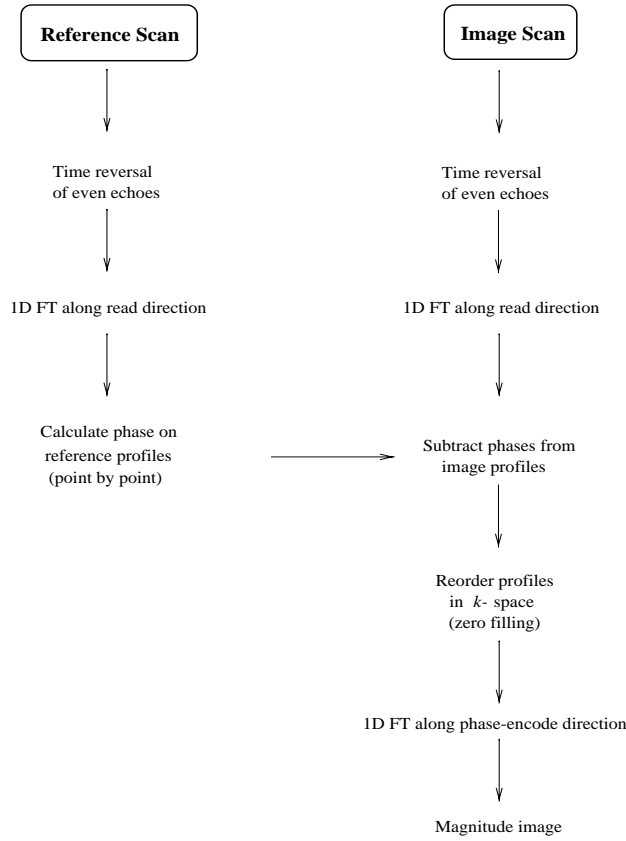


Figure 3.2: Overview of the GRASE reconstruction algorithm. See text for the details.

We follow Fig. 3.2 for the various reconstruction steps. The initial processing step is identical for both scans: the data collected under the negative polarity of the read gradient is reflected (i.e., time reversed) to guarantee the correct order with respect to k -space.

The 1D Fourier transform along the read direction is performed in both scans. The phases in the reference profiles are then subtracted, point by point, from the image profiles. The next step consists in reordering the image profiles along the phase-encode direction of k -space. This is necessary because the sequence of appearance of the image data depends on the phase-encoding scheme used, which will generally not coincide with the order along the k_y -direction. To obtain square image pixels in the final image it is normal to embed the acquired data in a larger square matrix, empty matrix points being filled with zeros. After zero filling the phase-encode direction the 1D Fourier transform along this direction is performed, giving the final image.

3.3 Imaging experiments

Phantom and head images were acquired with different phase-encoding schemes to investigate the quality of GRASE images. Phantom images had two purposes. The first was to debug errors in the pulse sequence and in the image reconstruction program during the implementation stage. The second was to allow the examination of image artifacts resulting from an object having a simple shape and a known constitution. The phantom (Appendix A) consisted of three glass tubes filled with different mixtures of Agarose gel and nickel chloride giving relaxation parameters similar to those expected on a human head at 3 T. The gels had $T_1=1$ s and $T_2=70$, 115 and 190 ms. All images shown in this section were acquired using the whole body gradient set.

3.3.1 Phantom images

Figure 3.3 shows the results obtained from the phantom images. The GRASE sequence consisted of $N_p = 33$ RF refocusing pulses and $N_g = 3$ gradient echoes per RF refocusing pulse. K -space was fully sampled with 99 phase-encoding steps. The phase encode direction is vertical, the FOV is 25×25 cm² and the data matrix was zero-filled to 128×128 . Slice thickness was 5 mm.

Each row corresponds to one of the phase-encoding schemes considered: (i) centric kb GRASE, (ii) centred GRASE, (iii) conventional centric, and (iv) centric TIPE GRASE. Column (a) shows, for each phase-encoding scheme, the measured magnitude decay of the 1-D template profiles (i.e., the magnitude of the 1-D Fourier transform of the template echoes) at the centre of the longest T_2 tube ($T_2 = 190$ ms). The magnitude decay is displayed in arbitrary units versus the phase-encoding step numbers. Column (b) shows the magnitude of the phase corrected GRASE images ($T_2 = 190$, 115 and 70 ms from left to right).

Due to their short effective TE all methods show very little T_2 contrast. For this reason the image scaling was chosen to emphasise artifacts. Column (c) shows a 3D plot of the magnitude images displayed in column (b). For display purposes in columns (b) and (c) the whole FOV is not shown in the read direction. The results in column (c) can be used to compare the intensity of the image artifacts for the different phase-encoding schemes regardless of image windowing. It can be seen that the centric TIPE GRASE and the conventionally centred phase-encoding schemes give similar results. Both schemes produce significantly less image artifacts than the centric kb GRASE and the centric GRASE schemes (edges more sharply defined), particularly for the shortest T_2 tube.

3.3.2 In-vivo images

Figures 3.4 and 3.5 show axial fat suppressed GRASE head images from a normal volunteer for the different phase-encoding schemes considered. Figure 3.4 shows a slice taken far from the sinuses (i.e., where susceptibility-induced distortions are not so severe) and Fig. 3.5 shows a slice taken at the level of the sinuses. The slice thickness was 5 mm and the FOV was 25×25 cm². The phase-encoding direction is left-right. As for the phantom images, k -space was fully sampled with 99 phase-encoding steps following a single excitation and the image was reconstructed to a 128×128 data matrix. The length of the echo train was 374 ms. The intensity

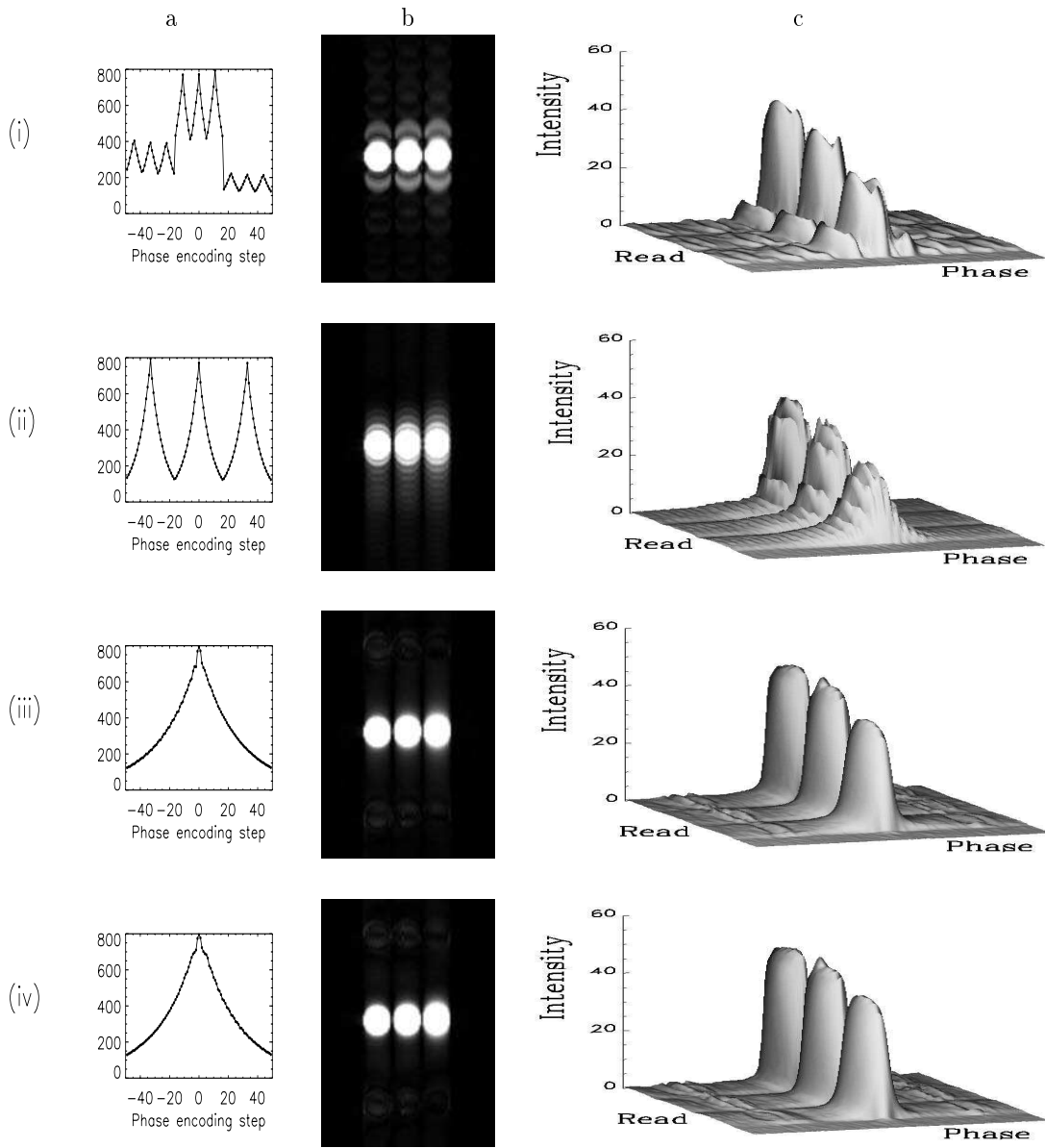


Figure 3.3: Phantom results. Each row corresponds to one of the phase-encoding orders considered: *i)* centric kb GRASE, *ii)* centric GRASE, *iii)* conventional centric and *iv)* centric TIPE GRASE. Column (a) shows the decay of the 1-D template profiles for each phase-encoding order at the centre of the longest T_2 tube. Column (b) shows the resulting magnitude GRASE images. From left to right the phantoms have $T_2 = 190$, 115 and 70 ms respectively. Images were windowed to show artifacts. Column (c) shows a 3D plot of the magnitude images in column (b). In columns (b) and (c) the FOV is not fully shown in the read direction for display reasons.

scaling was chosen to make artifacts visible while trying to maintain the contrast information (inherently low due to the short effective TE of the imaging methods). In each slice the GRASE images have the same scaling.

Figure 3.4 shows that the overall level of artifacts is similar in GRASE images of a region with low main-field inhomogeneities. A closer inspection shows, however, how the different structure of the artifacts associated with each phase-encoding scheme affect different regions of the brain. The kb centric (a) and centric GRASE (b) images have high frequency artifacts in the phase encode direction. These artifacts, although subtle, are visible in the brain contours perpendicular to the phase encode direction at the sides of the brain and result in a reduction in the sharpness of the edge definition. The conventional centric (c) and centric TIPE (d) images show, on the other hand, low frequency artifacts in the phase encode direction. These artifacts interfere with the main image and give rise to regions with signal loss within the brain without substantially affecting the brain edges. The artifacts are more visible in (c) (resulting from amplitude and phase modulations, see arrow) than in (d) (resulting from phase modulation only). The general structure of the artifacts is in agreement with the results predicted by the simulation and those obtained in the phantom experiments.

Figure 3.5 shows a slice having regions with strong susceptibility-induced field distortions (i.e., short T_2^*). It can be seen that the structure of the artifacts for each phase-encoding scheme is similar as in Fig. 3.4: high spatial frequency edge artifacts in (a) and (b), and low spatial frequency artifacts in (c) and (d) leading to some signal loss (see arrows). As expected from the simulation (Fig. 2.4 and the phantom experiments (Fig. 3.3) the artifacts in the kb centric GRASE image (a) are of a more structured nature (i.e., they have a lower spatial frequency) compared to the more diffuse artifacts present in the centric GRASE image (b). In the centric GRASE image the edge artifacts have the effect of producing a dark rim (signal loss) at the border of the brain. The artifacts are more visible in Fig. 3.5 than in Fig. 3.4 due to both the shorter average T_2^* and the poorer phase correction.

Figure 3.5 also shows that, when imaging regions close to the sinuses, the centric TIPE and the conventional centric schemes can have signal loss in areas where the high susceptibility-induced field inhomogeneities are strongest (see arrows behind the eyes in Fig. 3.5c-d). In contrast, even though the kb centric GRASE and centric GRASE images present stronger amplitude related artifacts, they do not lose this information as much as the two former methods do. This may be due to the fact that the kb centric GRASE and centric GRASE schemes have a much lower intrinsic phase modulation. As phase errors become particularly severe close to the sinuses, and since the phase correction method performs only an average correction, it may become important to use a phase-encoding scheme that minimises the phase modulation when imaging such regions. Alternatively, a better phase correction method could be found to take advantage of the improved SNR given by the centric TIPE images. This improvement in the SNR results from the fact that centric TIPE has more signal available at the centre region of k -space than the kb centric GRASE and centric GRASE schemes. An additional advantage of centric TIPE is that the first N_g echoes can be phase encoded without introducing an additional stimulated echo related amplitude modulation. This translates also in an improvement of the SNR, particularly as N_g increases.

It was found that differences between the centric TIPE and conventional centric head images were strongly slice dependent. Sometimes, even in regions of high susceptibility-induced field inhomogeneities both schemes gave similar results. This is a consequence of the fact that the

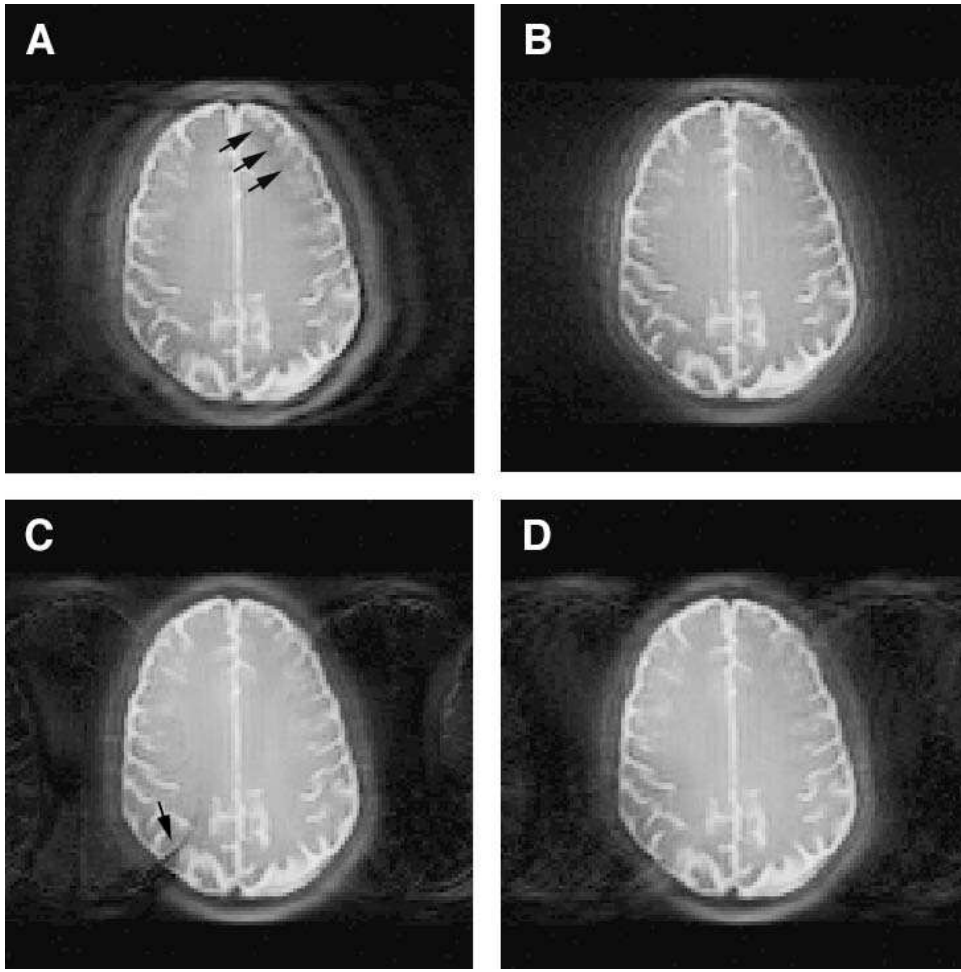


Figure 3.4: Fat suppressed GRASE head images from normal volunteers ($N_p=33$ RF refocusing pulses, $N_g=3$ gradient echoes per RF refocusing pulse, k -space fully sampled after one excitation followed by 99 phase-encoding steps). The image corresponds to an axial slice far from the sinuses obtained using the kb centric GRASE (a), centric GRASE (b), conventional centric (c) and centric TIPE GRASE (d) phase-encoding schemes. The phase-encode direction is vertical, the FOV is 25×25 cm² and the data matrix was zero-filled to 128×128 . Slice thickness was 5 mm. Images are windowed so as to make artifacts visible while keeping the low contrast information (effective TE is 23 ms). The arrow in Fig. 3.4c shows the interference effects of the low frequency artifacts. See text for more details.

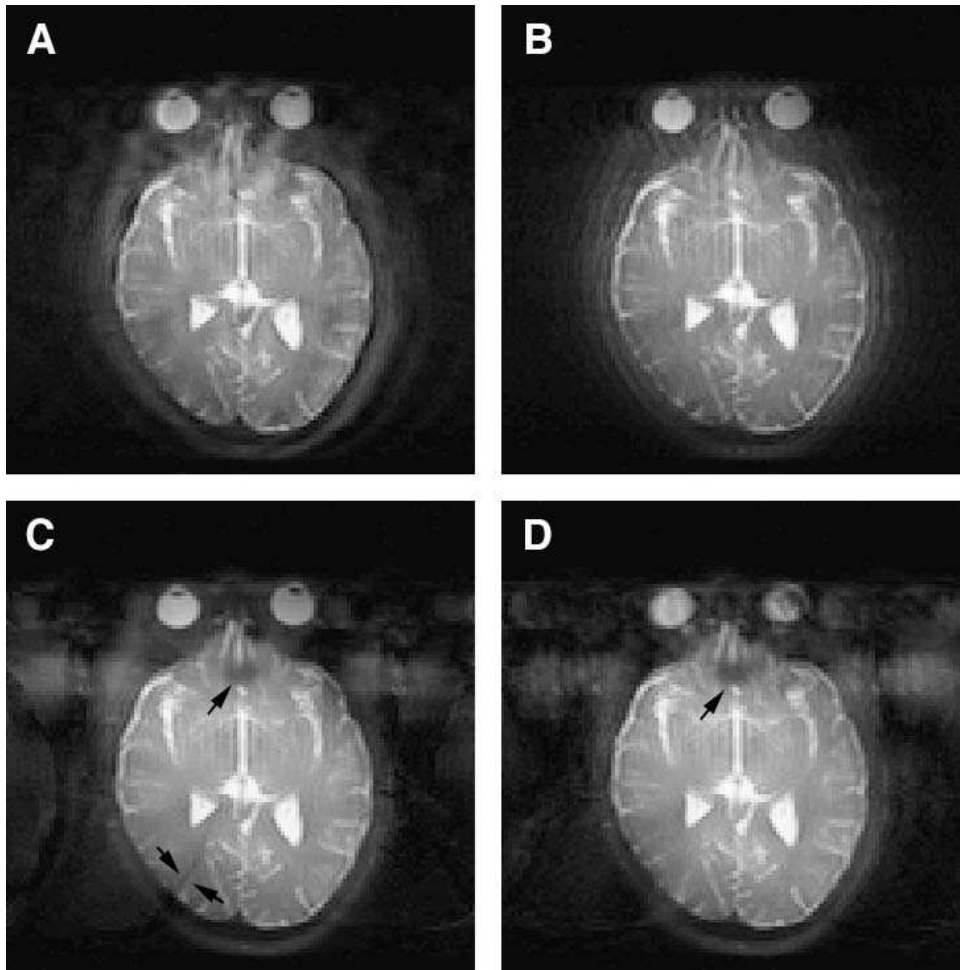


Figure 3.5: The same as Fig. 3.4 but for a slice at the level of the sinuses.

smoothness of the resulting amplitude modulation given by the conventional centric scheme depends on the relationship between the average T_2 and T_2^* values.

It was also found that conventional centric and centric TIPE images had similar SNR and that this was approximately 10 % higher than the SNR of centric GRASE and kb centric GRASE images. This is most probably due to the fact that the conventional centric and centric TIPE phase-encoding schemes bring more signal to the center of k -space (*c.f.* Fig. 2.4). For all phase-encoding schemes investigated there was a visible improvement in image quality when using fat suppression.

In summary, the possibility of obtaining images from a template interactive phase-encoding (TIPE) has been demonstrated. Unlike previous phase-encoding schemes proposed for GRASE, the centric TIPE scheme allows for a smooth amplitude modulation of the signal in the phase encode direction. This is independent of whether the imaged region corresponds to one of high or low susceptibility induced field inhomogeneities. Both conventional centric and centric TIPE phase-encoding schemes produce low frequency artifacts in the phase encode direction. In the conventional centric scheme the source of the artifacts is the modulation of both the amplitude and the phase of the signal in k -space. The centric TIPE scheme is mainly sensitive to phase artifacts only. Therefore, centric TIPE images are of most use when imaging regions where a good phase correction can be achieved. In regions with high field inhomogeneities where the average phase correction is poor, other phase-encoding schemes with lower intrinsic phase modulations might be preferable.

Chapter 4

Application of GRASE for BOLD fMRI

Having implemented GRASE and having investigated which phase-encoding schemes give the least artifacts in different brain regions, this chapter examines the use of GRASE for BOLD-based fMRI (*c.f.* section 1.4).

The first section of the chapter investigates the intrinsic BOLD contrast capabilities of GRASE by using a computer simulation. The second section examines a method for incorporating BOLD contrast in GRASE by use of a T_2^* preparation experiment and the displaced-echo technique. The third section demonstrates the application of BOLD-based GRASE in fMRI of the visual cortex using the displaced-echo technique. The fourth section compares the image quality of displaced GRASE with EPI images in regions of the brain that have short T_2^* . In the last section a simple computational model is used to compare the functional sensitivity of displaced GRASE with that given by GE-EPI and SE-EPI in regions with short T_2^* .

4.1 Intrinsic sensitivity of GRASE for BOLD fMRI

When considering GRASE for BOLD-based fMRI it is of interest to know whether the intrinsic contrast of GRASE will provide the desired BOLD sensitivity (i.e., sensitivity to detect principally T_2^* changes). This is in principle not clear because GRASE uses both gradient- and spin-echoes (T_2^* and T_2 contrast respectively).

A computer simulation was performed which was aimed at investigating how the intrinsic functional contrast of GRASE compares with that given by pure gradient-echo (which give the maximum BOLD sensitivity) and spin-echo sequences. The calculations of the functional contrast were performed for different effective echo times to find the conditions of optimum BOLD sensitivity.

The NMR signals originating from human cortical gray matter during the stimulation (S_a) and control (S_c) intervals of an hypothetical functional experiment were considered. The functional contrast ($\Delta S = S_a - S_c$) was calculated from the simulated image intensities given by GRASE, gradient-echo and spin-echo sequences (S_{GRASE} , S_{GE} and S_{SE} respectively).

For analytical convenience the following assumptions were made:

a) the image intensity is considered to be the magnitude of the NMR signal intensity acquired at the zero phase encoding step. For the three sequences considered the zero phase encoding step can occur at any of the echoes measured along the echo train. The three sequences are considered as single shot methods with unity gain and initial amplitude.

b) The signal is assumed to decay exponentially so that for GE and SE sequences the image intensity is given by:

$$S_{GE} = \exp(-R_2^* t) \quad (4.1)$$

$$S_{SE} = \exp(-R_2 t) \quad (4.2)$$

respectively, where R_2^* and R_2 are the tissue transverse relaxation rates for cortical gray matter and t is the time between the first excitation pulse and the center of the echo encoded with the zero phase encoding step (i.e., the TE_{eff}). The assumed exponential behaviour leads to a linear increase of relative signal changes with increasing echo time, which is supported by experimental results [98, 99].

c) R_2^* can be separated into reversible R_2' and irreversible R_2 contributions so that

$$R_2^* = R_2 + R_2' \quad (4.3)$$

d) the signal intensity for a GRASE sequence was assumed to be:

$$S_{GRASE} = \exp(-R_2 t - R_2' |t - i_p TE|) \quad (4.4)$$

This equation is equivalent to equation 2.1 without the phase term (now magnitude signals are being considered). The variables are as defined in equation 2.1. The echo time TE depends on the number of gradient echoes N_g acquired per RF interval, which is normally odd (c.f. section 1.3.3). To calculate TE we used the following expression [47]:

$$TE = N_g (s + t_{acq}) + pulse + 2 blip - s \quad (4.5)$$

where t_{acq} is the acquisition time, s is the time interval between consecutive acquisition windows, $pulse$ is the duration of the RF refocusing pulse and $blip$ is the time interval between the end of the refocusing pulse and the start of the first acquisition window. Considering the experimental conditions described in the previous chapter we have $t_{acq}=1.28\text{ms}$ (for collecting 128 complex points sampling at 100 kHz), $s=1.6\text{ms}$, $pulse=2\text{ms}$ and $blip=1\text{ms}$.

e) The T_2^* contrast of a particular gradient-echo is defined by the time interval between the center of the considered echo and the center of the spin-echo in a RF interval. Thus, the T_2^* contrast will depend on the particular gradient-echo as well as on the delays t_{acq} and s . To reduce the number of variables it was assumed for the simulation that the delays t_{acq} and s were fixed to the above mentioned values. The T_2^* contrast was therefore varied by considering different gradient-echoes for a given N_g and also by considering different values for N_g .

f) The simulation was performed to consider the intrinsic functional sensitivity of GRASE in two different brain areas: areas with long T_2^* and areas with short T_2^* . T_2^* is long in regions with low magnetic field inhomogeneities such as the visual cortex. Hence, based on fMRI experiments performed in the visual cortex at 3 Tesla the following values were chosen: $T_2^* = 30\text{ms}$ and $\Delta R_2^* = -2 \text{ Hz}$ [92]. For the short T_2^* (i.e., high magnetic field inhomogeneities) the following values were assumed: $T_2^* = 15\text{ms}$ and $\Delta R_2^* = -8 \text{ Hz}$. For this case the change in the relaxation rate ΔR_2^* corresponds to a change in T_2^* of approximately 2ms, as has been observed in the visual cortex. For both cases, high and low field inhomogeneities, the same T_2 (90ms) and ΔR_2 (-0.70 Hz) were used as these are less dependent on magnetic field inhomogeneities

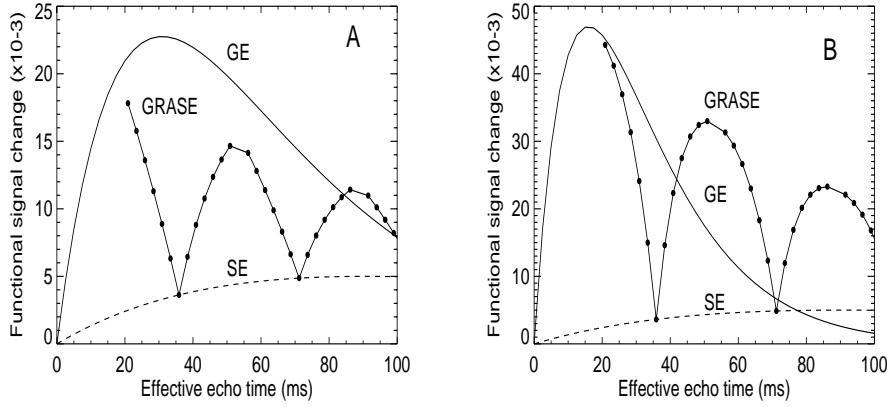


Figure 4.1: Functional signal change ΔS as a function of the effective TE for GRASE ($N_g = 13$, dots), gradient-echo (solid line) and spin-echo (dashed line) sequences for cortical tissue having $T_2^* = 30\text{ms}$ (A) and $T_2^* = 15\text{ms}$ (B).

(diffusion effects which may bring some dependency of ΔR_2 on magnetic field inhomogeneity are neglected).

With these assumptions the functional signal change ΔS was calculated as a function of the TE_{eff} for the GRASE, gradient-echo and spin-echo sequences.

Figure 4.1 shows the calculated functional signal changes ΔS for $T_2^* = 30\text{ms}$ (A) and for $T_2^* = 15\text{ms}$ (B). The signal changes are plotted as function of the TE_{eff} for the different sequences: GE (solid line), GRASE (dots) and SE (dashed line). The GRASE sequence has $N_g=13$ gradient echoes between consecutive 180° pulses and for convenience all points are joined, including the periods occupied by the 180° pulses.

Similarly to GE and SE sequences, the signal change ΔS in GRASE (Fig. 4.1) shows a maximum for an optimum TE_{eff} ($TE_{opt} \approx 20\text{ms}$ for the two considered cases). This means that when $TE_{eff} = TE_{opt}$, the NMR signal response upon stimulation is maximized. For GE and SE sequences $TE_{opt} = T_2^*$ and $TE_{opt} = T_2$, respectively. This can easily be proved by taking the derivate of ΔS with respect to TE_{eff} and equating to zero.

The local minima points in the GRASE curves in figure 4.1 correspond to the TE_{eff} where the Hahn echoes occur. Hence for these points GRASE and SE give the same results. The functional signal change ΔS increases locally as one moves away from the Hahn echoes because R_2^* contrast is introduced. Local maxima occur at the times where the outermost gradient echoes are applied. In the examples shown in Fig. 4.1, both GRASE sequences give the optimum signal change when the TE_{eff} corresponds to the first echo of the echo train. For this echo the T_2 weight is minimum and the T_2^* weight maximum.

Table 4.1 shows, for the case of $T_2^* = 30\text{ms}$, how the optimal functional signal change given by GRASE can be made similar to the optimum signal change of a GE sequence by increasing the number of gradient echoes N_g per RF interval. From left to right the columns in table 4.1

N_g	TE (ms)	TE_{opt} (ms)	ΔS (%)
1	5	91	22
7	20	13	51
13	35	21	78
27	70	38	95
35	90	48	89

Table 4.1: Optimum functional signal change ΔS given by GRASE with different N_g relative to the optimum signal change given by a GE sequence for the case when the cortical tissue has $T_2^* = 30\text{ms}$ and $T_2 = 90\text{ms}$. The case $N_g=1$ represents a pure SE sequence. As N_g increases GRASE becomes more similar to a SE-EPI sequence.

give N_g , the resulting echo time TE in the GRASE sequence, the optimum echo time TE_{opt} of GRASE and the signal change of GRASE relative to that of GE when $TE_{eff} = T_2^*$.

Table 4.1 shows that a pure SE sequence $N_g=1$ gives very little functional sensitivity compared to a GE sequence. Increasing N_g increases the available T_2^* contrast in GRASE so that the optimal functional signal change becomes more similar to that given by a GE sequence. It is found that in general both GE and GRASE sequences give similar optimum signal changes (with differences less than 10 %) when the TE_{opt} of GRASE corresponds to the first echo of the echo train and when the time interval between this echo and the first Hahn echo (i.e., approximately $TE/2$) is similar to the T_2^* of the active tissue. For example, when $T_2^* = 15\text{ms}$ (c.f. Fig. 4.1B) the optimum functional signal change of GRASE is 94 % of that given by GE when $N_g = 13$. If N_g is further increased then the increase in TE results in an increase of the T_2 weight which reduces the functional sensitivity compared to a GE sequence. This can be seen in table 4.1 when N_g is increased from 27 to 35 gradient echoes per RF refocusing interval.

Summarizing, the simulation shows that in principle the intrinsic BOLD contrast of GRASE can be used to give a similar functional sensitivity to that given by a pure GE sequence. This, however, can only be done by having a number of gradient echoes per RF interval which is considerably long, even in the case when T_2^* is as short as 15ms. In the literature, however, the advantages of GRASE (lower image distortions and lower signal loss than EPI) have been reported when using $N_g = 3$ or 5. For higher N_g such as those required for optimum BOLD sensitivity, GRASE would become more like a SE-EPI sequence, which is known to give image distortions and signal loss, particularly in regions with high field inhomogeneities. In addition, it has been assumed that the optimum BOLD contrast can be achieved by having the optimum T_2^* weighted echo at the center of k -space. However, no considerations were made for the fact that when N_g increases also the image artifacts increase as a result of the increased amplitude and phase modulations of the signal in k -space. Therefore, using the intrinsic BOLD contrast for GRASE will lead to similar difficulties as encountered with EPI in regions with short T_2^* , and will probably be even worse due to additional artifacts. Hence, to use GRASE in such a way that it offers advantages with respect to EPI, an alternative method for incorporating BOLD contrast should be considered which allows the use a low number of gradient echoes per RF interval. In this way, GRASE will offer an improved image quality through reduced distortions and signal loss. The following section describes a method for incorporating BOLD contrast in a GRASE sequence by using a T_2^* preparation experiment, thus largely independently from N_g .

4.2 Additional T_2^* contrast for GRASE

4.2.1 T_2^* preparation experiment

In a basic GRASE sequence the first 90° pulse generates transverse magnetization and a train of equidistant 180° pulses is used to refocus the magnetization. The low intrinsic T_2^* contrast is obtained by the gradient echoes measured at the sides of the Hahn echo during each RF-refocusing interval.

T_2^* contrast can be increased in a GRASE sequence with a preparation experiment which simply consists of including an additional delay τ between the first 90° pulse and the first refocusing pulse [100]. Thus, considering only the timing of the RF pulses the T_2^* -weighted GRASE sequence may be represented as

$$90^\circ - \tau - TE/2 - \alpha - TE/2 - \alpha - TE/2 \dots$$

where the refocusing flip angle α is normally 180° but can also be less if lower power deposition is required. The delay τ takes positive values and directly determines the degree of T_2^* contrast. Figure 4.2 schematically shows how the delay τ incorporates T_2^* weighting by creating a decay of assymetric spin-echoes. Using eq. (4.4), when no preparation experiment is used ($\tau=0$), the second echo is a pure spin-echo with signal intensity $S(\tau = 0) = \exp(-TE \cdot R_2)$. With a preparation experiment the signal of the same echo becomes

$$S(\tau) = \exp(-(TE + \tau) \cdot R_2 - \tau \cdot R_2') \quad (4.6)$$

and using eq. (4.3)

$$S(\tau) = \exp(-TE \cdot R_2 - \tau \cdot R_2^*) \quad (4.7)$$

which shows how the T_2^* -weighting is incorporated by the delay τ with a preparation experiment.

4.2.2 T_2^* -weighted GRASE: displaced-echo method

Unfortunately, a T_2^* preparation experiment does not only affect the magnitude but also affects the phase of the magnetization. Owing to this, some additional considerations are necessary for a T_2^* -weighted GRASE sequence.

In GRASE the use of non-perfect RF refocusing pulses will generate families of spin- and stimulated-echoes which can interfere during the signal acquisition periods. The well-known CPMG condition is conventionally used to ensure the constructive interference of all refocusing pathways [6]. This, however, makes the sequence sensitive to the phase of the magnetization. After a T_2^* -weighted preparation experiment the phase of the magnetization will be undetermined and therefore the CPMG condition will no longer hold. A T_2^* preparation experiment may be seen as having the effect of introducing some additional dephasing which causes the odd and even echo coherence pathways to no longer to be in phase in a CPMG sequence (*c.f.* section 1.1.7). For this reason a simple T_2^* -weighting experiment followed by a conventional GRASE sequence will lead to an image with interference artifacts.

It is therefore necessary to modify the conventional GRASE sequence so that it becomes insensitive to the phase of the magnetization. This can be achieved by use of the displaced-echo acquisition technique which has already been proposed for RARE-based sequences [22, 23]. The

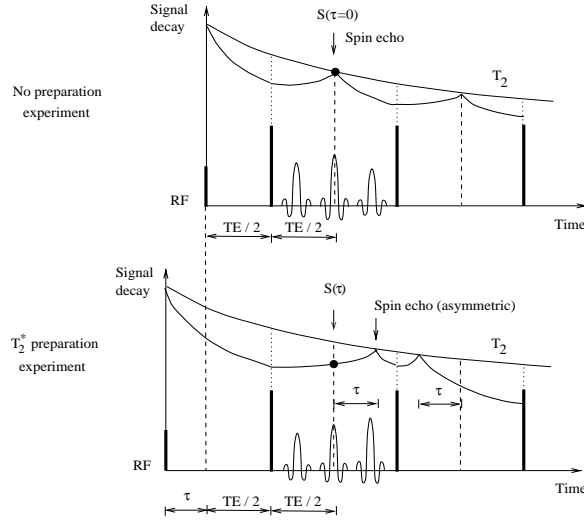


Figure 4.2: Signal decay of a GRASE sequence with (bottom) and without (top) a T_2^* preparation experiment. The signal magnitude of the first spin echo is $S(\tau = 0) = \exp(-TE \cdot R_2)$ with no preparation experiment. Through the incorporation of the delay τ the same echo becomes T_2^* -weighted (eq. (4.7)). See text for more details.

implementation of the displaced-echo method for a GRASE sequence is analogous. A displacing read gradient of appropriate strength ΔG_r is used to select either odd or even echoes originating from the spin-echo and stimulated-echo families, hence avoiding interference effects [22, 23]. An additional T_2^* preparation experiment will now have the desired effect of weighting the image intensity with the tissue T_2^* but without introducing interference-related artifacts.

Similarly as with RARE, in a GRASE sequence the echo parity to be acquired is selected by the position of ΔG_r with respect to the acquisition windows between two consecutive RF refocusing pulses: the odd parity group can be selected by placing ΔG_r after the last acquisition window whereas the even parity group can be selected by placing ΔG_r before the first acquisition window. In principle one is free to select even or odd echoes, or a combination of both if the position of the displacing gradient ΔG_r is alternated along the echo train. However, even echoes are preferable because they are less susceptible to gradient imperfections [23]. We therefore implemented displaced GRASE with the displacing read gradient positioned so as to select the even echoes.

Figure 4.3 shows a diagram of the pulse sequence used. It consists of a T_2^* -preparation experiment, determined by the delay τ , followed by a GRASE sequence with three gradient echoes per refocusing pulse. The displacing read gradients, shown with shaded areas, select the even echoes, which can first be measured after the second RF refocusing pulse.

The intensity of the echoes along the echo train is markedly different during the first RF refocusing pulses and tends to a steady state at the end of the echo train. Dummy repetitions (*c.f.* Fig. 4.3) and optimized refocusing flip angles can be used to equalize the signal intensities

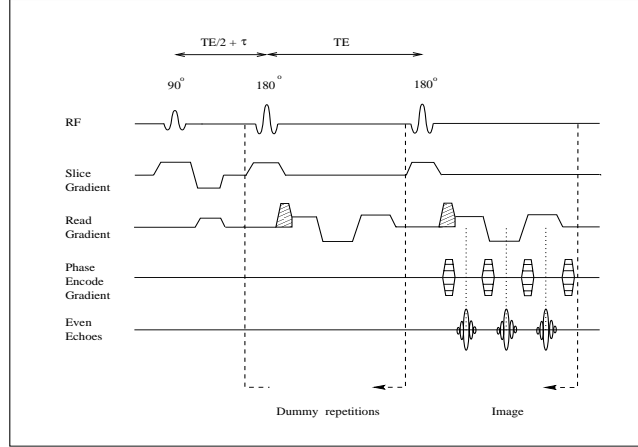


Figure 4.3: Displaced T_2^* -weighted GRASE pulse sequence. An imbalanced read gradient (shaded area) of proper strength selects the even parity echoes under each acquisition window after the second RF refocusing pulse. The T_2^* -weighting is achieved by means of the delay τ between the excitation pulse and the first refocusing pulse. Dummy repetitions can be used to let the intensities of the even echoes reach steady state before starting the phase-encoding.

before phase-encoding at the cost of reduced SNR [101]. When acquiring the even parity echoes one dummy scan is always necessary (*c.f.* Fig. 1.5B). When the echoes reach steady state they have a signal intensity that is 50% of the intensity that they would have in a conventional (coherent) CPMG sequence [22, 23]. An advantage of the TIPE method for displaced-echo imaging is the fact that in principle no dummy scans are necessary to reach echo stabilization along the echo train. This is because the TIPE method takes into account the intensity of the echoes when reordering them in k -space without assuming that signal decays in a purely monotonic fashion. For this reason the first high intensity echoes can be used to sample the central area of k -space thus giving a better SNR.

An alternative to the displaced-echo technique is given by the split-echo method [102, 103, 91]. In this method both echo parities are displaced so that they do not interfere while still remaining in the acquisition window, hence allowing their simultaneous acquisition after a single excitation (*c.f.* Fig. 1.5B). The signals from the two echo parities give separate images which can be added to form the final image. A disadvantage of the split-echo method relative to the displaced-echo is that the simultaneous phase-encoding of the two echo parities may lead to very different k -space weighting in the separate images when few dummy scans are used. In addition, there is no SNR advantage in a split-echo image relative to a displaced-echo image obtained with half the acquisition bandwidth.

To evaluate T_2^* -weighted GRASE, conventional and displaced GRASE images were compared with ($\tau=30\text{ms}$) and without ($\tau=0\text{ms}$) a T_2^* -weighting preparation experiment using the whole-body gradient set. Figure 4.4 shows a example of such a comparison. All images in Fig. 4.4 correspond to the same axial slice, with a FOV of $20 \times 20 \text{ cm}^2$. The acquisition matrix was

128x99 and image reconstruction size was 128x128. Images were obtained using the centric TIPE method. It can be seen that when there is no additional T_2^* contrast ($\tau=0\text{ms}$) both conventional (Fig. 4.4a) and displaced GRASE (Fig 4.4c) give very similar image quality. A direct measurement of the SNR in different image areas reveals that in the same areas the SNR of the displaced GRASE image ($\tau=0\text{ms}$) is approximately 60 to 70 % of the SNR in the conventional GRASE image.

Similar results are obtained in different image slices and different volunteers. Increasing the T_2^* contrast in the conventional GRASE image (Fig. 4.4b, $\tau=30\text{ms}$) gives rise to clear interference artifacts which are significantly less noticeable in the T_2^* -weighted displaced GRASE image (Fig. 4.4d, $\tau=30\text{ms}$). Increasing the T_2^* contrast in the displaced GRASE image increases the signal loss in areas where the field inhomogeneities are stronger. It was further observed that when using strong T_2^* -weighting such as $\tau=30\text{ms}$, similar image quality was observed in GRASE images obtained with or without fat suppression. This is most probably due to the short T_2^* of the fat signal.

4.3 Use of displaced GRASE based BOLD in the visual cortex

To demonstrate the use of GRASE for fMRI a comparison should be made with EPI and a stimulation protocol that gives well known, reproducible and preferably strong brain activation. Owing to the inherent disadvantages of EPI, such an experiment would be difficult when considering areas of the brain with short T_2^* . The visual cortex is, however, an area of the brain well known for giving strong and reproducible activation. Although this is not an area where high field inhomogeneities are present, it was decided to investigate the use of T_2^* -weighted GRASE using a conventional visual stimulation paradigm.

In the experiments described here the interest was in imaging axial slices at the level of the calcarine sulcus. Such slices have low susceptibility-induced field inhomogeneities and therefore the centric TIPE method was adopted.

The centric TIPE method was implemented for multislice acquisition mode. This means that for each slice the optimal phase-encoding order was calculated (optimum in terms of amplitude modulation in k-space) from a template scan of the corresponding slice. In the functional experiments one steady-state template scan was used to calculate the phase-encoding and perform phase correction of the whole image time series of the corresponding slice.

For the functional study sagittal scout images were obtained through the occipital pole to localize the calcarine fissure. The anatomical images consisted of three axial oblique multislice segmented IR-RARE images obtained parallel to the calcarine fissure (512x512, TI = 600ms, TE = 6ms, TR = 3.9s, RARE factor = 8, slice thickness = 5mm, slice center gap = 7mm, FOV = 25x25 cm²).

The functional sensitivity of displaced GRASE was investigated in seven healthy human subjects (*c.f.* Appendix A) using the whole-body gradient set. A T_2^* -weighting of $\tau=30\text{ms}$ was used, the choice of which was based on previous measurements of the average T_2^* in gray matter in the visual cortex at 3 Tesla [92]. No fat suppression was used. The data matrix was 128x64 with an acquisition bandwidth of 100 kHz. Single-shot functional EPI images were acquired in all volunteers as a control (blipped GE-EPI with linear phase-encoding, TE=30ms, 128x64,

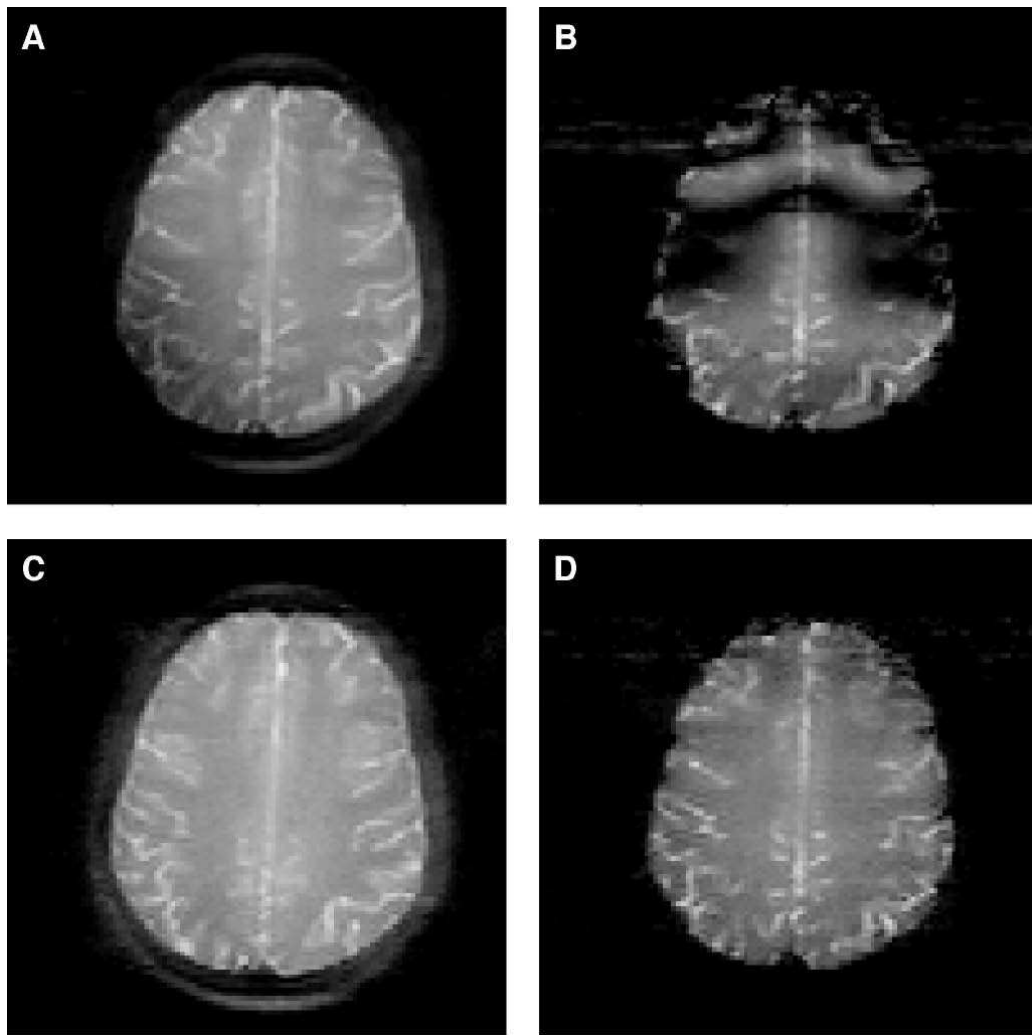


Figure 4.4: Comparison of conventional GRASE with displaced GRASE with and without a T_2^* -weighting preparation experiment: A) conventional GRASE ($\tau=0\text{ms}$), B) conventional GRASE ($\tau=30\text{ms}$), C) displaced GRASE ($\tau=0\text{ms}$), D) displaced GRASE ($\tau=30\text{ms}$). The displaced method reduces considerably the amount of interference artifacts in T_2^* -weighted GRASE images.

100 kHz). The total imaging time for a single slice was 283ms for GRASE and 82ms for EPI. The T_2^* -weighting of $\tau = 30$ ms in EPI was achieved by asymmetrically sampling k -space. The GRASE and EPI images were acquired with the same FOV, slice positions and orientations as used for the anatomical images. Both EPI and displaced GRASE images were reconstructed with a data matrix of 128×128 giving a subsequent in-plane resolution of $2 \times 2 \text{ mm}^2$.

Visual stimulation was performed using LED goggles (Grass, W. Warwick, RI) and consisted of a full field red-black flashing checkerboard pattern (8 Hz) during stimulus and black field during control. The imaging sequence was used to trigger the stimulus in order to ensure the synchronization of the data acquisition and the stimulation paradigm. In each of the three contiguous axial slices defined by the anatomic images, imaging data were acquired during five control and four task periods that were interleaved; five images were acquired in each of the nine consecutive periods with $TR = 4$ s. With this paradigm a single functional experiment took 3 min and required the acquisition of 45 images. No signal averaging was performed.

For the functional analysis the AFNI Software package was used [104]. The reconstructed images were first motion corrected and then cross correlation maps of the pixels' time series with an ideal box-car waveform were obtained [105]. The box-car waveform represents the expected activation-induced signal response. Maps giving the average percent signal change were also calculated. A correlation coefficient of 0.6 was chosen as threshold value to display the percent signal change maps. The statistical significance of a correlation coefficient of 0.6 with 45 measured points corresponds to a probability of 99.994 % that the observed correlation has not occurred by chance [105]. Pixels with a correlation coefficient above the threshold were encoded with a color scale giving their percent signal change and overlaid on the corresponding high resolution anatomical images.

Figure 4.5 shows an example of single-shot multislice axial T_2^* -weighted displaced-echo GRASE images (Fig. 4.5a) and the corresponding EPI images (Fig. 4.5b). By comparison with the anatomical images shown in Fig. 4.6 it can be seen that GRASE images show less distortion.

The SNR was measured from the EPI and GRASE images in an area approximately covering the visual cortex. The measurements were performed for the 7 volunteers and the 3 slices and on images acquired at the middle of the time series, i.e., when steady state had been achieved. The result was that on average the SNR given by GRASE is (47 ± 7) % of the SNR given by EPI.

Figure 4.6 shows the functional maps overlaid on anatomical images corresponding to Fig. 4.5. The functional maps (Fig. 4.6a for GRASE and Fig. 4.6b for EPI) were obtained from the same subject, using the same stimulation paradigm and the same T_2^* -weighting. Both imaging methods show significant positive signal changes located predominantly in the visual cortex during stimulation. Displaced GRASE shows, however, less activation than EPI.

Figure 4.7 shows a histogram with the number of total activated pixels (having correlation coefficient greater than 0.6) for GRASE (dark bars) and EPI (light bars). The results of all volunteers and slices were considered together. This is allowed because for each single volunteer and slice the activity histogram has a similar form, the number of activated pixels being volunteer dependent. When all the data is grouped, the differences between EPI and GRASE accumulate and become clearer. This histogram shows that, when looking at the visual cortex, EPI gives more activated pixels than displaced GRASE with the same T_2^* -weight. In particular, EPI gives more pixels with stronger functional activation than does GRASE.

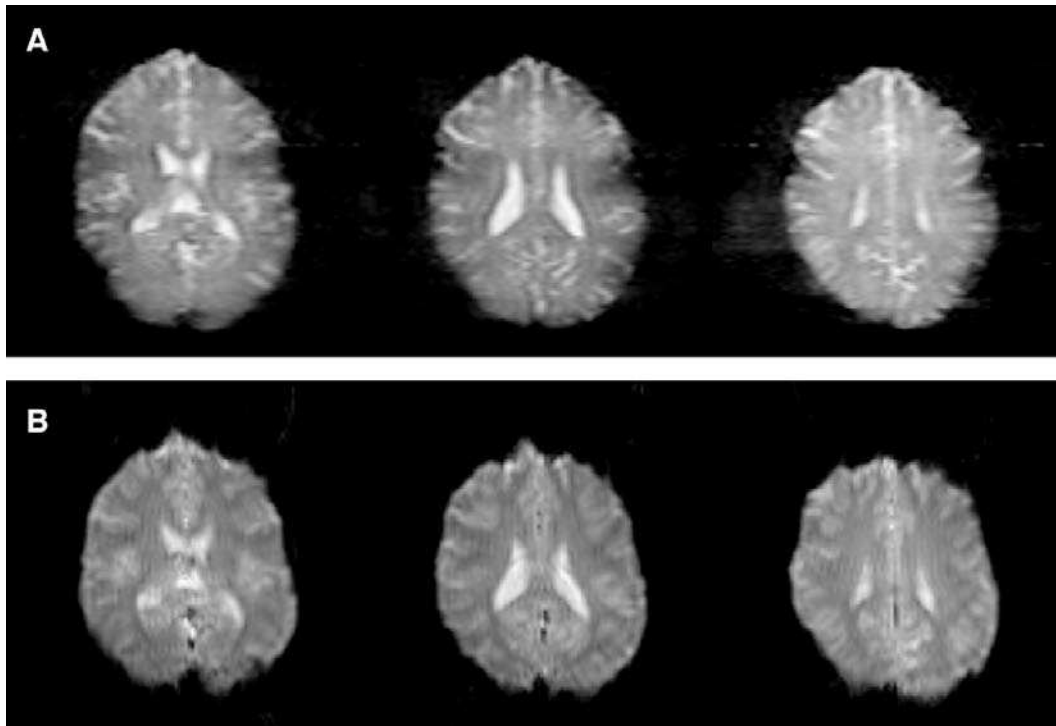


Figure 4.5: Single-shot multislice T_2^* -weighted displaced-echo GRASE (a) and EPI (b) images from the time series of a fMRI experiment in the visual cortex. The T_2^* -weight was $\tau=30\text{ms}$ for both GRASE and EPI. See text for more details.

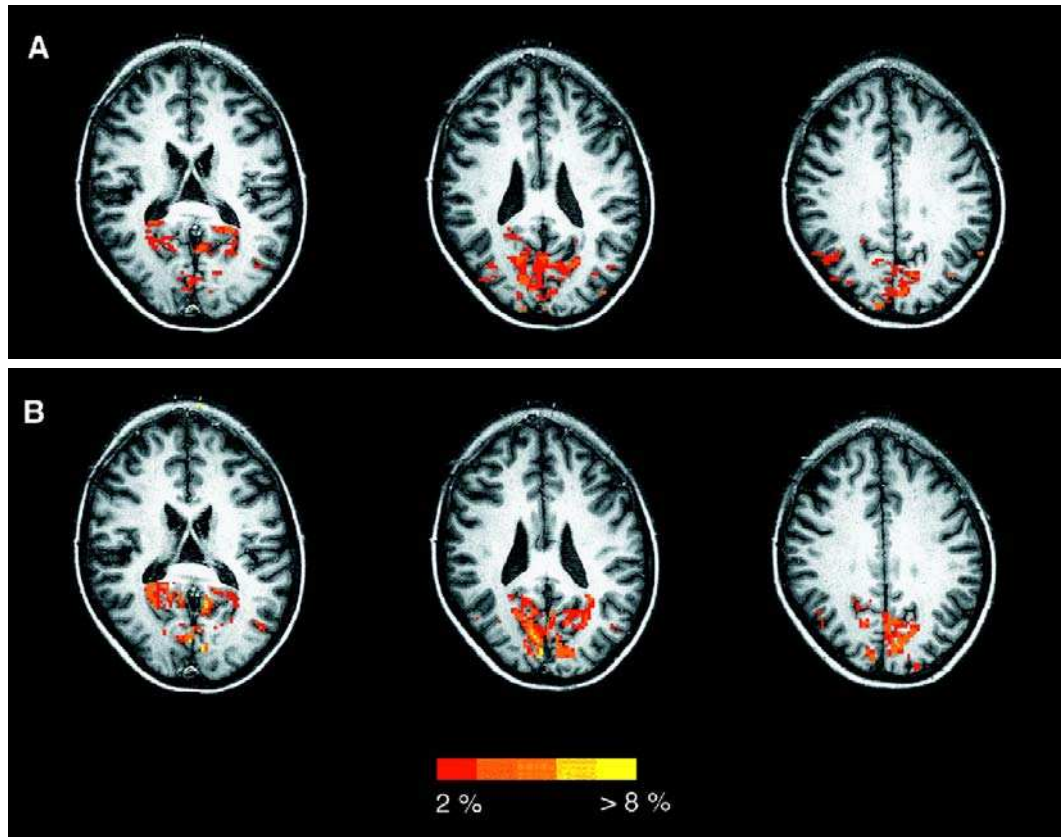


Figure 4.6: Functional maps overlaid on anatomical images for GRASE (a) and for EPI (b). The maps correspond to the images shown in Fig. 4.5.

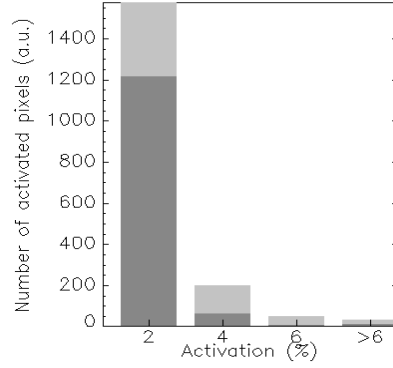


Figure 4.7: Histogram of the total measured activated pixels in EPI (light bars) and GRASE (bars) fMRI studies of the visual cortex (7 volunteers, 3 slices per volunteer). The bars indicate the number of pixels which showed activation under 2%, between 2 and 4%, between 4 and 6% and above 6%. Only pixels with a correlation coefficient greater than 0.6 were considered.

The relative functional contrast to noise ratio of EPI and GRASE may be estimated by comparing the averaged activation-induced signal changes ($\overline{\Delta S}$) and signal fluctuations in a region of with non-activated pixels (σ) for both both sequences,

$$\frac{\text{CNR}_{\text{EPI}}}{\text{CNR}_{\text{GRASE}}} = \frac{\overline{\Delta S}_{\text{EPI}}}{\overline{\Delta S}_{\text{GRASE}}} \frac{\sigma_{\text{EPI}}}{\sigma_{\text{GRASE}}} \quad (4.8)$$

Figure 4.8 shows an example of typical averaged time courses obtained with GRASE and EPI in a single volunteer. For the activation curves the average is performed over the three imaged slices considering all pixels having a correlation coefficient larger than 0.6. For reference, the GRASE averaged time course of a small region containing non activated gray matter is also shown (time course labeled *Noise*). The corresponding non-activated time course for EPI in the same region is similar and is not shown. The signal intensities are displayed in arbitrary units. The data shown in Fig. 4.8 gives $\overline{\Delta S}_{\text{EPI}} \approx 0.17$ and $\overline{\Delta S}_{\text{GRASE}} \approx 0.11$. The standard deviation of the non-activated time course is $\sigma_{\text{EPI}} \approx 79$ and $\sigma_{\text{GRASE}} \approx 85$ for the same non-activated region. Using eq. (4.8) this leads to an approximate gain of a factor of 2 for the contrast to noise ratio of EPI compared to that of GRASE. Taking other regions with non-activated pixels (but always the same region for both GRASE and EPI) leads to similar results.

The reduced functional sensitivity of GRASE compared to EPI in this region of the brain is to be expected due to the lower SNR of GRASE owing to the displaced-echo technique.

4.4 Displaced GRASE in brain regions with short T_2^*

In the previous section the use of displaced GRASE for fMRI in a region with long T_2^* was demonstrated. In this section the image quality in regions with short T_2^* is examined using T_2^* -weighted displaced GRASE, GE-EPI and SE-EPI sequences using the head gradient set.

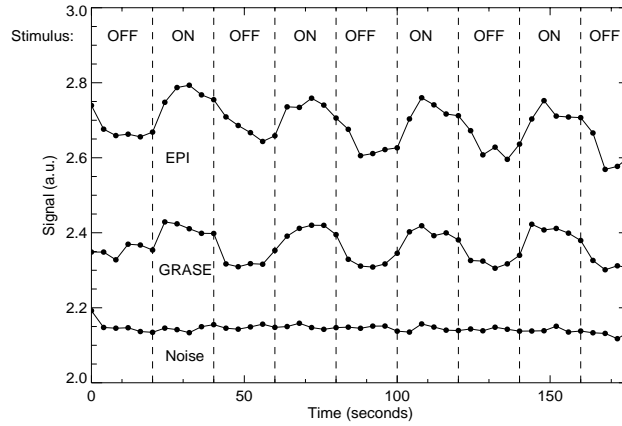


Figure 4.8: Average time courses from activated regions in EPI and GRASE images. The average was performed over the three slices of a volunteer and over all pixels having a correlation coefficient above 0.6. The off/on stimulation periods are separated by vertical lines. The average GRASE time course from a region of gray matter containing no activated pixels is also shown for reference (Noise). See text for more details.

Figure 4.9 shows an example of the results obtained. Displaced GRASE and EPI images were obtained from the same slice with $\tau=30\text{ms}$ (as used previously for optimal BOLD contrast in the visual cortex) and $\tau=10\text{ms}$, to investigate the contribution to the image of brain tissue with differing T_2^* values. Figure 4.9A is a high resolution (256×256) anatomical RARE image taken as reference (16 segments, $\text{TR}=5\text{s}$, $\text{TE}=20\text{ms}$). Figures 4.9B and 4.9C show the T_2^* -weighted SE-EPI ($\text{TE}=30\text{ms}$) and GRASE images with $\tau=10\text{ms}$, respectively. Figures 4.9D and 4.9E show the GE-EPI and GRASE images with $\tau=30\text{ms}$, respectively. The acquisition matrix of displaced GRASE and EPI images was 128×64 with a 100 kHz receiver bandwidth and the reconstructed image size was 128×128 . The length of the echo trains were 80ms for EPI and 248ms for GRASE. The phase-encoding direction was anterior-posterior and the FOV was $23 \times 23 \text{ cm}^2$. Displaced GRASE images were obtained using the centric GRASE phase-encoding order because in a slice with high field inhomogeneities this is the phase-encoding scheme that gives the least artifacts.

By comparison with the anatomical image, Fig. 4.9 shows that the distortions in EPI images along the phase-encoding direction are stronger than those seen in the displaced GRASE images, particularly in the areas with stronger field inhomogeneities (front of the brain) and for $\tau=30\text{ms}$. With the image parameters used, GE-EPI (Fig. 4.9D) showed higher SNR (by a factor of ≈ 2) than displaced GRASE (Fig. 4.9E) for $\tau=30\text{ms}$. The noise in both images is similar because the total effective acquisition time was the same for both methods (i.e., the same number of echoes and the same acquisition window per echo). For the low T_2^* contrast images displaced GRASE (Fig. 4.9C), showed similar SNR but less image distortions than spin-echo EPI (Fig. 4.9B). The same results were obtained on other slices through brain areas having strong field

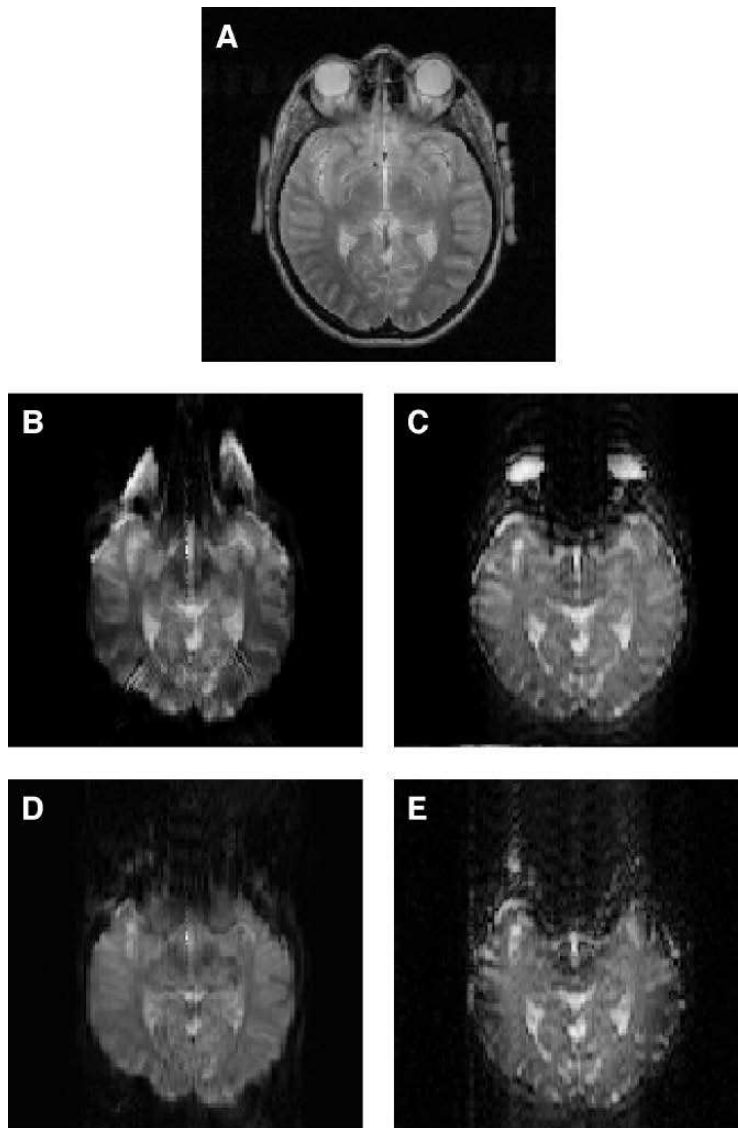


Figure 4.9: Comparison of image quality given by displaced GRASE, GE-EPI and SE-EPI with different T_2^* -weighting in a slice at the level of the sinuses: A) anatomical image for reference, B) SE-EPI with $\tau = 10\text{ms}$, $TE = 30\text{ms}$, C) GRASE with $\tau = 10\text{ms}$, D) GE-EPI with $\tau = 30\text{ms}$ and E) GRASE with $\tau = 30\text{ms}$.

inhomogeneities and different volunteers.

4.5 Functional sensitivity of displaced GRASE

The functional sensitivity of EPI and displaced GRASE in combination with a T_2^* preparation experiment was further examined by using a computational model. Similarly to the model used in section 4.1, it is assumed that the signal intensity of EPI and GRASE images is mainly given by the signal at the center of k -space. Thus, rewriting eqs. (4.1) and (4.7)

$$S_{\text{GE-EPI}} = \exp(-\tau / T_2^*) \quad (4.9)$$

$$S_{\text{GRASE}} = \frac{1}{2} \exp(-TE / T_2 - \tau / T_2^*) \quad (4.10)$$

where τ is measured from the RF excitation pulse and is the time when the center of k -space is sampled. For a GE-EPI sequence the shortest τ that can be achieved is normally limited to approximately half the length of the echo train. For a GRASE sequence TE is the time interval between consecutive RF refocusing pulses and τ is the delay used in the T_2^* preparation experiment, which can be varied continuously from zero. The factor $1/2$ in the GRASE signal accounts for the fact that with displaced GRASE there is a signal loss of approximately 50 % compared with coherent GRASE. This, however, may be rather conservative when using the TIPE scheme. It is further assumed that both imaging sequences have the same acquisition bandwidth, so that a comparison of their signals is equivalent to a comparison of their signal-to-noise ratios.

Assuming that the stimulation-induced signal changes in the gray matter are mainly due to changes in T_2^* ,

$$\Delta S_{\text{GE-EPI}} = \exp(-\tau / T_2^*) \cdot [\exp(-\tau \cdot \Delta R_2^*) - 1] \quad (4.11)$$

$$\Delta S_{\text{GRASE}} = \frac{1}{2} \exp(-TE / T_2 - \tau / T_2^*) \cdot [\exp(-\tau \cdot \Delta R_2^*) - 1] \quad (4.12)$$

where it was used that $\Delta S = S_a - S_c = S_c (S_a / S_c - 1)$ (*c.f.* section 4.1).

By taking the derivate with respect to τ and equating to zero it can be easily proved that both $\Delta S_{\text{GE-EPI}}$ and ΔS_{GRASE} have a maximum when $\tau = T_2^*$ of the cortical tissue giving activation. Therefore, if the conditions are such that it is possible to use the optimum T_2^* -weighting that maximises stimulation-induced signal changes, then using eqs. (4.9)-(4.12) a comparison between GE-EPI and GRASE sequences gives

$$\frac{\Delta S_{\text{GE-EPI}}}{\Delta S_{\text{GRASE}}} = \frac{S_{\text{GE-EPI}}}{S_{\text{GRASE}}} = 2 \cdot \exp(TE / T_2) \quad (4.13)$$

Equation 4.13 predicts that the functional sensitivity of GE-EPI will be at least a factor of 2 (for $TE \ll T_2$) better than that given by displaced GRASE in brain regions where the optimum $\tau = T_2^*$ can be used. This is in good agreement with the experimental results obtained when examining activation in the visual cortex.

It is of interest to compare the functional sensitivity of GRASE and EPI in brain regions where, due to local field inhomogeneities, the T_2^* of gray matter is shorter than the minimum T_2^* -weight (τ_{min}) achievable with GE-EPI. In such regions GE-EPI will not have the optimum functional sensitivity. However, owing to its higher signal it may still offer better functional sensitivity than GRASE for a range of cortical T_2^* s which are shorter than τ_{min} . When considering short T_2^* -weighting one should also consider SE-EPI (*c.f.* section 1.3.1) because for this method the optimum T_2^* -weight can be also varied continuously from zero similarly as with GRASE. With SE-EPI this can be achieved by sampling the center of k -space at a time τ after the spin-echo (*c.f.* Fig. 1.11), thus generating an assymetric spin-echo so that

$$S_{SE-EPI} = \exp(-\widetilde{TE} / T_2 - \tau / T_2^*) \quad (4.14)$$

and

$$\Delta S_{SE-EPI} = \exp(-\widetilde{TE} / T_2 - \tau / T_2^*) \cdot [\exp(-\tau \cdot \Delta R_2^*) - 1] \quad (4.15)$$

where \widetilde{TE} is the echo time and normally the shortest value that it can take is $\widetilde{TE} = ETL - 2\tau$, ETL being the length of the EPI echo train.

A comparison of the SNR given by displaced GRASE and SE-EPI gives

$$\frac{S_{SE-EPI}}{S_{GRASE}} = 2 \cdot \exp((TE - \widetilde{TE}) / T_2) \quad (4.16)$$

where eqs. (4.14) and (4.10) have been used. Equation (4.16) predicts that for the experimental conditions used in the previous section ($TE = 10\text{ms}$, $\widetilde{TE} = 60\text{ms}$, $T_2 \approx 90\text{ms}$), SE-EPI and displaced GRASE will have similar SNR, which is in agreement with the experimental results.

In what follows the model will be used for estimating the activation-induced signal changes given by GE-EPI, SE-EPI and displaced GRASE in cortical tissues having $T_2^* \leq \tau_{min} = 30\text{ms}$. The value of τ_{min} was based on the experimental conditions described in the previous section (100 kHz, 128x64 data matrix, with assymmetric sampling of k -space). For the calculation of the functional signal changes eqs. (4.11), (4.15) and (4.12) were used. For GE-EPI the T_2^* -weighting was fixed to $\tau = \tau_{min}$. For SE-EPI and GRASE the T_2^* -weighting was set for optimum BOLD contrast, thus $\tau = T_2^*$. The echo time for GRASE was fixed to $TE = 10\text{ms}$. For SE-EPI the echo time was chosen so that it would give the minimum possible T_2 -weighting for each τ , hence $\widetilde{TE} = 2(\tau_{min} - \tau)$. This is an idealization because \widetilde{TE} may be made unrealistically short by choosing $\tau \approx \tau_{min}$ in which case SE-EPI would have essentially a pure T_2^* contrast. In a real situation there is a practical limit for the shortest \widetilde{TE} owing to the finite time used by the RF pulses and the gradients. Therefore, this assumption overestimates the signal intensity of SE-EPI when $T_2^* \approx \tau_{min}$. As previously (section 4.1), it was assumed that $T_2 = 90\text{ms}$ and that the activation-induced change in the relaxation rate is $\Delta R_2^* = -8 \text{ Hz}$, which approximately corresponds to a 2ms change in cortical tissue having $T_2^* = 15\text{ms}$ when not activated.

Figure 4.10 shows the results of calculating ΔS_{GE-EPI} , ΔS_{SE-EPI} and ΔS_{GRASE} with these assumptions. It can be seen from Fig. 4.10 that GE-EPI is expected to give better functional sensitivity than SE-EPI and displaced GRASE in cortical tissue having T_2^* s longer than approximately 13ms. For tissues having T_2^* shorter than approximately 13ms, SE-EPI provides higher functional signal change than both GE-EPI and displaced GRASE. The simulation gives similar results when using different values for the assumed T_2 (from 70 to 120ms) and different changes in the relaxation rate ΔR_2^* (from -1 to -30 Hz).

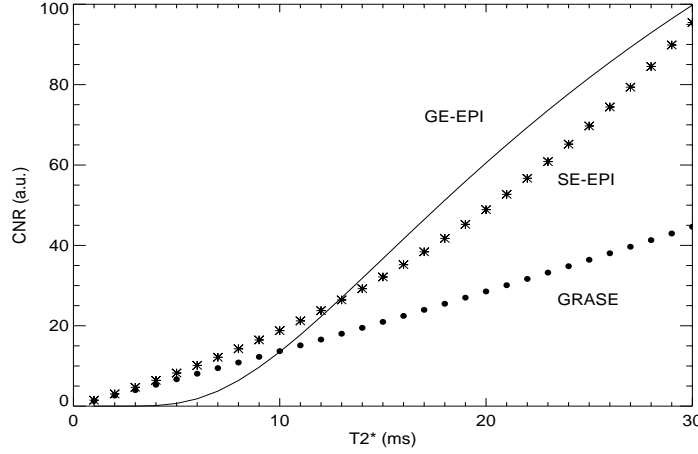


Figure 4.10: Simulation of the activation-induced signal changes given by GE-EPI (solid line), SE-EPI (stars) and displaced GRASE (dots) for cortical tissues having $T_2^* \leq \tau_{min} = 30\text{ms}$. It is assumed that the experimental conditions are such that the minimum T_2^* -weight obtainable with GE-EPI is τ_{min} .

However, based on the experimental results from the previous section, it is known that for short T_2^* -weighting displaced GRASE gives a better image quality than SE-EPI. In addition, the image distortions and signal loss from EPI depend on the local magnetic field inhomogeneities and are thus slice and subject dependent. This is a limitation for EPI in fMRI studies involving averaging across subjects, where functional maps which are less prone to subject-dependent artifacts are preferable in order to detect small signal changes in areas with low activation. Therefore, in these situations it is to be expected that owing to its higher image quality, displaced GRASE may still be preferred to EPI for functional imaging of cortical tissue with short T_2^* . For T_2^* under approximately 10ms GRASE should be clearly better due to its higher image quality and similar functional sensitivity to SE-EPI. On the other hand, above 20ms GE-EPI should be better owing to its much higher functional sensitivity. Therefore, for the experimental conditions here investigated the transition must be somewhere between these values. Hence, it is concluded that for T_2^* up to about 15ms displaced GRASE is expected to provide the best choice for fMRI when compared to EPI.

The simulation described in this section is, however, only a simplified model which has its limitations. In a real situation the image intensity is not purely determined by the signal at the center of k -space. The image distortions which are characteristic in EPI sequences have not been considered in the simulation either. Therefore, the predictions from the model are approximate and may be used as an indication for future experimental planning.

Chapter 5

Summary and conclusions

Summary

The investigation of human brain function with magnetic resonance imaging (fMRI) is currently performed by using blood oxygenation level dependent (BOLD) contrast in combination with fast gradient-echo MRI sequences like EPI. A limitation of EPI is its high sensitivity to magnetic susceptibility effects which leads to image distortion and signal loss, particularly in brain areas having strong magnetic field inhomogeneities. In the context of this work 'strong' means field inhomogeneities leading to T_2^* relaxation times of about 30ms. The limitations of EPI become more severe at high main fields, where the functional sensitivity given by the BOLD contrast is higher. The sensitivity to magnetic field inhomogeneities could be minimized by using fast MRI sequences based purely on spin-echoes, like RARE. However, in cases where extended brain areas are of interest, the application of RARE will be limited due to excessive RF power deposition. A solution of compromise can therefore be provided by an hybrid method that uses both gradient- and spin-echoes: GRASE.

When this work started there were no reports on the use of GRASE imaging with a high field system (i.e., above 1.5 Tesla) and no demonstration on the use of GRASE for fMRI. Hence, motivated by the expected properties of GRASE imaging when applied for fMRI in regions where EPI has a poor performance, the aims of this work were to: *i*) investigate and if possible improve the image quality of GRASE images obtained with a whole-body 3 Tesla MRI system, *ii*) investigate the BOLD contrast capabilities of GRASE for fMRI in brain regions with short T_2^* and find indications for its use. In the following, the main results will be summarized.

Implementation of GRASE imaging at 3 Tesla

GRASE was implemented as a multi-slice two-dimensional single-shot imaging method with three gradient-echoes per RF refocusing interval. The image quality given by the centric GRASE and k -space banded (kb) centric GRASE phase-encoding methods was investigated. These phase-encoding methods, which have already been described in the literature, have a short effective echo time (TE) and are therefore well suited to be used in combination with a preparation experiment which defines the desired image contrast independently from the phase-encoding scheme. The conventional centric phase-encoding method, although never proposed for GRASE, was also investigated as it also gives a short effective TE.

A new Template Interactive Phase-Encoding method

A new phase-encoding method is presented that, in principle, allows the calculation of any desired phase-encoding order from the signal decay of a template scan, i.e., one with no phase-encoding. This method was called "template interactive phase-encoding" or TIPE. The application of the TIPE method for short effective TE (centric TIPE) was proposed and demonstrated. In this application the signal decay of the template scan is used to order the echoes in k -space so that the resulting amplitude modulation has its maximum at the center, is symmetric around the center and decreases monotonically from the center of k -space. When using centric TIPE in multi-slice mode a template scan of each slice is used to calculate the phase-encoding order of each slice independently.

The comparison of centric TIPE with the previously mentioned phase-encoding methods gives the following results:

- a) Images obtained with the centric TIPE and conventional centric phase-encoding methods have similar signal-to-noise ratio (SNR) which in turn is approximately 10 % higher than that measured in centric GRASE and kb-centric GRASE images.
- b) Both centric TIPE and conventional centric phase-encoding methods produce low-frequency artifacts in the phase-encode direction. In the conventional centric method, the source of the artifacts is the modulation of both the amplitude and the phase of the signal in k -space. The centric TIPE method is mainly sensitive to phase artifacts. Thus, centric TIPE images are of most use when imaging regions where a good phase correction can be achieved.
- c) In regions with high magnetic field inhomogeneities, where the average phase correction is poor, the centric GRASE and kb centric GRASE methods may be preferable. These phase-encoding methods are less sensitive to phase errors at the cost of having stronger amplitude modulations in k -space which lead to high frequency artifacts in the phase-encoding direction.

BOLD sensitivity of GRASE for fMRI

In functional MRI the BOLD contrast refers to the ability to indirectly detect activation-induced blood oxygenation changes by detecting changes in local magnetic field inhomogeneities. These cause changes in T_2 and, most importantly, changes in T_2^* .

Intrinsic BOLD contrast of GRASE

Through the use of both gradient- and spin-echoes GRASE has an intrinsic T_2 and T_2^* contrast, and so it can be used to show BOLD contrast. A simulation was used to compare the intrinsic BOLD contrast of GRASE with that offered by pure gradient-echo (i.e., pure T_2^* contrast giving thus the highest BOLD sensitivity) and pure spin-echo (T_2 contrast) sequences.

The simulation shows that to make the intrinsic BOLD contrast of GRASE similar to that given by a pure gradient-echo method, an excessively high number of gradient-echoes per RF refocusing interval is required. This makes the GRASE sequence similar to an EPI sequence, which is known to give image distortions and signal loss, particularly in regions where T_2^* is short. Therefore, to keep the advantages offered by GRASE it was decided to investigate means for incorporating BOLD contrast while keeping a low number of gradient-echoes per RF interval.

BOLD contrast enhancement with the use of T_2^* -weighted GRASE

The T_2^* contrast can be increased by using a T_2^* -weighting preparation experiment followed by the GRASE imaging sequence. This, however, violates the Carr-Purcell Meiboom-Gill (CPMG) condition for the phase of the magnetization. The CPMG condition ensures the constructive interference of odd and even echoes originating from non-perfect 180° RF refocusing pulses. Thus, in order to use a T_2^* -weighting preparation experiment it was necessary to modify the GRASE sequence so that it became insensitive to the phase of the magnetization. This was achieved by use of the displaced-echo technique, which has been proposed for RARE-based sequences but not reported in the literature for GRASE. The displaced-echo technique works by selecting only one of the echo parities and dephasing the other, thus avoiding interference effects.

It is demonstrated that by using the displaced-echo technique it is possible to freely adjust the T_2^* contrast of GRASE images without visible interference artifacts and to use only three gradient echoes per RF interval. The displaced-echo technique has, however, the disadvantage that approximately only half of the available signal is used as result of using one echo parity group. This results in a reduction in the SNR by a factor of approximately 50 % in displaced GRASE images compared with conventional GRASE. With the TIPE scheme the signal loss may be reduced due to the fact that the highest intensity echoes are used to sample the center of k -space.

Demonstration of fMRI with GRASE based BOLD

To demonstrate the use of displaced GRASE for fMRI a comparison is necessary with an experimental protocol which gives well known, reproducible and strong brain activation. This would represent a difficult experiment when considering regions of the brain having short T_2^* . For this reason, it was decided to compare the sensitivities of T_2^* -weighted displaced GRASE and EPI using a conventional visual cortex paradigm on healthy volunteers. The visual cortex, although not a brain region characterized by short T_2^* , was chosen because of being an area known to give strong and reproducible activation.

Both EPI and GRASE show reproducible brain activation-induced signal changes predominantly located in the visual cortex. GRASE has, however, a lower functional sensitivity than EPI. An estimation of the contrast-to-noise ratio (CNR) from the measured data reveals that for GRASE the CNR is approximately 50 % of that given by EPI.

Image quality of displaced GRASE in regions with short T_2^*

Having demonstrated the use of displaced GRASE for fMRI in a brain region with long T_2^* , the image quality of GRASE was examined in regions of the brain having short T_2^* . The comparison was performed with gradient-echo EPI (GE-EPI) and spin-echo EPI (SE-EPI) for long (30 ms) and short (10 ms) T_2^* -weighting respectively.

The results show that:

- a) For long T_2^* -weighting displaced GRASE gives approximately half the SNR of GE-EPI, and
- b) For short T_2^* -weighting displaced GRASE gives similar SNR to SE-EPI but clearly better image quality.

A model for the functional sensitivity of displaced GRASE

A simple computational model was used to further examine the functional sensitivity of T_2^* -weighted displaced GRASE and compare it to that given by GE-EPI and SE-EPI sequences. The main aim of the model was to investigate the functional sensitivity of the different imaging methods when used for detecting brain activation in areas with short T_2^* . The model considers only activation-induced signal changes originated from changes in T_2^* .

The simulation suggests that:

- a) In agreement with the experimental findings, the functional sensitivity of GE-EPI is approximately a factor of two better than that given by displaced GRASE in areas with long T_2^* , and the SNR of displaced GRASE and SE-EPI is similar in regions low T_2^* contrast images.
- b) Due to the higher image quality of displaced GRASE and the similar functional sensitivity to SE-EPI for short T_2^* , it is expected that for tissues having up to $T_2^* \approx 15\text{ms}$ displaced GRASE will be preferable for fMRI.

Conclusions

In conclusion:

- A new template interactive phase-encoding method has been proposed. This method has been demonstrated for GRASE but in principle can be used for other imaging methods in which the signal decay is not known *a priori*.
- When considering the use of GRASE for fMRI using the BOLD contrast two possible avenues can be followed. One option is to use the intrinsic BOLD contrast of GRASE. This, however, requires that the GRASE sequence becomes an EPI-like sequence due to the increased number of gradient-echoes that are needed per RF refocusing interval. As a result, this option does not take full advantage of the reduced sensitivity to susceptibility effects of GRASE. The other option is to incorporate BOLD contrast with a preparation experiment at the cost of a reduction in the functional sensitivity. This allows GRASE to have a low number of gradient-echoes per RF interval thus showing better image quality than EPI based methods. Therefore, through a higher image quality (less subject dependent distortions and signal loss) displaced GRASE may provide an effectively higher functional sensitivity than EPI in regions with short T_2^* , in particular when averaging across subjects.

Appendix A

Materials

A.1 MRI system

A brief description of some hardware components of the system is provided in table A.1. In addition to the whole body Bruker gradient set, a Magnex head gradient set was available. The most relevant hardware specifications of the Magnex gradients are also listed in Table A.1. The main advantage of the Magnex gradient set was its shorter full strength ramp time ($150\ \mu s$) compared to the whole body gradient set ($450\ \mu s$). Both gradient sets had similar maximum strengths. The Magnex gradient set was used as an independent module which could be inserted and removed from the whole body magnet bore with minimal system reconfiguration.

A.2 MRI samples

A.2.1 Phantom

A phantom was constructed to investigate the artifact levels of GRASE images obtained with different phase-encoding methods. The phantom was designed so that its NMR relaxation properties were comparable to those of grey matter in human brain at 3 Tesla. It was measured that in grey matter T_1 is approximately 1.4s and that T_2 is in the range 50 - 120ms.

The phantom consisted of three glass tubes, each with 55 ml capacity and an internal diameter of 25 mm. The tubes contained Argarose gels doped with $NiCl_2$ [106]. The Argarose concentrations in the different vials were varied (1.3, 1.0 and 0.5 %) to achieve different T_2 s (70, 115 and 190 ms respectively). The $NiCl$ concentration was 1 mM for all tubes resulting in a T_1 of approximately 1 s. The T_1 and T_2 values of the solutions were measured using a multipoint inversion recovery method for T_1 and a multipoint spin-echo method for T_2 . The relaxation times were taken from a regression analysis.

A.2.2 Volunteers

Healthy human subjects were used to investigate the image quality of GRASE images and for performing the functional MRI experiments. Written informed consent was obtained in each case prior to examination. Each MRI examination lasted approximately 1 hour and 45 minutes. During the MRI examinations the volunteers wore ear plugs for acoustic protection. The

- **System**

- Model: Bruker Medizintechnik MEDSPEC 30/100 (Ettlingen, Germany).
- Magnet: 2.94 Tesla ($\nu_0 = 125$ MHz for protons), horizontal bore, internal diameter = 92 cm.
- Shims: 15 channels, room temperature, computer controlled.
- Computer: Bruker/SGI workstation with ParaVision imaging package.

- **Gradients**

- Bruker whole-body gradient set:
 - Model: B-GA 63, actively shielded, 63cm diameter.
 - Maximum strength: 30 mT/m for the three gradients, with a current of 600 A and a voltage of 350V.
 - Minimum ramp times (constant time mode): 450 microsec for the three gradients when switching from 0 to 100 % of maximum strength.
- Magnex head gradient insert:
 - Model: SGRAD III 580/400, actively shielded, 40cm diameter.
 - Maximum strength: 38 mT/m for X/Y, 35 mT/m for the Z gradient (at 600 A).
 - Minimum ramp times (constant time mode): for X/Y gradients 145 microsec, for Z gradient 100 microsec when switching from 0 to 100 % of maximum strength.
- Gradient amplifiers: B-GS 350/600, Copley 274 (constant voltage operation mode).
- Preemphasis: software controlled, three variable gains and time constant can be specified for each gradient.
- Gradient cooling system: water cooling circuit.

- **Radio-frequency**

- Frequency synthesizer: Programmed Test Sources PTS-310 (0.1-299 MHz, 1 Hz precision, phase coherent)
- Transmitter amplifiers: ENI RF pulse power amplifier MRI 5001 H (10-130 MHz, 4 KW)
- RF coil used: Bruker quadrature head coil (transmit-receive).

- **Patient safety**

- Magnet room supervisor unit: O_2 control, He and N_2 detector, air flow control.
- Patient alarm: possibility for the patient to give an acoustic signal by pressing an air bag.
- RF power control: mean transmitted power < 10 W.

Table A.1: Hardware description of the Bruker MEDSPEC 30/100 system with additional Magnex head gradient set

volunteers also wore a headphones microphone system (MRI Audio System, model RTC-9511-MXC77, Resonance Technology Inc., CA. USA) which allowed them to communicate with the operator at the console at any desired point during an MR examination. The volunteers could listen to music through the headphones except when a functional experiment was performed. The volunteers were asked to remain with their heads still during the examinations while laying their head on a comfortable head rest. No other head fixation mechanism was used.

The RF supervisor unit of the MRI system has hardware-based RF power transmission monitoring, allowing sequences to be tested on humans safely. The RF supervisor unit was set to allow a maximum mean transmitted RF power of 10 W per unit time. Assuming a mean adult's head weight of 6 kg, this gives a maximum power deposition of 2 W/kg, which is in accordance with safety guidelines [13].

Bibliography

- [1] F. Bloch, W. W. Hanssen, M. Packard. The nuclear induction experiment. *Phys. Rev.*, **70**:474–485, 1946.
- [2] E. M. Purcell, H. C. Torrey, R. V. Pound. Resonance absorption by nuclear magnetic resonance in a solid. *Phys. Rev.*, **69**:37, 1946.
- [3] W. G. Proctor, F. C. Yu. The Dependence of Nuclear Magnetic Resonance Frequency upon Chemical Compound. *Phys. Rev.*, **77**:717, 1950.
- [4] E. L. Hahn. Spin echoes. *Phys. Rev.*, **80**:580–594, 1950.
- [5] H. Y. Carr, E. M. Purcell. Effects of diffusion on free precession in nuclear magnetic resonance experiments. *Phys. Rev.*, **94**:630–638, 1954.
- [6] S. Meiboom, D. Gill. Modified spin-echo method for measuring nuclear relaxation times. *Rev. Sci. Instrum.*, **29**:688–691, 1958.
- [7] R. R. Ernst, W. A. Anderson. Application of Fourier transform spectroscopy to magnetic resonance. *Rev. Sci. Instr.*, **37**:93–102, 1966.
- [8] P. Lauterbur. Image formation by induced local interactions: examples employing nuclear magnetic resonance. *Nature*, **242**:190, 1973.
- [9] P. Mansfield, P. K. Grannell. NMR 'diffraction' in solids? *J. Phys. C*, **6**:L422–L426, 1973.
- [10] A. Abragam. *Principles of nuclear magnetic resonance*. Oxford University Press, Hong Kong, 1994.
- [11] A. Wokaun R. R. Ernst, G. Bodenhausen. *Principles of nuclear magnetic resonance in one and two dimensions*. Oxford University Press, Oxford, 1994.
- [12] D. I. Hoult C-N. Chen. *Biomedical magnetic resonance technology*. Adam Hilger, Great Britain, 1989.
- [13] . Board statement on clinical magnetic resonance diagnostic procedures. *Documents of the NRPB*, **2**:No. 1, 1991.
- [14] G. H. Glover, C. E. Hayes, N. J. Pelc, W. A. Edelstein. Comparison of linear and circular polarization for magnetic resonance imaging. *J. Magn. Reson.*, **64**:255–270, 1985.

- [15] C. P. Slichter. *Principles of magnetic resonance*. Springer Verlag, United States of America, 1990.
- [16] E. O. Stejskal. Use of spin echoes in a pulsed magnetic-field gradient to study anisotropic, restricted diffusion and flow. *J. Chem. Phys.*, **43**:3597–3603, 1965.
- [17] H. C. Torrey. Bloch equations with diffusion terms. *Phys. Rev.*, **104**:563–565, 1956.
- [18] J. Hennig. Multiecho Imaging Sequences with Low Refocusing Flip Angles. *J. Magn. Reson.*, **78**:397–407, 1988.
- [19] J. Hennig. Echoes - How to generate, recognize, use or avoid them in MR-imaging sequences. Part I: Fundamental and not so fundamental properties of spin echoes. *Concepts in Magn. Reson.*, **3**:125–143, 1991.
- [20] P. T. Callaghan. *Principles of Nuclear Magnetic Resonance Microscopy*. Oxford University Press (New York), 1995.
- [21] J. Hennig. Echoes - How to generate, recognize, use or avoid them in MR-imaging sequences. Part II: Echoes in imaging sequences. *Concepts in Magn. Reson.*, **3**:179–192, 1991.
- [22] D. G. Norris, P. Börnert, R. Reese, D. Leibfritz. On the application of ultra-fast RARE experiments. *Magn. Reson. Med.*, **27**:142–164, 1992.
- [23] D. G. Norris, P. Börnert. Coherence and interference in ultra-fast RARE experiments. *J. Magn. Reson. Med.*, **A 105**:123–127, 1993.
- [24] D. B. Twieg. The k -trajectory formulation of the NMR imaging process with applications in analysis and synthesis of imaging methods. *Med. Phys.*, **10**:610–621, 1983.
- [25] R. N. Bracewell. *The Fourier transform and its applications*. McGraw-Hill, Singapur, 1980.
- [26] A. N. Garroway, P. K. Grannel, P. Mansfield. Image formation in NMR by a selective irradiative process. *J. Phys. C*, **7**:L457–L462, 1974.
- [27] D. I. Hoult. The solution of the Bloch equations in the presence of a varying B_1 field: an approach to selective pure analysis. *J. Magn. Reson.*, **35**:69–86, 1979.
- [28] M. S. Silver, R. I. Joseph, D. I. Hoult. Highly selective $\pi/2$ and π pulse generation. *J. Magn. Reson.*, **59**:347–351, 1984.
- [29] D. E. Rourke, M. J. W. Prior, P. G. Morris, J. A. B. Lohman. Stereographic projection method of exactly calculating selective pulses. *J. Magn. Reson.*, **A 107**:203–214, 1994.
- [30] M. Shinnar, J. S. Leigh. The application of spinors to pulse synthesis and analysis. *Magn. Reson. Med.*, **12**:93–98, 1989.
- [31] S. Pickup, M. Popescu. Efficient design of pulses with trapezoidal magnitude and linear phase response profiles. *Magn. Reson. Med.*, **38**:137–145, 1997.

- [32] R. J. Sutherland, J. M. S. Hutchison. Three-dimensional NMR imaging using selective excitation. *J. Phys. E: Sci. Instrum.*, **11**:79–83, 1978.
- [33] L. Emsley, G. Bodenhausen. Self refocused 270° gaussian pulses for slice selection without gradient reversal in magnetic resonance imaging. *Magn. Reson. Med.*, **10**:273–281, 1989.
- [34] W. A. Edelstein, J. M. S. Hutchison, G. Johnson, T. W. Redpath. Spin warp NMR imaging and application to human whole-body imaging. *Phys. Med. Biol.*, **25**:751–756, 1980.
- [35] A. Haase, J. Frahm, D. Matthaei, W. Hanicke, K.-D. Merboldt. FLASH imaging: rapid NMR imaging using low flip-angle pulses. *J. Magn. Reson.*, **67**:258–266, 1986.
- [36] A. Haase. Snapshot FLASH MRI. Applications to T_1 , T_2 and chemical shift imaging. *Magn. Reson. Med.*, **13**:77–89, 1990.
- [37] D. G. Norris. Excitation angle optimization for snapshot FLASH and a signal comparison with EPI. *J. Magn. Reson.*, **91**:190–193, 1991.
- [38] T. Loonneker, F. Hennel, J. Hennig. Multislice Interleaved Excitation Cycles (MUSIC): an efficient gradient-echo technique for functional MRI. *Magn. Reson. Med.*, **35**:870–874, 1996.
- [39] T. Niendorf, S. Pollmann. Monitoring of location-dependent visual cortex activation: comparison between MUSIC and FLASH. in “*Proc., 3rd International Conference on functional mapping of the human brain, 1997*”, p. S502.
- [40] P. Mansfield. Multi-planar image formation using NMR spin echoes. *J. Phys. C*, **10**:L55–L58, 1977.
- [41] R. Turner F. Schmitt, M. K. Stehling. *Echo-planar imaging: theory, technique and application*. Springer, Berlin, 1998.
- [42] F. Farzaneh, S. J. Riederer, N. J. Pelc. Analysis of T_2 limitations and off-resonance effects on spatial resolution and artifacts in Echo-Planar imaging. *Magn. Reson. Med.*, **14**:123–139, 1990.
- [43] S.-G. Kim, X. Hu, G. Adriany, K. Ugurbil. Fast interleaved echo-planar imaging with navigator: high resolution anatomic and functional images at 4 Tesla. *Magn. Reson. Med.*, **35**:895–902, 1996.
- [44] J. Hennig, A. Nauerth, H. Friedburg. RARE imaging: a fast imaging method for clinical MR. *Magn. Reson. Med.*, **3**:823–833, 1986.
- [45] R. V. Mulkern, S. T. S. Wong, C. Winalski, F. A. Jolesz. Contrast manipulation and artifact assesment of 2D and 3D RARE sequences. *Magn. Reson. Imag.*, **8**:557–566, 1990.
- [46] K. Oshio, D. A. Feinberg. GRASE (Gradient- and Spin-Echo) Imaging: A Novel Fast MRI Technique. *Magn. Reson. Med.*, **20**:344–349, 1991.

- [47] D. A. Feinberg, B. Kiefer, G. Johnson. GRASE Improves Spatial Resolution in Single Shot Imaging. *Magn. Reson. Med.*, **34**:149–155, 1995.
- [48] G. Johnson, D. A. Feinberg, V. Venkataraman. Single-shot GRASE Imaging with Short Effective TEs. *J. Magn. Reson. Imag.*, **6**:944–947, 1996.
- [49] G. Johnson, D. A. Feinberg, V. Venkataraman. A Comparison of Phase Encoding Ordering Schemes in (T_2) Weighted GRASE Imaging. *Magn. Reson. Med.*, **36**:427–435, 1996.
- [50] P. A. Bandettini, E. C. Wong. Magnetic resonance imaging of human brain function. *Neuros. Clin. Nor. Amer.*, **8**:345–371, 1997.
- [51] C. S. Roy, C. S. Sherrington. On the regulation of blood-supply of the brain. *J. Physiol.*, **11**:85–108, 1890.
- [52] P. T. Fox, M. Raichle, M. Mintun, C. Dence. Nonoxidative glucose consumption during focal physiologic neural activity. *Science*, **241**:464–464, 1988.
- [53] W. Kuschinsky, O. B. Paulson. Capillary circulation in the brain. *Cerebrovasc. Brain Metab. Rev.*, **4**:261–286, 1992.
- [54] R. B. Buxton, E. C. Wong, L. R. Frank. Dynamics of blood flow and oxygenation changes during brain activation: the balloon model. *Magn. Reson. Med.*, **39**:855–864, 1998.
- [55] P. T. Fox, M. E. Raichle. Focal physiological uncoupling of cerebral blood flow and oxidative metabolism during somatosensory stimulation in human subjects. *Proc. Nat. Acad. Sci.*, **83**:1140–1144, 1986.
- [56] J. W. Belliveau, D. N. Kennedy, R. C. McKinstry, B. R. Buchbinder, R. M. Weisskoff, M. S. Cohen, J. M. Vevea, T. J. Brady. Functional mapping of the human visual cortex by magnetic resonance imaging. *Science*, **254**:716–719, 1991.
- [57] B. R. Rosen, J. W. Belliveau, D. Chien. Perfusion imaging by nuclear magnetic resonance. *Magn. Reson. A.*, **5**:263, 1989.
- [58] S. Ogawa, T. M. Lee, A. S. Nayak, P. Glynn. Oxygenation-sensitive contrast in magnetic resonance images of rodent brain at high magnetic fields. *Magn. Reson. Med.*, **14**:68–78, 1990.
- [59] S. Ogawa, T. M. Lee, A. S. Nayak, P. Glynn. Brain magnetic resonance imaging with contrast dependent on blood oxygenation. *Proc. Natl. Acad. Sci.*, **87**:9868–9872, 1990.
- [60] R. Turner, D. Le Bihan, C. T. Moonen, D. Despres, J. Frank. Echo-planar time course MRI of cat brain oxygenation changes. *Magn. Reson. Med.*, **22**:159–166, 1991.
- [61] M. E. Phelps, E. J. Hoffman, N. A. Mullani, M. M. Ter-Pogossian. Application of annihilation coincidence detection to transaxial reconstruction tomography. *J. Nucl. Med.*, **16**:210–224, 1975.

- [62] K. Herholz. *Signal sources in PET. In: Optical Imaging of Brain Function and Metabolism II.* Plenum Press (New York), 1997.
- [63] A. Villringer. *Understanding functional neuroimaging methods. In: Optical Imaging of Brain Function and Metabolism II.* Plenum Press (New York), 1997.
- [64] H. Berger. Über das Elektroenkephalogramm des Menschen. *Arch. Psychiatr. Nervenkr.*, **87**:527–570, 1929.
- [65] G. D. Dawson. A summation technique for detecting small signals in a large irregular background. *J. Physiol. Lond.*, **115**:2P–3P, 1951.
- [66] W. W. Orrison, J. D. Lewine, J. A. Sanders, M. F. Hartshorne. *Functional Brain Imaging.* Mosby (St. Louis), 1995.
- [67] D. Cohen. Magnetoencephalography: evidence of magnetic fields produced by alpha rhythm currents. *Science*, **161**:784–786, 1968.
- [68] J. Sarvas. Basic mathematical and electromagnetic concepts of the biomagnetism inverse problem. *Phys. Med. Biol.*, **32**:11–22, 1987.
- [69] F. F. Jobsis. Noninvasive, infrared monitoring of cerebral and myocardial oxygen sufficiency and circulatory parameters. *Science*, **198**:1264–1267, 1977.
- [70] A. Grinvald, R. D. Frostig, R. M. Siegel, E. Bartfeld. High-resolution optical imaging of functional brain architecture in the awake monkey. *Proc. Natl. Acad. Sci. (USA)*, **88**:11559–11563, 1991.
- [71] D. Malonek, A. Grinvald. Interactions between electrical activity and cortical microcirculation revealed by imaging spectroscopy: implications for functional brain mapping. *Science*, **272**:551–554, 1996.
- [72] R. W. Thatcher, M. Hallett, T. Zeffiro, E. R. John, M. Huerta. *Functional Neuroimaging.* Academic Press, Great Britain, 1994.
- [73] J. W. Belliveau, B. R. Rosen, H. L. Kantor, R. R. Rzedzian, D. N. Kennedy, R. C. McKinstry, J. M. Vevea, M. S. Cohen, I. L. Pykett, T. J. Brady. Functional cerebral imaging by susceptibility-contrast NMR. *Magn. Reson. Med.*, **14**:538–546, 1990.
- [74] R. M. Weisskoff, C. S. Zuo, J. L. Boxerman, B. R. Rosen. Microscopic susceptibility variation and transverse relaxation: theory and experiment. *Magn. Reson. Med.*, **31**:601–610, 1994.
- [75] K. K. Kwong, J. W. Belliveau, D. A. Chesler, I. E. Goldberg, R. M. Weisskoff, B. P. Poncelet, D. N. Kennedy, B. E. Hoppel, M. S. Cohen, R. Turner, C. Hong-Ming, T. J. Brady, B. R. Rosen. Dynamic magnetic resonance imaging of human brain activity during primary sensory stimulation. *Proc. Natl. Acad. Sci.*, **89**:5675–5679, 1992.
- [76] S. Ogawa, T. M. Lee. Magnetic resonance imaging of blood vessels at high fields: in-vivo and in-vitro measurements and image simulation. *Magn. Reson. Med.*, **16**:9–18, 1990.

- [77] L. Pauling, C. D. Coryell. The magnetic properties and structure of hemoglobin, oxy-hemoglobin, and carbonmonoxyhemoglobin. *Proc. Natl. Acad. Sci. USA*, **22**:210–216, 1936.
- [78] S. Ogawa, D. W. Tank, R. Menon, J. M. Ellermann, S. Kim, H. Merkle, K. Ugurbil. Intrinsic signal changes accompanying sensory stimulation: functional brain mapping with magnetic resonance imaging. *Proc. Natl. Acad. Sci. USA*, **89**:5951–5955, 1992.
- [79] P. A. Bandettini, E. C. Wong, R. S. Hinks, R. S. Tikofsky, J. S. Hyde. Time course EPI of human brain function during task activation. *Magn. Reson. Med.*, **25**:390–397, 1992.
- [80] A. M. Blamire, S. Ogawa, K. Ugurbil. Dynamic mapping of the human visual cortex by high-speed magnetic resonance imaging. *Proc. Natl. Acad. Sci. USA*, **89**:11069–11073, 1992.
- [81] P. A. Bandettini, E. C. Wong, A. Jesmanowicz, R. S. Hinks, J. S. Hyde. Spin-echo and gradient-echo EPI of human brain activation using BOLD contrast: a comparative study at 1.5 tesla. *NMR Biomed.*, **17**:336–347, 1994.
- [82] S. Ogawa, R. S. Menon, D. W. Tank, S. G. Kim, H. Merkle, J. M. Ellermann, K. Ugurbil. Functional brain mapping by blood oxygenation level-dependent contrast magnetic resonance imaging. *Biophys. J.*, **64**:803–812, 1993.
- [83] R. Turner, P. Jezzard, H. Wen, K. K. Kwong, D. Le Bihan, T. Zeffiro, R. S. Balaban. Functional mapping of the human visual cortex at 4 and 1.5 Tesla using deoxygenation contrast EPI. *Magn. Reson. Med.*, **29**:277–279, 1993.
- [84] P. A. Bandettini, E. C. Wong, A. Jesmanowicz, R. Prost, R. W. Cox, R. S. Hinks, J. S. Hyde. MRI of human brain activation at 0.5 T, 1.5 T and 3 T: comparisons of ΔR_2^* and functional contrast to noise ratio. in “*Proc., SMR, 2nd Annual Meeting, 1994*”, p. 434.
- [85] D. C. Noll, J. D. Cohen, C. H. Meyer, W. Schneider. Spiral k -space MR imaging of cortical activation. *J. Magn. Reson. Med. Imag.*, **5**:49–56, 1995.
- [86] D. A. Feinberg, K. Oshio. GRASE (Gradient- and Spin-Echo) MR imaging: A new fast clinical imaging technique. *Radiol.*, **181**:597–602, 1991.
- [87] D. A. Feinberg, K. Oshio. Gradient-Echo shifting in fast MRI techniques (GRASE imaging) for correction of field inhomogeneity errors and chemical shift. *J. Magn. Reson.*, **97**:177–183, 1992.
- [88] D. A. Feinberg, G. Johnson, B. Kiefer. Increased Flexibility in GRASE Imaging by k Space-Banded Phase Encoding. *Magn. Reson. Med.*, **34**:149–155, 1995.
- [89] A. Haase, J. Frahm, W. Hanicke, D. Matthaei. 1H NMR chemical shift selective (CHESS) imaging. *Phys. Med. Biol.*, **30**:341–344, 1985.
- [90] D. G. Norris. Ultrafast low-angle RARE: U-FLARE. *Magn. Reson. Med.*, **17**:539–542, 1991.

- [91] J. Jovicich, D. G. Norris. GRASE imaging at 3 Tesla with Template Interactive Phase-Encoding. *Magn. Reson. Med.*, **39**:970–979, 1998.
- [92] T. Niendorf. Quantitative mapping of T2* relaxation during visual stimulation at 3 T. in “*Proc., ISMRM, 6th Annual Meeting, 1998*”, p. 1404.
- [93] E. Bartholdi, R. R. Ernst. Fourier spectroscopy and the causality principle. *J. Magn. Reson.*, **11**:9–19, 1973.
- [94] Y. M. Kadah, X. Hu. Simulated phase evolution rewinding (SPHERE): a technique for reducing B_0 inhomogeneity effects in MR images. *Magn. Reson. Med.*, **38**:615–627, 1997.
- [95] T. Onodera, S. Matsui, K. Sekihara, H. Kohno. A method of measuring field-gradient modulation shapes. Application to high speed NMR spectroscopic imaging. *J. Phys. E: Sci. Instrum.*, **20**:416–419, 1987.
- [96] A. B. Kerr, J. M. Pauly, C. H. Meyer, D. G. Nishimura. Image quality for spiral-based sequences. in “*Proc., SMR, 3rd Annual Meeting, 1995*”, p. 622.
- [97] P. Jehenson, M. Westphal, N. Schuff. Analytical method for the compensation of eddy-current effects induced by pulsed magnetic field gradients in NMR systems. *J. Magn. Res.*, **90**:264–278, 1990.
- [98] R. S. Menon, S. Ogawa, D. W. Tank, K. Uğurbil. 4 Tesla gradient recalled echo characteristics of photic stimulation-induced signal changes in the human primary visual cortex. *Magn. Reson. Med.*, **30**:380–386, 1993.
- [99] M. Barth, M. Diemling, E. Moser. Modulation of signal changes in gradient-recalled echo functional MRI with increasing echo time correlate with model calculations. *Magn. Reson. Imag.*, **15**:745–752, 1997.
- [100] D. G. Norris, M. H.-Berlage, F. Wittlich, T. Back, D. Leibfritz. Dynamic imaging with T_2^* contrast using U-FLARE. *Magn. Reson. Imag.*, **11**:921–924, 1993.
- [101] P. Le Roux, R. S. Hinks. Stabilization of echo amplitudes in FSE sequences. *Magn. Reson. Med.*, **30**:183–191, 1993.
- [102] F. Schick. SPLICE: sub-second diffusion-sensitive MR imaging using a modified fast spin-echo acquisition mode. *Magn. Reson. Med.*, **38**:638–644, 1997.
- [103] T. Niendorf. Functional Mapping of Human Motor Cortical Areas with T2* Sensitized Split-Echo UFLARE. in “*Proc., ISMRM, 6th Annual Meeting, 1998*”, p. 1562.
- [104] R. W. Cox. Software for analysis and visualization of functional magnetic resonance neuroimages. *Comput. Biomed. Res.*, **29**:162–173, 1996.
- [105] P. A. Bandettini, A. Jesmanowicz, E. C. Wong, J. S. Hyde. Processing strategies for time-course data sets in functional MRI of the human brain. *Magn. Reson. Med.*, **30**:161–173, 1993.

- [106] K. A. Kraft, P. P. Fatouros, G. D. Clarke, P. R. S. Kishore. An MRI phantom material for quantitative relaxometry. *Magn. Reson. Med.*, **5**:555–562, 1987.

Acknowledgements

I would like to extend my sincere gratitude

To David Norris, my supervisor, for his help, guidance and patience throughout this project, specially for keeping always an amazing enthusiasm and good humour.

To the rest of the NMR group, Rosie Dymond, Martin Koch, Christian Schwarzbauer, Christopher Wiggins, Thoralf Niendorf, Bettina Johst, Reiner Hertwig, Manfred Weder, Herbert Kuh and Piotr S. Zbgwyev, for providing assistance and encouragement in innumerable occasions and with whom I had the chance to enjoy three unforgettable years.

To our wonderful MTAs team, Katrin Wiesner, Grit Wenge, Sabine Busker and Harold, for chearing up the physicists team when things were looking dull and for their good disposition for staying many times until late in the evening working with us.

To Andrea Sandmann and Stephan Liebig, for their enthusiasm and the excellent quality of their work preparing slides, posters and other printouts.

To all the people in the MPI with whom I had the chance to interact, for offering always a familiar and very friendly atmosphere.

To Prof. Y. D. von Cramon, for his advice and support as well as for proof reading this manuscript.

And to my family and friends, from here and from far away, for providing continual encouragement during my time in Leipzig.

Leipzig, 30. Oktober 1998

Curriculum Vitae

Name: Jorge Jovicich
Date of birth: March 13th, 1968
Place of birth: Córdoba, Argentina
Nationality: Argentinean
Marital Status: Single

Education:

1995 - present: Ph.D.
Max-Planck-Institute of Cognitive Neuroscience, Leipzig, Germany
Department of Physics, University of Leipzig

1993 - 1994: M.Sc. in Medical Imaging
Dept. of Bio-Medical Physics and Bio-Engineering,
University of Aberdeen, UK
Thesis: Physiological monitoring within a strong
magnetic field strength
Supervisors: J. M. S. Hutchison, M. A. Foster

1987 - 1993: First Degree: Licentiate in Physics (5 years career)
School of Mathematics, Astronomy and Physics (FaMAF)
National University of Córdoba - Argentina
Thesis: Synchrotron radiation for breast imaging:
a Monte Carlo simulation
Supervisors: M. Rubio, G. Vélez

Professional experience:

Jan. 1992 - Feb. 1992 Summer Course (duration: 7 weeks)
National Laboratory of Synchrotron Light (LNLS),
Campinas, San Pablo, Brazil.
Subject: work with the Vacuum Group

Mar. 1993 - Sept. 1993 Full-time research and teaching assistant at FaMAF,
National University of Córdoba, Argentina

Oct. 1994 - June 1995 Working visitor
NMR Group of the Experimental Oncology Division,
Radiobiology Unit, Medical Research Council, United Kingdom

Publications

Journals

1. Jovicich J. and Norris D. G., GRASE imaging at 3 Tesla with Template Interactive Phase-Encoding (TIPE), *Magn. Reson. Med.*, **39**, 970-979 (1998).
2. Jovicich J. and Norris D. G., Functional MRI of the human brain with GRASE based BOLD contrast, *Magn. Reson. Med.* (submitted).

Works presented at conferences

1. Jovicich J. and Norris D. G., Functional neuroimaging with GRASE: a comparison with GRE and SE sequences, in "*Proc., 13th Annual Meeting of the European Society for Magnetic Resonance in Medicine and Biology, Prague, 1996*", p. 69. Oral presentation.
2. Jovicich J. and Norris D. G., Functional neuroimaging with GRASE: a comparison with GRE and SE sequences, in "*Proc., 5th Scientific Meeting and Exhibition of the International Society for Magnetic Resonance in Medicine, Vancouver, 1997*". p. 1622. Poster.
3. J. Jovicich, D. G. Norris, Template Interactive Phase-Encoding (TIPE): Application for short effective TE GRASE imaging at 3 Tesla, in "*Proc., 14th Annual Meeting of the European Society for Magnetic Resonance in Medicine and Biology, Brussels, 1997*", p. 49. Oral presentation.
4. J. Jovicich, D. G. Norris, fMRI with GRASE at 3T: initial evaluation using split echo technique, in "*Proc., 6th Scientific Meeting and Exhibition of the International Society for Magnetic Resonance in Medicine, Sydney, 1998*", p. 1448. Poster.
5. J. Jovicich, D. G. Norris, Funktionelle GRASE-Bildgebung bei 3 Tesla, in "*Proc. International Society for Magnetic Resonance in Medicine, 1. Tagung der Deutschen Sektion, Freiburg, 1998*", p. 37. Oral presentation.

Patent

1. J. Jovicich, D. G. Norris, Template Interactive Phase-Encoding (TIPE) for magnetic resonance imaging. Anmelder: Max-Planck-Gesellschaft. German and international application.